Quasi-free proton and neutron knockout reactions in oxygen-20

Najafi, Mohammadali

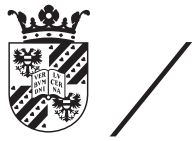

rijksuniversiteit
groningen

Quasi-free proton and neutron knockout reactions in ^{20}O

PhD thesis

to obtain the degree of PhD at the
University of Groningen
on the authority of the
Rector Magnificus, Prof. E. Sterken
and in accordance with
the decision by the College of Deans.

This thesis will be defended in public on

Friday 17 January 2013 at 16:15 hrs.

by

Mohammad Ali Najafi

born on 23 June 1982
in Shahreza, Iran

Supervisor:
Prof. N. Kalantar-Nayestanaki

Co-supervisors:
Dr. M. Mahjour-Shafiei
Dr. C. Rigollet

Assessment committee:
Prof. T. Aumann
Prof. M.N. Harakeh
Prof. R. Zegers

ISBN 978-90-367-6690-6 (printed version)

ISBN 978-90-367-6694-4 (electronic version)

Available online at:

http://dissertations.ub.rug.nl/faculties/science/2014/

QR code:

Contents

Chapter

Introduction

Physicists mostly date nuclear physics to 1896, when Henri Becquerel discovered radioactivity; however, the concept of *atomic nucleus* as a dense positively-charged body in the core of atoms was realised in 1911, just a year after Ernest Rutherford and his team, Geiger and Marsden, scattered a beam of alpha particles from a gold foil. Based on the proposal of Rutherford, they searched for large-angle-scattered alpha particles, and to their surprise, they observed some. The interpretation of this observation as the existence of the atomic nucleus led to the Rutherford's model of the atom.

Since their discovery, atomic nuclei have been studied for about a century; many theoretical models were developed to explain their properties and many experimental methods invented to probe the structure of the nucleus and consequently test the models. Two major models for describing atomic nuclei are the *collective* and *shell models*[1]. In the collective model, it is assumed that all or almost all of the nucleons participate in every movement of the nucleus. On the contrary, in the basic shell model (usually known as *independent-particle* model), it is assumed that the movement of each nucleon is independent of the others. Both models are widely used, each one surpassing the other in a certain nuclear property. The shell model was suggested by two independent groups at the same time, in an attempt to explain the observation of the *nuclear magic numbers* by a model similar to the atomic shell model. These magic numbers were defined based on the solid evidence of large gaps in the nucleon separation energies, and were later reproduced by the shell models.

Generally, for low-energy states, the shell model gives a better explanation of the nuclear properties such as magic numbers, spins, parities, than the collective model. The reason is that at low energies the nucleon-nucleon collisions inside atomic nuclei are suppressed and nucleons move almost independently [1]. However, the shell model fails in a number of predictions. One of its most outstanding failures is

[1]Here *shell model* means "nuclear shell model" and when referring to atomic shell model it is mentioned explicitly.

the quadrupole moments of nuclei, especially when the proton and neutron numbers are not close to the magic numbers [2]. Modern shell model calculations incorporating *effective interactions* have made it possible to reach a global description of nuclear dynamics in a vast region of the chart of the nuclei [3].

1.1 Shell model in a nutshell

In the nuclear shell models, resembling the atomic shell model, each nucleon is restricted to the distinct states from the solution of the Schrödinger equation with a potential well. This potential well, usually called *nuclear mean field*, is generated by the interactions of each nucleon with the other nucleons in the nucleus. The nuclear mean-field approach is based on the assumption that the movement of the nucleons in the atomic nuclei is non-relativistic, and therefore the Schrödinger equation can be used. A many-body Schrödinger equation with a non-trivial potential such as realistic[2] nucleon-nucleon potentials is not tractable with the current computational power, except for a few light nuclei. Therefore, it was assumed additionally that the nuclear mean field can be approximated by an isotropic harmonic oscillator combined with a spin-orbit term. This approximation gives rise to a quantisation of the nuclear states, which allows conversion of the complex many-body problem of a nucleus to A one-body problems, with A being the atomic mass number. Later, more advanced mean-field potentials such as *Woods-Saxon* [4] were proposed instead of the harmonic oscillator. Figure 1.1 shows the scheme of the single-particle states obtained from shell model calculations.

When solving the Schrödinger equation of a nucleus within a shell model, the mean-field potential depends on the configuration of the nucleons with respect to the centre of mass, and the configuration of the nucleons depends on the mean field. The usual approach to this iterative problem is the Hartree-Fock method which results in the best possible solutions for the ground-state wave function and energy of the nucleus. The Hartree-Fock solutions based on a mean-field potential are of limited application, because the mean-field potentials ignore the complex features of the nucleon-nucleon interaction, the so-called *residual interactions*.

The formal way of including the residual interactions in the Hamiltonian is by employing the effective interactions. Effective interactions can be obtained phenomenologically, in which case they depend on the experimental data, or be constructed from the realistic nucleon-nucleon interactions. Normally, in deriving the effective interactions we cannot take into account all possible configurations. The full Hilbert space must be truncated to a so-called model space; in other words, only a subspace of the Hilbert space is chosen in which the eigenvalue problem with the residual interactions can be solved. Having the model space including the selected orbitals, the effective operators are introduced in order to take into account the contribution of the excluded part of the Hilbert space. A variety of different schemes for introduction of the effective operators have been used, which gave rise to many

[2]Realistic interactions are the ones that reproduce the properties of the two-nucleon systems accurately.

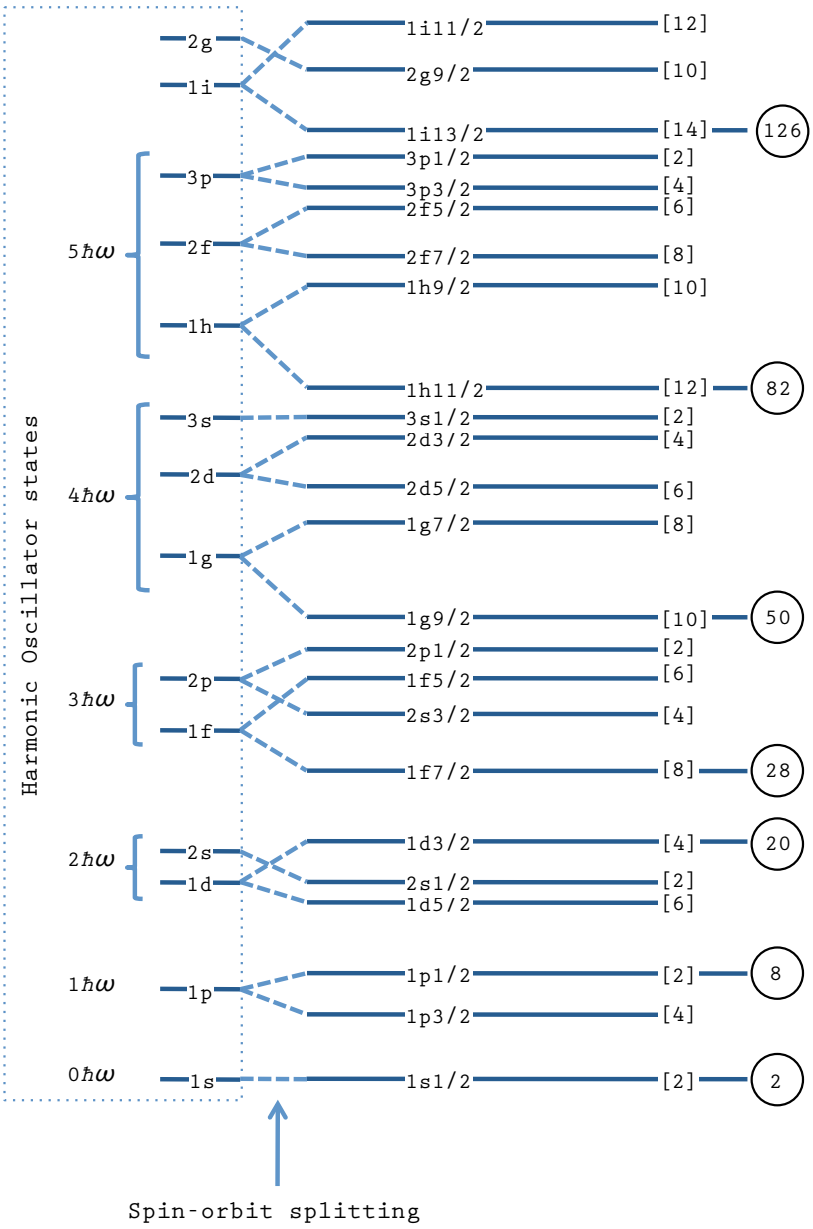

Figure 1.1: The shell structure of the atomic nuclei obtained from the shell model. The numbers indicated by circles are total number of nucleons below that level, and the numbers in brackets are the number of nucleons in that level.

successful theoretical predictions. For example, the nucleon binding energies and the shapes of the single-particle wave functions were predicted fairly accurately, using the effective-interaction approach [5] and the energy-density functionals [6] included in the shell model calculations. (For reviews about the shell model and effective interactions see [3] and [7, 8].)

Many single-particle properties of the atomic nuclei have been studied extensively in the direct nuclear reactions. Specifically, analysis of the differential cross sections can lead to a wealth of information about the nuclear properties as well as the reaction mechanism. The transfer and knockout reactions give detailed information about the shell structure and spectroscopic factors. In a knockout reaction at beam energies of several hundred MeV per nucleon, deeply-bound nucleons can be knocked out.

Pioneered by Mougey's experiments [9] in the 1980s, it has been observed that the cross sections of one-nucleon knockout reactions are smaller than the predictions of the independent-particle model [1]. It is as if only a fraction of a nucleon is sitting in an eigen state of the nuclear mean field. This observation was interpreted as fragmentation of the wave function of the nucleon into higher excited states; and therefore, the occupancy level of that state is quenched.

As a first conjecture, short-range correlations were investigated as the cause of this phenomenon. The contribution of the short-range correlations did not, however, account for the observed quenching. In fact the *ab initio* calculations showed that the inclusion of the short-range correlation in the theory, led to 10–15% depletion of the occupancies, as compared to around 35% observed in $(e\,,e'p)$ reactions [10]. As a result, the long-range correlations are also being considered, which show that a combination of the configuration mixing and coupling to collective resonances may give an account of the observed reduction of the occupancies [11, 12].

A systematic measure of the occupancy of a level can be achieved using spectroscopic factors. The theoretical definition of the spectroscopic factors and their measurement will be given in the next chapter.

1.2 Advance of nuclear physics experiments

Until the 1950s, nuclear physics experiments were limited to the stable nuclei found in nature (black spots in Figure 1.2), and a few unstable nuclei with long life-times. The first experiments with unstable ion beams were performed during 1950s in the Niels Bohr institute in Copenhagen [13, 14]. Since then, other unstable ion beam facilities have been constructed, which have produced many unstable ions. Figure 1.2 shows these ions in different colours based on their production mechanism: light-ion induced reactions (green), fragmentation (blue), fusion or transfer reactions (orange), and radioactive decay chain (magenta). Furthermore, it is predicted that more than 3000 more nuclei could exist in bound states, but have not been experimentally observed yet. These nuclei are shown as yellow area in Figure 1.2, whose edges demonstrate the theoretical limits of existence of atomic nuclei [15]. These limits indicate the minimum and maximum ratio of proton-to-neutron num-

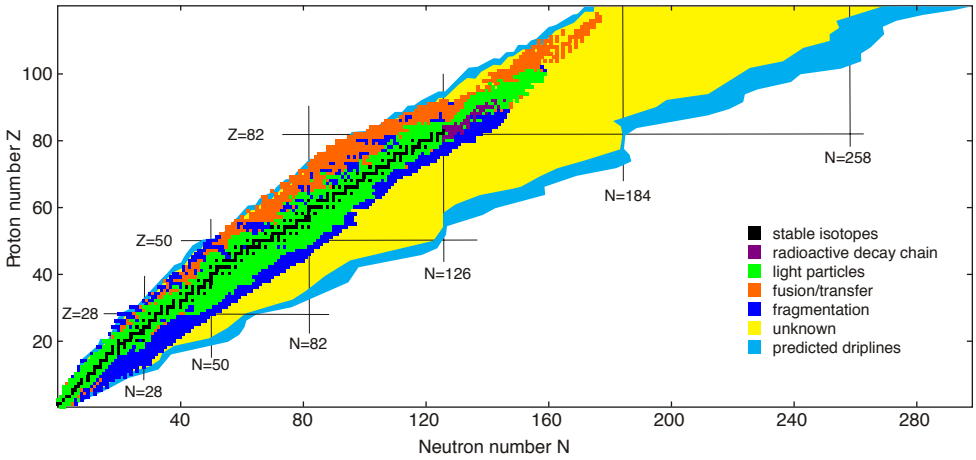

Figure 1.2: The broad view of the chart of atomic nuclei. The stable nuclei found in nature are marked as black. Other nuclei are shown in different colours depending on their production mechanism. The yellow area indicates the nuclei that are predicted to be bound but have not been observed. The cyan bands are the uncertainties of the drip lines (picture from Reference [16]).

ber for each element that can form a bound nucleus, and are called neutron and proton drip lines, respectively. The cyan bands at the edges of the yellow area are the uncertainties in the theoretical predictions of the drip lines.

In the last few decades, the knowledge of atomic nuclei has profoundly benefited from accelerator facilities. Specially, the production of short-lived nuclei has opened opportunities to study new areas of the chart of nuclei, and test the quality of models that were developed based on the stable-ion experiments. The unstable ion beams are produced using two methods: Isotope Separation On-Line (ISOL), and in-flight separation. In the ISOL method, a primary beam impinges on a thick production target, the ions of interest are then extracted from the production target and guided through an electromagnetic mass analyser, which separates different masses. Finally, the selected ions can be re-accelerated if necessary. In the in-flight separation method, the primary beam punches through a thin target, from which different reaction fragments eject. The ions of interest are then selected using an array of large-aperture magnetic spectrometers.

Generally, the ion beams produced by the ISOL method have higher intensities and better optical qualities than the ones produced by the in-flight technique. However, the ISOL method is not suitable for very short-lived ions (half-lives shorter than a 100 ms), and also depends on the chemistry of the isotope species, while in-flight technique can produce very short-lived ions (as short as 1 μs, depending on the flight path of the ions in the device). Moreover, the in-flight separation method is independent of chemistry, and therefore, unlike the ISOL method it can produce almost all ions between the proton and neutron drip lines. For a review of the ISOL and in-flight separation methods see References [17] and [18], respectively.

Currently, both ISOL and in-flight methods are widely used worldwide, and several facilities are established using them, namely: REX-ISOLDE at CERN (Switzerland), SPIRAL at GANIL (France), and ISAC at TRIUMF (Canada) are the current major facilities using ISOL method, and SISSI-ALPHA at GANIL (France), RIPS at RIKEN (Japan), A1900 at NSCL (USA), and FRS at GSI (Germany) for the in-flight technique[3].

To gain further grounds in the nuclear landscape and improve the knowledge of nuclear properties close to the drip lines, new generations of the unstable beam facilities are being constructed or planned to be constructed. HIE-ISOLDE is an upgrade of the REX-ISOLDE and have been under construction since last few years[4]. SPIRAL2 is a new multi-purpose facility that will be coupled to the present GANIL facility[5]. ISAC-II at TRIUMF now includes a linear superconducting accelerator that boosts the production of rare-isotope production[6]. FRIB at NSCL will be a new national user facility for nuclear science[7]. And FAIR at GSI is an ambitious and multi-purpose facility with a novel and extensive nuclear physics programme[8], and will be introduced in more details during this thesis.

The GSI laboratory in Germany is one of the large ion-beam accelerator facilities, which has been producing and delivering beams of stable and unstable ions to different experiments since the 1970s. At the time of writing this dissertation, the Facility for Antiproton and Ion Research (FAIR) [19] is being constructed adjacent to GSI as the new generation of ion accelerator facilities with a broad range of scientific goals (see Figure 1.3). One of the four scientific pillars of FAIR is the NUclear STructure, Astrophysics and Reactions (NUSTAR) project, which includes several sub-projects: Super-FRS, HISPEC/DESPEC, R^3B, MATS, LaSpec, ILIMA, ELISe, and EXL. Each one of these sub-projects covers parts of the NUSTAR physics case, and all together they make it possible to study almost every scientific question in low- and intermediate-energy nuclear physics. Among these, EXL (Exotic nuclei studied in Light-ion induced reactions in NESR storage ring), and R^3B (Reactions with Relativistic Radioactive Beams) are the major projects that will focus on nuclear structure and reactions. A list of the physics goals of these projects is given in Section 2.1. This thesis is an account of my work during the past four years within the EXL and R^3B projects.

1.3 This thesis

This thesis is based on two independent projects: one within the EXL collaboration along with the developments of the future EXL experimental setup, and another

[3] For a more complete list of the accelerator facilities worldwide see: http://www-elsa.physik.uni-bonn.de/accelerator_list.html.

[4] About HIE-ISOLDE see: http://hie-isolde.web.cern.ch/hie-isolde/

[5] About SPIRAL2 see: http://pro.ganil-spiral2.eu/spiral2/what-is-spiral2/

[6] About ISAC-II see: http://www.triumf.ca/research-program/research-facilities/isac-facilities

[7] About FRIB see: http://www.frib.msu.edu/about

[8] About FAIR see: http://www.fair-center.eu/

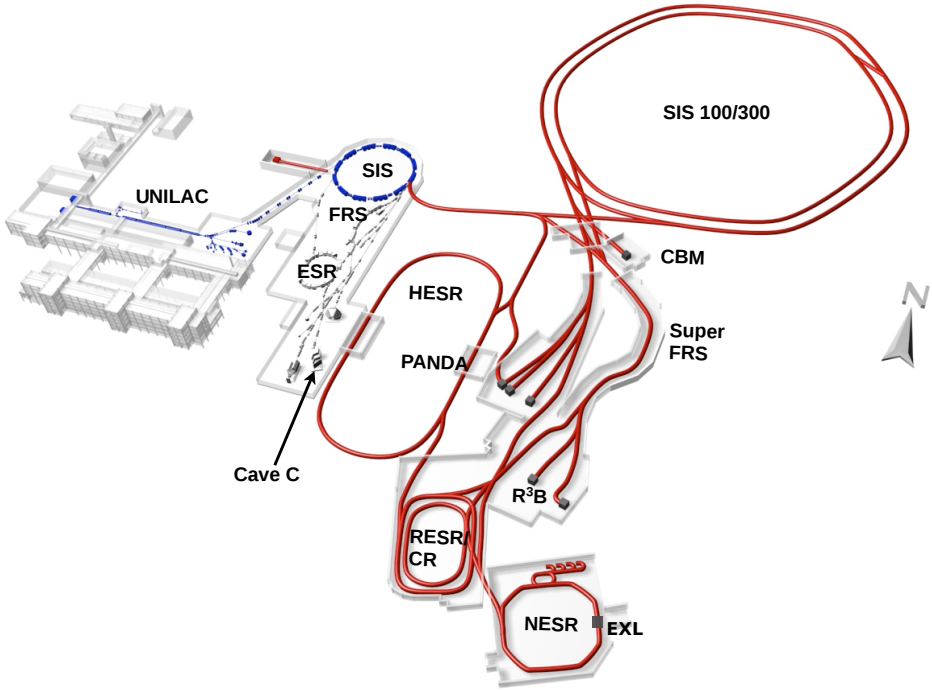

Figure 1.3: The schematic view of FAIR together with GSI. The red colour indicates FAIR next to the current GSI facility shown in blue. Picture adapted from Reference [20].

one with the LAND-R^{3}B collaboration, focusing on systematic spectroscopy of the oxygen isotopes. The former includes an in-beam test of a few detection units of the proposed EXL setup. The report of this test and its results will be presented in Chapter 3. However, the major part of this thesis is on the latter; an experimental study of the quasi-free nucleon knockout from ^{20}O. The experiment, called S393, was performed using the LAND-R^{3}B setup at GSI, Germany. The description of this experiment is given in Chapter 4, which includes an introduction of the setup together with the calibration and reconstruction of the data. Chapter 2 contains the theoretical background behind the physics goals of the EXL and R^{3}B projects, with an emphasis on the spectroscopic factors. The theoretical definition and the phenomenological formula of the spectroscopic factors are given in this chapter. Chapter 5 presents the data analysis and the results; including the bound and unbound excited states of ^{19}N observed in this experiment, the cross section of the proton knockout from ^{20}O, the quenching factor of the proton states in ^{20}O, and the momentum distributions of the reaction products. Chapter 6 gives a summary of the whole thesis and an outlook into the future.

Chapter

Physics goals of EXL and R^3B

EXL and R^3B are two projects within NUSTAR, dedicated to the reaction and structure studies of atomic nuclei. The EXL experimental setup is designed and optimised to couple to an ion storage ring and primarily explore the low-momentum-transfer reactions. On the other hand, the R^3B experimental setup is specifically designed to investigate the high-momentum-transfer reactions and will be constructed at the end station of the high-energy branch of the FAIR Super-FRS facility, see Figure 1.3.

In this chapter, first the physics goals of these two projects are listed, together with a very basic theoretical background. Then, the spectroscopic studies, the main subject of interest in this thesis, are introduced in more details in Section 2.2. For an overview of the EXL and R^3B experimental setups see their respective technical design proposals [21, 22].

2.1 Physics goals of EXL and R^3B

The physics goals of the EXL and R^3B projects overlap to some extent. As long as light-ion induced reactions are considered, some of the physics goals of EXL can be obtained within R^3B and also the other way around. However, as already mentioned, EXL is exclusively optimised for low-momentum-transfer reactions, while being able to cover high-momentum-transfer region as well. On the contrary, R^3B is designed for high-momentum-transfer studies, and moreover, is capable of studying heavy-ion-induced reactions which are not accessible to EXL due to the gas-jet structure of the target. Therefore, these two projects are complementary, and together they make it possible to extract in-depth information from nuclear reactions. In the rest of this section the physics goals of these two projects are briefly introduced.

Matter distribution

Unusual matter distributions have been observed in a few neutron-rich nuclei close to the neutron drip line. For example, ^{11}Li has a surprisingly large extension, almost as large as a lead nucleus with more than 200 nucleons. This observation was interpreted to be due to the fact that the last neutron has a very extended wave function [23], which results in a large tail in the matter distribution of ^{11}Li. This broad distribution of the last two neutrons around the core of ^{9}Li is called *halo*, and is one of the interesting subjects in nuclear structure studies. The nuclei having this unusual matter distribution are called *halo nuclei*, and provide an opportunity to study the *nuclear matter* at very low densities.

Another case of matter distribution that will be addressed in the EXL and R^{3}B projects is the so-called neutron *skin* in neutron-rich nuclei. This effect appears when the number of neutrons with respect to the number of protons increases. Generally, the isospin asymmetry forces favour equal proton and neutron densities all over the nucleus. However, with increase of the neutron number, protons become more bound, and therefore the density distribution of protons cannot extend to the surface of the nucleus [24]. From macroscopic point of view, in neutron-rich nuclei, the nuclear medium imposes a pressure strong enough to condense protons in the core of the nucleus and thus leave a neutron skin on the surface. The same pressure is considered to be involved in the stability of neutron stars. Measurements of the neutron-skin thickness provides strong constraints on this pressure [25, 26], which is of essential importance for understanding the stability of neutron stars.

Furthermore, neutron skins are microscopic laboratories for investigation of the density dependence of the nuclear symmetry energy, which is one of the components of the Equation-Of-State (EOS) of neutron-rich matter. The equation of state is a thermodynamic description of a large volume of nuclear matter, and is the main tool to study the phase transitions of neutron stars, and therefore, its sensitivity to symmetry energy is of fundamental importance in nuclear and astro-nuclear models [27].

Shell structure of unstable nuclei

Many of the properties of stable nuclei are well described using shell models with effective interactions. However, recent investigations of the shell structure of neutron-rich nuclei have shown that the traditional shell structure of the nucleus observed in stable nuclei is altered for unstable nuclei near neutron and proton drip lines. For instance, in neutron-rich nuclei in the *sd*-shell it has been observed that the shell gap at $N = 20$ shrinks, and a new shell gap at $N = 16$ emerges [28] (see Figure 1.1).

Recently, much attention and interest has been drawn to the contribution of different forces in the evolution of shell closures. Several theoretical studies have been performed to figure out what terms of the nucleon-nucleon interaction cause the evolution of the shell structure. First, it was suggested that the central forces play a dominant role in the construction of the shell structure and its evolution [29]; however, later on, other speculations were put forward that the vector and spin-tensor

forces can be very significant [30, 31]. So far, the role of different nucleon-nucleon forces as well as three-nucleon forces have not been determined unambiguously, which requires more theoretical studies and experimental inputs.

A key point to this problem and many other problems in shell model calculations is the correlations of nucleons. These correlations as opposed to independent behaviour of nucleons are not projected in a well-defined observable, and therefore, spectroscopic factors were introduced as one of the ways of acquiring information about the role and consequences of the correlations. Chapters 4 and 5 of this thesis are dedicated to an experimental study which exploits quasi-free nucleon knockout reactions, aimed at the spectroscopy of oxygen nuclei. Therefore, the spectroscopic factors and their role in the shell model will be explained in more details in a separate section (2.2).

Clusters in neutron-rich nuclei

Another objective of the quasi-free reactions is to study clustering in neutron-rich nuclei. The clustering phenomenon was suggested even before the emergence of the shell model. It was observed that for some of the light nuclei, specially for $A = 4n$ nuclei, the energy levels are better explained if it is assumed that the structure of the nucleus is mainly governed by the dynamics of clusters rather than that of individual nucleons[1] [32]. It means that one can ignore the inner structure of each cluster and only focus on the dynamics of the clusters with respect to each other. For instance, certain levels of ^{10}Be can be described as a molecular state of two alpha clusters plus two neutrons, in which the neutrons are continuously exchanged between two alpha clusters [33]. In neutron-rich nuclei close to the drip line, movements of extra neutrons around the clusters change the dynamics of the system. The proton-induced cluster knockout reactions are used to extract spectroscopic factors of the clusters, and determine the occupancies of cluster states [34].

New collective modes and giant resonances

Excitation of atomic nuclei to the continuum states is profoundly governed by the collective motions of the nucleons in the form of multipole vibrations. The first hint of these collective motions appeared in 1930 when Thibaud suggested rotational modes for ^{208}Tl as the daughter nucleus in the alpha decay of ^{212}Bi [35][2]. However, the concept of the collective modes became substantial based on the observation of a very low excitation energy for the first 2^+ state, far below the energy needed to break the 0^+ nucleon pair [36].

Electromagnetic excitations and light-ion inelastic scattering populate different collective modes of exotic nuclei with reasonably high cross sections. Using these reactions, low-lying isoscalar and high-lying giant resonances can be probed as well

[1] One of the physics goals of the experiment S393, which will be introduced in Chapter 4, is to study the cluster structure of light neutron-rich nuclei, like, ^{8}Be as a bound state of two alpha particles.

[2] Later, it was found out that ^{208}Tl does not have significant rotational modes.

as proton and neutron density distributions, which can manifest meaningful differences from each other. Giant resonances are categorised based on their multipolarity, spin and isospin , and consequently, provide tools for a broad range of studies on nuclear matter and finite nuclei. For example, measurement of the isoscalar giant monopole strength gives a measure of the incompressibility of the atomic nuclei, which appears in the nuclear-matter equation of state [37]. Moreover, giant resonances carry information about the matrix elements of effective nucleon-nucleon potentials. Specifically, the parameters of the effective interactions can be adjusted to reproduce the centroid energy of the giant resonance modes [38].

Recently, the observation of low-lying dipole strengths in neutron-rich nuclei near the neutron drip line has become an intriguing puzzle in the field. Among all possible excitations, the coherent vibration of the valence neutrons against the core seems to have a significant contribution, as large as a few percent of the energy-weighted sum rules [39, 40]. Such vibrations are commonly referred to as *pygmy* or *soft* dipole resonances and are recently supported by theoretical calculations [41, 42, 43].

Gamow-Teller transition; Charge-exchange reactions

The Gamow-Teller transitions are beta decays in which the spin vectors of the released leptons are parallel ($\Delta S = 1$), as opposed to the super-allowed Fermi transitions in which the spin vectors are anti-parallel ($\Delta S = 0$). The Gamow-Teller transitions are governed by the spin-isospin excitations due to weak interactions, and have a rather simple operator: $\sigma\tau$, σ and τ being the spin and isospin operators, respectively. This makes them a very good choice for the study of the spin-isospin correlations in nuclei. At small momentum transfers, the total Gamow-Teller transition strength is less than model-independent Ikeda sum rule [44]. This phenomenon, usually referred to as quenching of the Gamow-Teller strength, can be due to the sub-nuclear degrees of freedom or to the nuclear configuration mixing [45, 46, 47]. The EXL setup is particularly suited for the study of transitions of this kind via charge-exchange reactions.

Moreover, one of the most important processes that governs the evolution of the core-collapse supernovae is the Gamow-Teller transition. The progress of the rapid-neutron-capture process in supernovae is delayed by the beta decay of the nuclei with magic neutron number. Often the beta decay is a Gamow-Teller transition, whose half-life determines the abundance of the mother nucleus [48].

Fission, vaporisation, multifragmentation, and spallation

The collision of heavy ions can result in concentration of matter in a very small space during a very short time, creating environments of extreme matter density. These environments are ideal for investigations of nuclear-matter dynamics and properties under extreme conditions, very similar to astrophysical objects. The colliding ions can fuse to form a highly-excited quasi-bound compound nucleus. The compound nucleus can decay to the ground state by gamma-ray, nucleon, or cluster evaporation. However, often a compound nucleus decays to one or more fragments.

This decay is called either *fission*, *vaporisation*, or *multifragmentation* depending on the number of fragments and their weights with respect to each other. Each one of these three scenarios occurs in specific states, and there are efforts to develop statistical description of these states by borrowing macroscopic concepts from statistical mechanics [49], like the phase coexistence and the phase transitions.

Multifragmentation is often accompanied by knockout of several neutrons, giving rise to a gas of nucleons around the fragments. This phenomenon gives access to the study of the *liquid-gas phase transitions* in nuclear matter [50]. Another process, significantly less probable than multifragmentation, is when the compound nucleus decays to two or three ions with similar masses. This process is called *fission*. The study of fission process is mainly aimed at the extraction of the fission barrier, the fission dynamics, and the fission rates for different ions [51].

In addition, heavy-ion collisions can result in very strong rotations and shape distortions, which makes the problem more complicated, but also gives the possibility to study nuclei produced in excited states with very high spin. *Nuclear spallation* is another possible outcome of the collision of a heavy ion with another heavy or light ion at high energies, in which the heavy ion disintegrates to many light fragments and free nucleons [52]. Spallation reactions are important not only for their applications as neutron sources [53], but also for their implications in understanding the cosmic rays abundances of elements [54].

The R^3B setup will be well suited to study this large range of nuclear and astrophysics problems of interest; whereas, the EXL setup is limited by the target structure, and many of the heavy-ion reactions will not be accessible there.

2.2 Spectroscopic studies using nuclear reactions

The study of nuclear reactions provides a way of investigating static and dynamic properties of atomic nuclei. A nuclear reaction is a process in which a nucleus interacts with another nucleus, subatomic particles or photons. The end result of a nuclear reaction depends on the properties of the initial particles and the reaction mechanism involved. In this thesis, we are mostly interested in extracting the nuclear spectroscopic factors from the quasi-free scattering data. One of the most common theoretical approaches to the reaction observables is the Distorted-Wave Born Approximation (DWBA), that calculates the transition probability of the reaction, taking into account the wave functions of two particles in both entrance and exit channels [55].

Since the proton-induced quasi-free knockout reactions occur at large beam energies ($E \gtrsim 100$ MeV/u) [56], the interaction time is shorter than the time it takes for the projectile to transit the target nucleus. Therefore, the de Broglie wavelength of the projectile is close to the size of a nucleon. In such a reaction, the *eikonal approximation* is valid which states that when the incident energy, E, is much larger than the scattering potential, V,

$$E \gg |V|,$$

it is fair to assume that the projectile's trajectory is a straight line [57]. Further simplification can be achieved if we assume that the reaction occurs *adiabatically* [58, 59]. This assumption relies upon the fact that the velocity of the beam ion is much larger than the velocity of the nucleons inside the nucleus. In an adiabatic knockout reaction, the structure of the target nucleus remains unchanged during the reaction, and therefore, the momentum vector of the residual fragment is in the opposite direction of the knocked-out nucleon with the same magnitude.

Nuclear spectroscopic factors are known to be the best tools for getting an account of the occupancies of the single-particle states [60]. The theoretical definition of the spectroscopic factors and the experimental formula for extracting them will be given in the next subsections.

Spectroscopic factors

From a theoretical point of view, the spectroscopic factor of a single-particle state (l, j), for the removal of a nucleon, $S^A_{A-1}(lj)$, is defined as the norm of the radial overlap function between states $\langle A-1|$ and $|A\rangle$,

$$S^A_{A-1}(lj) = \Big| \int \sum_n \langle A-1 \| a_{nlj} \| A \rangle \phi_{nlj}(r) \Big|^2 \tag{2.1}$$

where n, l, j, and A represent the number of nodes in the wave-function, the orbital angular momentum, the total angular momentum, and the mass number, respectively. a_{nlj} is the annihilation operator and ϕ_{nlj} is the radial single-particle basis function. The contribution of different combinations is summed over discrete states and integrated over the continuum states [61].

The spectroscopic factors as defined in Equation 2.1 are conceived as the fraction of a nucleon wave function that can be interpreted as a single-particle or a single-hole state on top of an inert core. In an ideal case, in which all nucleon states are perfect single-particle states, the spectroscopic factor for a specific (l, j) is always unity. But since in the real world the nucleons are not independent of each other, this factor is reduced. In order to calculate the spectroscopic factors, the A-nucleon wave functions $\langle A-1|$ and $|A\rangle$ must be built using the time-independent Schrödinger equation. However, the Schrödinger equation of an A-nucleon system with a realistic Hamiltonian is almost impossible to solve. Therefore, approximation methods have to be employed. The ground-state wave functions are obtained using the Hartree-Fock method. Then, different excitations should be included in the wave-functions which require inclusion of the nuclear correlations using a many-body theory such as Random-Phase Approximation or Coupled-Cluster approach [62, 63].

The spectroscopic factors defined in Equation 2.1 are not experimental observables. Nevertheless, the experimental observables, namely absolute cross sections, can give an account of the spectroscopic factors, C^2S, based on the following formula [64]:

$$\sigma(nj^\pi) = \left(\frac{A-1}{A}\right)^2 C^2S(nj^\pi)\, \sigma_{sp}(S_N + E_x(nj^\pi)) \tag{2.2}$$

where $\sigma(nj^{\pi})$ is the cross section of the removal of a nucleon from a state with spin-parity J^{Π}. $\sigma_{sp}(S_N + E_x(j^{\pi}))$ is the calculated cross section using an independent-particle shell model. S_N and E_x are the separation energy of the nucleon and the energy of the state, respectively, and C is the isospin coupling (Clebsh-Gordan) coefficient.

Experimentally, we measure deviation of the spectroscopic factors from unity by a reduction (or quenching) factor defined as [60]

$$R = \frac{\sigma_{exp}}{\sum_{nj^{\pi}} \sigma(nj^{\pi})}. \tag{2.3}$$

The sum is over all the final states available to the knockout residue that lie below the nucleon separation thresholds, and σ_{exp} is the *inclusive* cross section of the knockout reaction. Here, "inclusive" refers to the integration over all the bound states available to the reaction fragments. The integration over the final states is necessary because our experimental setup does not resolve the bound states from each other, and thus we account for all of them by integration. Moreover, the states above the neutron separation threshold decay before they are measured, and therefore, we are limited to the states below the threshold.

Equations 2.2 and 2.3 give a model-dependent method of determining the spectroscopic factors. Although this makes it challenging to compare the experimental and theoretical spectroscopic factors (Equations 2.3 and 2.1, respectively), it provides an opportunity to test the compatibility of different models.

Three different nucleon removal reactions are employed for measurements of the spectroscopic factors: electron-induced proton knockout reactions (e , $e'p$), transfer reactions, and quasi-free nucleon knockout reactions. The electron-induced knockout reactions are sensitive to the whole volume of the nucleus from surface to the centre, and therefore they are ideal for studying the sensitivity of the spectroscopic factors to the radius. However, they cannot be used for neutron removal, and also not for unstable nuclei[3]. Hadronic probes as in transfer reactions or quasi-free reactions are complementary to the electron-induced reactions, and they allow the extraction of spectroscopic information from any state. But the draw-back of the hadronic reactions is that they are mostly peripheral, and have a very low sensitivity to the interior volume of the nucleus [65, 66]. The surface domination of spectroscopic information stems from the strong absorption of hadronic probes in the nucleus [1]. This absorption is less pronounced at radii with lower density which result in the high sensitivity of hadronic probes to the surface. In the quasi-free reactions such as (p , $2p$), a higher sensitivity to the interior of the nucleus can be achieved compared to the transfer reactions because of the high beam energies. Another problem of the hadronic probes is that they entail much more complicated theoretical calculations.

Measurements of the spectroscopic factors in unstable nuclei have led to a prominent and intriguing observation: *the quenching of the spectroscopic factors of a nucleon*

[3]The future electron-ion colliders such as ELISe at FAIR and ELIC at CEBAF will provide the possibility of electron-induced proton knockout from unstable ions.

depends on its orbital momentum, l, and binding energy [67, 68]. Figure 2.1 from Reference [68] presents a compilation of the measurements on the reduction of spectroscopic factors over the last few decades, for both stable and unstable nuclei. In this plot the measured spectroscopic factors, R_S, are shown versus the difference of proton and neutron separation energies, ΔS. The blue and red points indicate the reduction factors for proton and neutron states, respectively.

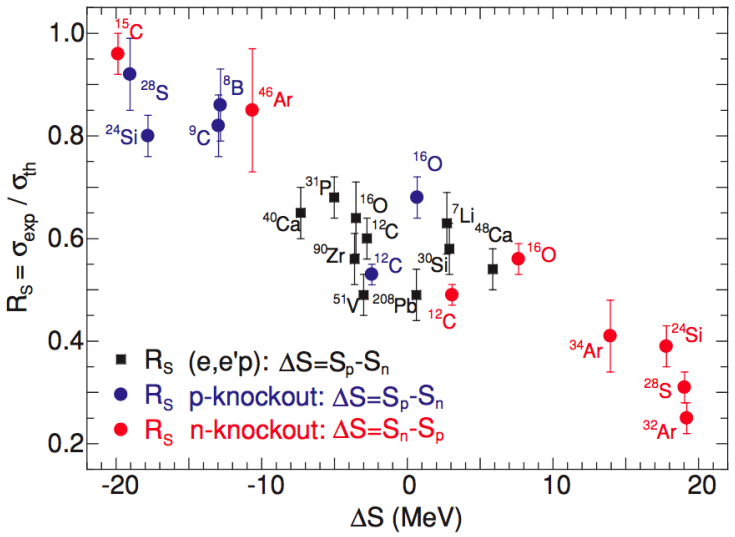

Figure 2.1: Dependence of the reduction factors, R_S, on the nucleon binding energy from measurements. Vertical axis shows the reduction factor and horizontal axis shows the difference between proton separation energy and that of neutron, ΔS. (Picture from Reference [68].)

It is apparent from this figure that the neutron-state spectroscopic factors (red points) for neutron deficient species (like ^{28}S) show a high reduction, while for the proton states (blue points) of the same species spectroscopic factors are not quenched considerably. In other words, *the spectroscopic factors of the nucleons of the deficient species (and hence deeper bound) are more quenched*. It can thus be suggested that the wave function of the nucleon of the deficient species is fragmented into higher states, so that it compensates for its shortage in the nucleus and hence increase stability.

A theoretical study of the spectroscopic factors for oxygen isotopes [61] manifests the same trend. The calculations are depicted in Figure 2.2. As a way of example, we take ^{24}O, which is at the neutron drip line, and its protons are deeply bound while its neutrons are loosely bound. It turned out in the calculation that the spectroscopic factors of proton states (shown in black circles) are highly quenched, but neutron states have spectroscopic factors close to unity. These calculations were performed for the $1p_{1/2}$ proton and neutron states, using *ab-initio* coupled-cluster theory. By comparing Figures 2.2 and 2.1, we observe that the spectroscopic factors obtained from the *ab-initio* calculations are not as strongly quenched as the ones observed in the experiments. For example, the theoretical calculations give a quenching factor of 0.86 for the $1p_{1/2}$ proton states in ^{16}O, while it was found to be 0.6 – 0.7 in the ex-

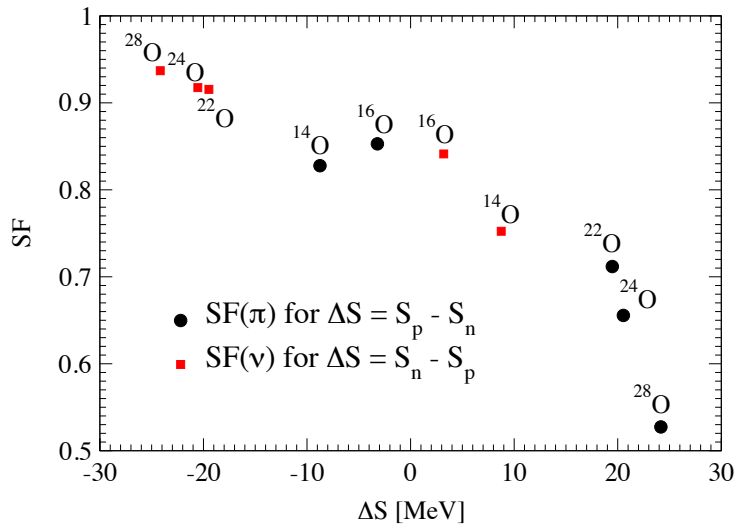

Figure 2.2: The same as Figure 2.1 but for the $1p_{1/2}$ states of oxygen isotopes from a theoretical calculation. (Picture from Reference [61].)

perimental studies. Thus, more studies are necessary to understand the quenching mechanism of the reaction cross sections.

The R^3B and EXL projects create a unique opportunity to investigate the quenching of the spectroscopic factors of unstable nuclei as a function of the ratio between the proton and neutron numbers. The major part of this thesis is dedicated to an experiment with the LAND-R^3B setup, and is aimed at the determination of the spectroscopic factors of the oxygen isotopes. This setup is a predecessor of the R^3B setup and is explained in Chapter 4.

Chapter

In-beam Test of the EXL Demonstrator at KVI

On the way to the construction of the EXL detection system [21], several preparatory experiments have been performed. One of these experiments was to test the response of some of the detectors that will be used in the future EXL detection system. In this test experiment, these detectors were arranged in a so-called *demonstrator*, and were irradiated with a proton beam at the cyclotron facility of KVI.

The demonstrator was composed of two Double-sided Silicon Strip Detectors (DSSD), two lithium-drifted silicon (Si(Li)) detectors, and two CsI scintillators, altogether representing a module of the EXL Silicon Particle Array (ESPA) and the EXL Gamma and Particle Array (EGPA) (see Figures 3.1 and 3.2). Each DSSD has 64 strips on each side, from which every four strips were connected to one read-out channel, thus giving rise to 16 effective strips on each side. The surface area of each DSSD is 2×2 cm^2, with a thickness of 0.3 mm. The DSSDs were used for tracking purposes as well as ΔE energy-deposit measurements. The Si(Li)s were used for energy measurements and each of them has dimensions of $80\times50\times6.5$ mm^3. Each Si(Li) is divided in eight pads; the four central pads of Si(Li)#1 and one pad of Si(Li)#2 were connected to the data-acquisition system. The CsI scintillators were used for energy measurements. Each CsI scintillator has a trapezoidal shape with a length of 11.5 cm, area of 2×1 cm^2 on the front face, and area of 3×1.5 cm^2 on the rear side. The two scintillators were connected to a double photomultiplier via a thin light guide. While the scintillation light of each scintillator was collected by a separate photomultiplier, they shared the same light guide. The light guide, the blue volume in Figure 3.1, is a very thin layer of glass that was used to improve the optical contact.

A proton beam was accelerated to a nominal energy of 133 MeV and impinged on the demonstrator. The comparison of the calibrated spectra and simulations, showed that the beam energy was around 4 MeV higher than the nominal value of 133 MeV (see Subsection 3.3.3). In order to test the response of the demonstrator at a different energy, a reduced energy of around 70 MeV was obtained using an

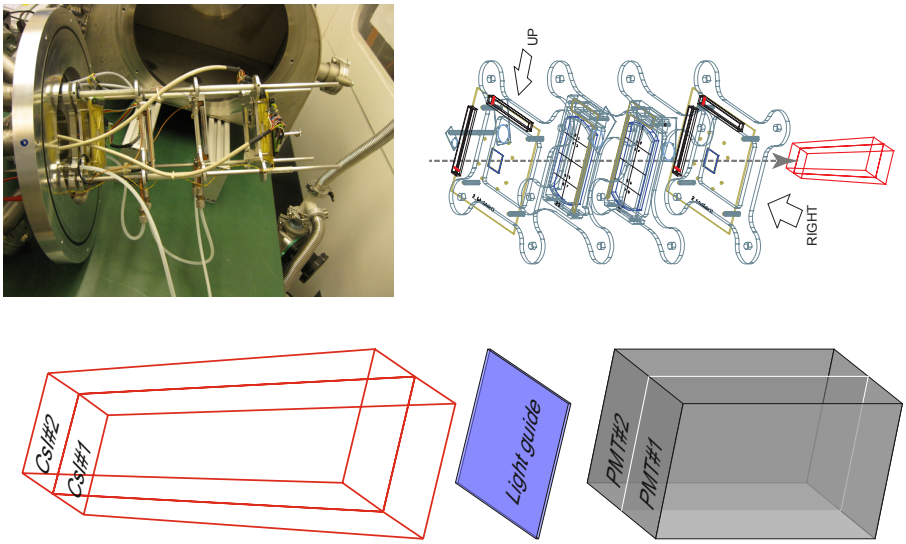

Figure 3.1: Top left: the silicon detectors before mounting in the vacuum chamber. Top right: The computer drawing of the detection system adapted from Branislav Streicher (Private communication). Bottom: the schematic view of the constituents of the CsI scintillation detectors. The thin blue volume demonstrates the light guide that was used to enhance the optical connection.

aluminium brick as a degrader. The thickness of the brick was 42.6 mm, and it was placed in the beam line just before the setup. At the end of the experiment, the CsI scintillators were placed in front of the chamber and irradiated directly for calibration purposes.

For convenience, we label the different parts of the experiment as follows[1]:

- run 3: the test of the whole set of detectors with full-energy beam (around 137 MeV),
- run 4: the same as run 3 with the aluminium brick in the beam line (reduced beam energy of around 70 MeV),
- run 5: calibration of the CsI scintillators with full-energy beam,
- run 6: calibration of the CsI scintillators with reduced-energy beam.

In the following sections, the procedures of simulation, calibration, and the total-energy reconstruction of the experiment are explained.

3.1 Simulation of the experiment

This experiment was simulated with `Geant4.9.4` [69]. The simulated geometry for run 3 is shown in Figure 3.2, in which the green box is just a separation of vacuum

[1]The run numbers are based on the chronological order of the experiment, after two beam-adjustment runs.

and air in the simulation and it does not represent the real vacuum chamber. The entrance and exit foils of the chamber were included in the simulation. The blue squares show the PCB read-out boards of the silicon strip detectors (DSSDs), and the strip detectors are the small squares in the middle of the boards. The long thick arrow in the middle shows the beam direction.

The primary particles are generated as a cylindrical beam with no divergence. The position distribution at which the particles are generated is a uniform random function along two perpendicular axes to the direction of the beam. The primary energy of particles was simulated with a Gaussian distribution with a width of $\sigma = 0.3$ MeV. Different sets of simulated data were obtained by assumption of different energies of 133 and 137 MeV as the initial beam energy. The `PhysicsList` in this simulation includes different electromagnetic and hadronic interactions. In this section, only the results of the simulation with 133-MeV protons are given and the ones with 137-MeV protons are presented in Table 3.4. The centroid and the full width at half maximum (FWHM) of the simulated spectra of each detector are given in Table 3.1.

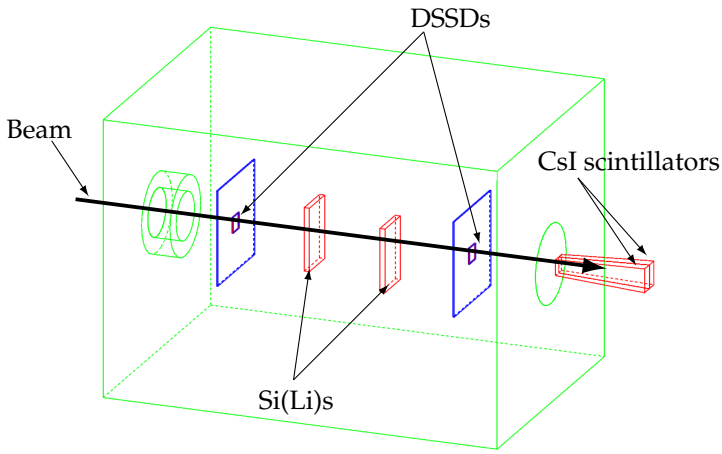

Figure 3.2: The geometry of the detectors in the EXL demonstrator test. The long thick arrow in the middle shows the direction of the beam.

3.2 Calibration

The energy calibration process of the silicon detectors (DSSDs and Si(Li)s) relies on the use of radioactive sources, emitting alpha particles with known energies. The zero offset of the spectra was eliminated using a set of pulser data for each output channel. In the following sections, the calibrated spectra of the detectors are presented and compared with the simulation results.

Table 3.1: The simulated energy deposit of the proton beam in each detector, in each run. "Total" is the sum of the energy deposit of the beam in the detectors, which was summed event-by-event. "All" is the sum of the energy deposit in all of the elements in the simulation, including passive materials, such as air and foils. The spectra of both DSSDs in run 3 and DSSD#1 in run 4 are fitted with Landau distribution and their FWHM is approximated as 2.35 of the width (σ). For all other spectra a Gaussian distribution was used.

Detector	Energy [MeV]	FWHM [MeV]
run 3 (133 MeV)		
DSSD#1	0.28	0.05
DSSD#2	0.31	0.06
Si(Li)#1	7.4	0.84
Si(Li)#2	7.7	0.86
Scintillators	116.2	1.6
Total	132.0	0.82
All	133.0	0.7
run 4 (66.5 MeV)		
DSSD#1	0.51	0.10
DSSD#2	0.90	0.18
Si(Li)#1	13.5	1.3
Si(Li)#2	17.3	2.1
Scintillators	32.5	7.5
Total	64.8	3.5
run 5 (133 MeV)		
Scintillators	132.5	0.8
run 6 (66.5 MeV)		
Scintillators	65.7	3.5

DSSDs

Each DSSD has 32 output channels that were calibrated strip by strip for both DSSDs. For DSSD#1, a ^{148}Gd source and for DSSD#2 an ^{241}Am source were used to calibrate the spectra of each strip. The energies of the emitted alpha particles are given in Table 3.2 for all sources. The calibrated spectra of a typical DSSD strip in run 3 and run 4 are shown as black solid histograms in Figure 3.3, and the simulated spectra are shown as dashed grey. In each spectrum there are two peaks; the one at lower energies is due to the beam, and the one at higher energies is due to the radioactive source. Although the experimental spectrum matches the simulated one in run 3, it shows some deviation in run 4. This will be discussed further in Subsection 3.3.3.

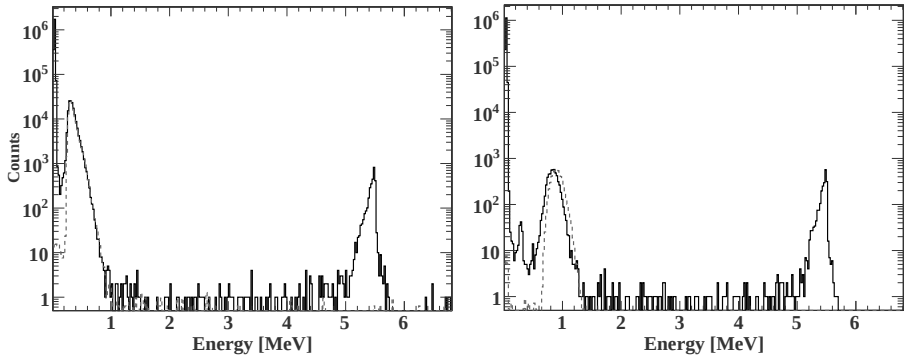

Figure 3.3: The energy spectrum of strip#10 of DSSD#2 in run 3 (left) and run 4 (right). The dashed lines show the results of the simulation. The response of the radioactive source was not simulated.

Table 3.2: The energy of the emitted alpha particle in the dominant decay mode of the radioactive sources.

radioactive source	energy of the emitted alpha [keV]
^{148}Gd	3183
^{241}Am	5485
^{244}Cm	5805
^{239}Pu	5157

Si(Li)s

Four pads of Si(Li)#1 and one pad of Si(Li)#2 were used and connected to the data-acquisition system. For the calibration of Si(Li)#1 an ^{241}Am and for Si(Li)#2 a mixed radioactive source were used. The mixed radioactive source included ^{241}Am, ^{244}Cm and ^{239}Pu (see Table 3.2). The calibrated spectra of the Si(Li)s are depicted in Figure 3.4 and Figure 3.5 for run 3, and Figure 3.6 and Figure 3.7 for run 4, along with the simulated spectra. In all of these spectra, the sharp peaks around 5 MeV are from the radioactive sources. In the spectra of Si(Li)#2, the events that do not fall under the main peak are mostly caused by multiple scattering and hadronic interactions of the beam in the detectors. This can be verified using the simulation. If the multiple scattering and hadronic interactions are deactivated in the simulation, only the events under the main peak remain. The simulated spectra of run 4 show a significant disagreement with the experimental ones, and likewise for run 3 but to a lesser extent. This is most probably due to the wrong beam energy in the simulation, which will be discussed further in Subsection 3.3.3.

In the experimental spectra of the Si(Li)s, there are some low-energy peaks ($E <$ 2 MeV), that are not due to the beam. Figure 3.8 shows the spectrum of Si(Li)#2 in three histograms, subjected to three different analysis conditions. The first condition (dotted histogram) is setting the trigger to an OR of the Si(Li)s and no other element

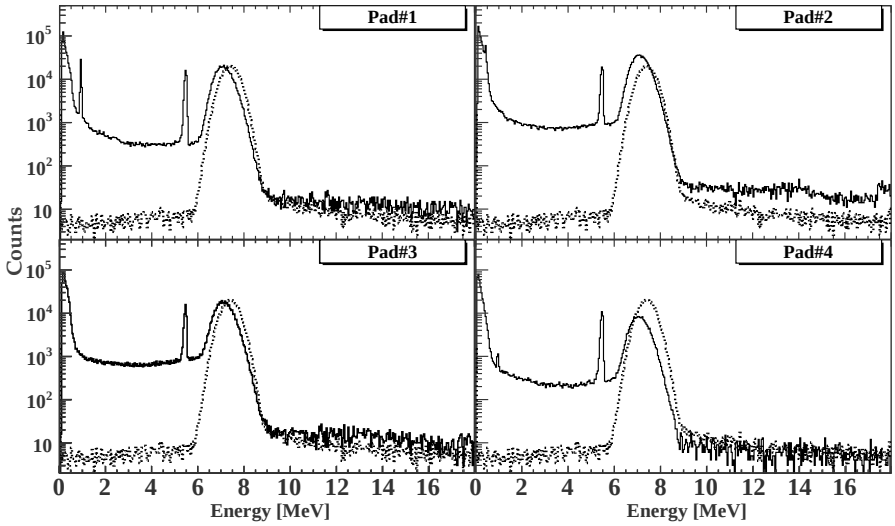

Figure 3.4: The energy spectra of four pads of Si(Li)#1 in run 3. The dotted histogram shows the simulated spectra.

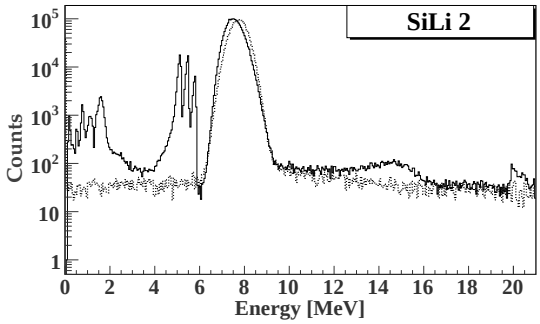

Figure 3.5: The energy spectrum of Si(Li)#2 in run 3. The dotted histograms show the simulated spectrum. The bump at $E \sim 15$ MeV is due to pileup events.

firing, which almost excludes the events that are caused by the beam. The second condition (solid black histogram) is setting the trigger to an AND of all the detectors, which excludes the events that are not caused by the beam. The last condition (grey histogram) is constraining the events to a small region, in the middle of the DSSDs, while satisfying the same trigger as for the solid black histogram. This last condition is a more strict condition for excluding all events, that are not due to the beam.

Clearly, all low-energy peaks have disappeared with this condition, showing that these are not beam-related. There may have been a problem in the electronics readout system, as was the case in the first EXL demonstrator test [70].

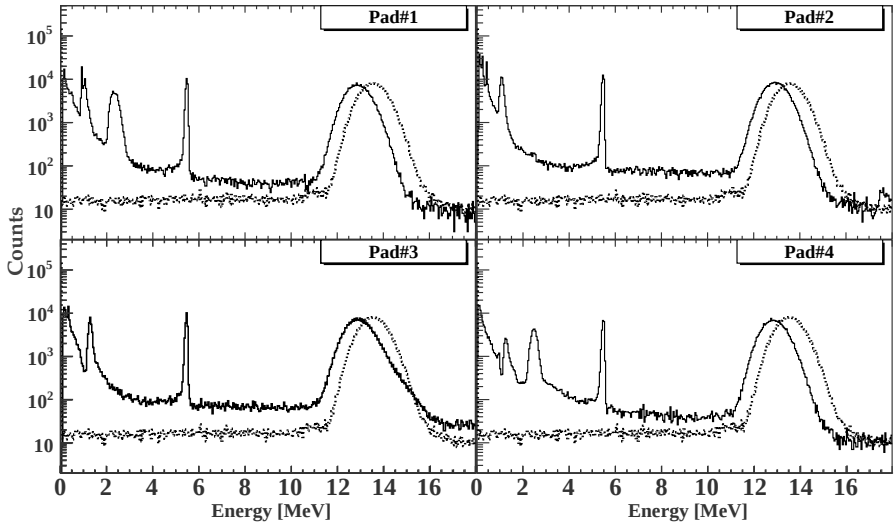

Figure 3.6: The same as Figure 3.4 but for run 4.

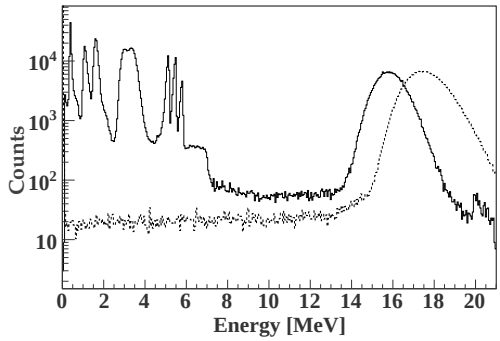

Figure 3.7: The same as Figure 3.5 but for run 4.

CsI scintillators

Figure 3.9 shows the raw spectrum of the energy signals of CsI#2 versus CsI#1 in run 3. Two peaks are labelled as 1 and 2. Peak 1 shows the events that stopped in CsI#1 and their corresponding scintillation light leaked to CsI#2 and vice versa for peak 2. The events that lie on the line between these two peaks are the protons crossing from one scintillator to the other one. The events that lie on the line between each peak and the origin are due to the hadronic interactions [71].

At the end of the experiment, the CsI scintillators were placed in front of the chamber and irradiated directly with the beam (both full-energy and reduced-energy beams). Since part of the scintillation light in each of the CsI crystals leaked to the neighbouring crystal, the calibration of these detectors is not as straightforward as for the other ones. In order to calibrate them, the data of run 5 were used and

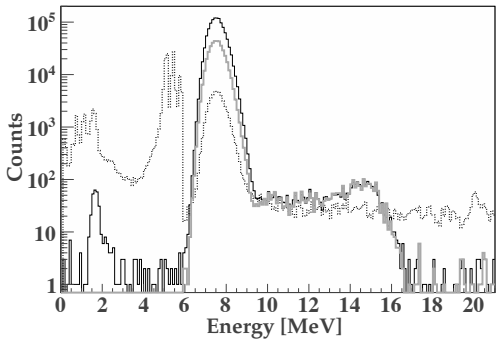

Figure 3.8: The energy spectrum of Si(Li)#2 in run 3, subjected to three different analysis conditions: 1) an OR of the Si(Li)s (dotted histogram), 2) an AND of all detectors (black histogram), and 3) the same as 2 plus a constraint on the position of the particles, to hit the centre of the DSSDs (grey histogram).

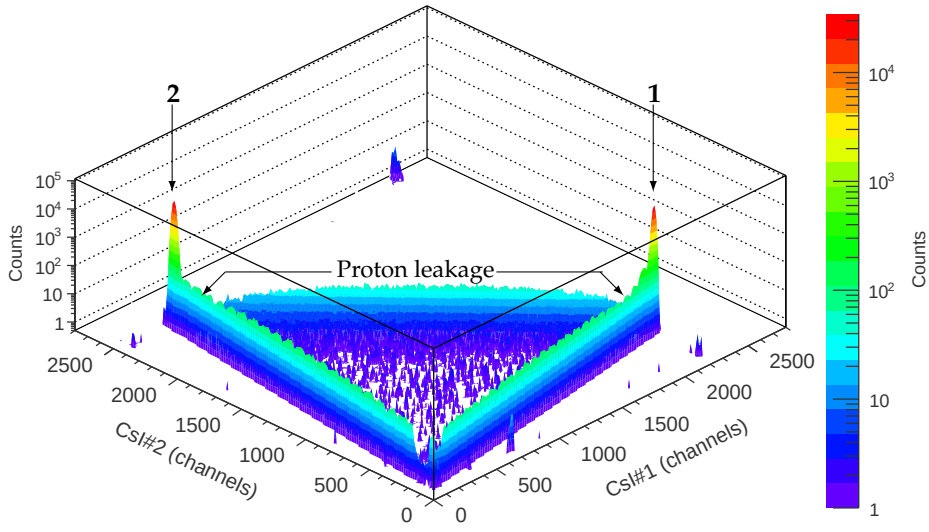

Figure 3.9: The raw spectrum of the energy signals of CsI#2 versus CsI#1; peak 1 is the proton peak in CsI#1 and the light-leakage peak in CsI#2 and similarly for peak 2.

two methods were applied. These methods will be discussed further.

First method: adding the leakage

Since the peak positions in the spectra of the two scintillators do not match, the spectrum of CsI#1 was shifted in order to match the one of CsI#2. For this purpose, we rely on the fact that the sum of the beam energy signal in one crystal and its leakage signal in the other crystal should give the total beam energy while entering

the CsI scintillator,

$$\begin{aligned} f_1 E_{1l} + f_2 E_{2p} &= E_t \\ f_1 E_{1p} + f_2 E_{2l} &= E_t \end{aligned} \tag{3.1}$$

f_1 and f_2 are the matching factors for CsI#1 and CsI#2, respectively. E_{1l} and E_{1p} are the peak positions of the light-leakage peak and proton peak in the spectrum of CsI#1, respectively, and similarly for E_{2l} and E_{2p}. Therefore, the energy deposit of each event in CsI#1 is multiplied by a matching factor that is obtained from,

$$\text{Matching Factor} = \frac{f_2}{f_1} = \frac{E_{1p} - E_{1l}}{E_{2p} - E_{2l}}.$$

This matching factor is applied to the CsI#1 energy signals. Then the matched data of CsI#1 are added to the data of CsI#2 event by event. The resulting spectrum has only one peak which represents the sum of each proton signal with its leakage in the other crystal. In run 5, the mean value of this peak should be equal to 132.5 MeV, which is the energy of the 133-MeV beam after passing through $\sim$1 m of air. This gives us the calibration factor for the CsI scintillators.

The calibrated spectra of both scintillators are depicted in Figure 3.10, left column. The right column shows the sum spectrum of the energies of CsI#1 and CsI#2, which was obtained event by event. The upper and lower rows are the results of run 3 and run 4, respectively.

Second method: ignoring the leakage

In the first method of calibration, the leaked light was added to the main signal of protons, in order to integrate all the energy deposited in the scintillators. However, it is a known fact that always part of the scintillation light will be lost due to the attenuation of light in the crystal or escape of photons from the crystal boundaries. This missing energy is always compensated by considering a larger calibration factor. Likewise, for the calibration of the CsI scintillators in our setup we can consider the leaked scintillation light as lost, and compensate for it by a larger calibration factor.

In this way, we only consider the main peak of the spectrum for the calibration of the scintillators. It means that after subtracting the zero offset, the peak position of the raw spectrum is multiplied by a calibration factor that results in a peak energy at 132.5 MeV for run 5. Figure 3.11 shows the calibrated spectra of CsI scintillators in run 3 and run 4 using this method.

A final decision on the quality of the two methods requires more knowledge about the response of the CsI crystals to the protons in the energy range of this experiment. If the leaked light should be included in the calibration, the process of the leakage should be better understood. Specifically, the amount of energy that is lost due to the leakage should be known and corrected for.

In the next section, it is shown that the second method results in a better energy resolution for the total-energy reconstruction.

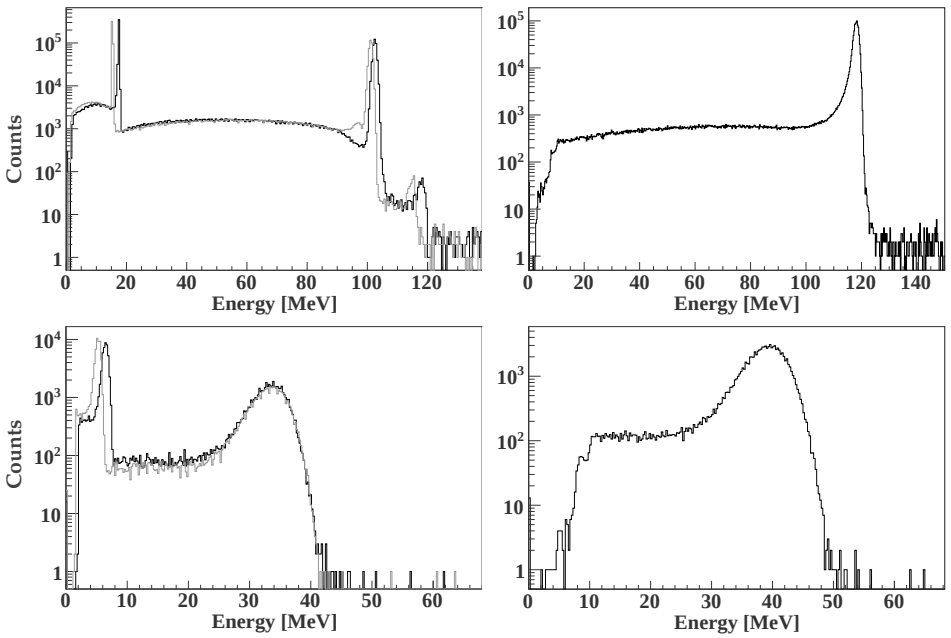

Figure 3.10: Left column: The calibrated energy spectra of CsI#1 (grey) and CsI#2 (black) scintillators. Right column: The sum of the energy of CsI#1 and CsI#2 scintillators. Top and bottom panels are the results of run 3 and run 4, respectively. For the energy calibration, the data of run 5 were used, and also the leaked light was included.

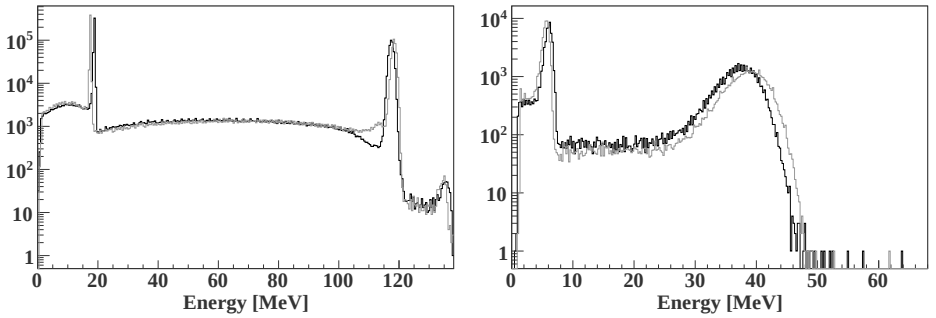

Figure 3.11: The energy spectra of CsI#1 (grey) and CsI#2 (black) scintillators in run 3 (left) and run 4 (right). The leaked light is ignored in the calibration.

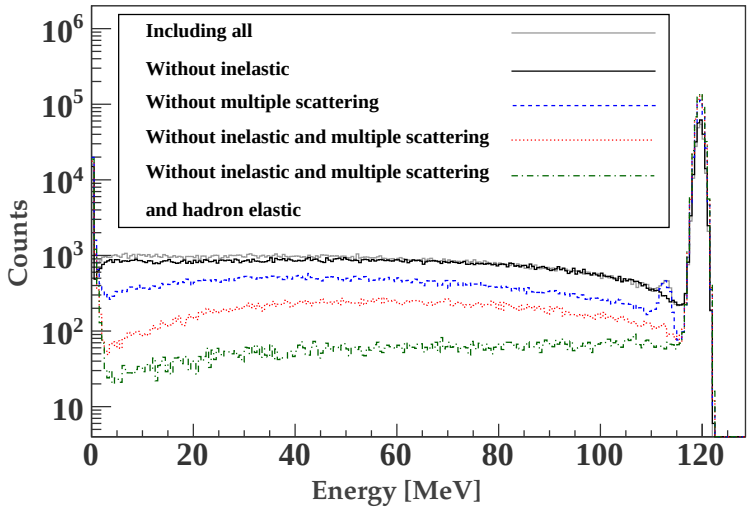

Figure 3.12: The simulated energy spectra of CsI#2, using different sets of active processes.

3.3 Analysis

3.3.1 Events in the plateau region of the CsI spectra

The data in Figure 3.10 are shown under a trigger selection that accepts the events that passed through all detectors of the setup. Therefore, all of the events in these spectra are due to the beam. These spectra exhibit the proton peak and the continuum which extends almost to zero, and the number of events in the continuum is nearly the same as the number of events in the peak region. The origin of these events was investigated using several simulations, with different physics processes. By deactivating different physics processes in each simulation, different spectra were obtained for the CsI scintillators. Three major physics processes were taken into account: hadron elastic interactions, inelastic interactions and multiple scattering.

Figure 3.12 shows five simulated spectra of CsI#2, obtained from five different simulations. These simulations only differ in their active physical processes. The grey histogram shows the result of the main simulation, in which all the processes in the `PhysicsList` are active (see Section 3.1). The solid black histogram is the result of deactivating the inelastic processes, and the dashed (blue) histogram is the result of deactivating multiple scattering. The dotted (red) histogram shows the result of deactivating both multiple scattering and the inelastic processes. Finally, the dotted-dashed (green) histogram is the result of deactivating the three physical processes: multiple scattering, inelastic scattering, and hadronic-elastic processes. It must be noted that the `PhysicsList` of the simulation contains many other processes that are not deactivated, and therefore, they cause the remaining continuum in the green histogram. Figure 3.12 suggests that the plateau events are because of a combination of different physical processes.

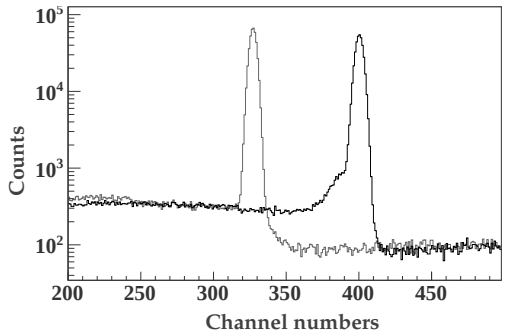

Figure 3.13: The raw spectrum of CsI#2 (CsI#1), zoomed in the region of the light-leakage peak, is shown in the black (grey) histogram.

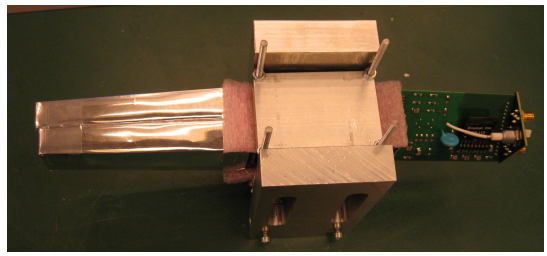

Figure 3.14: The CsI scintillators with their photomultipliers (in the middle) and the preamplifier circuit (right).

3.3.2 Unusual peak in the spectrum of CsI#1

There is a small peak, just below the proton peak in the spectrum of CsI#1 that does not have a counterpart in CsI#2 (see Figure 3.10, top left panel). The light leakage of this peak appears in the spectrum of the other scintillator as a broadening of the light-leakage peak, as is illustrated in Figure 3.13, which shows the raw spectrum of both scintillators, zoomed in the region of the light-leakage peak. Therefore, the small peak is due to a scintillation process in the crystal of CsI#1. However, this peak does not appear in the spectrum of CsI#2.

Figure 3.14 shows a photograph of the CsI scintillators, wrapped in foils and coupled to the photomultipliers via a thin light guide. It can be seen that the front faces of the detectors are not exactly in line. This imperfection in the geometry of the scintillators could be the reason for the small peak in CsI#1. Nevertheless, more investigations have been done trying to pinpoint the origin of this peak. For example, a conjecture about this peak was a misalignment of the CsI scintillators with respect to the beam direction. The position information of the DSSDs was used to see whether the events causing this peak occur in the vicinity of the surface between the two scintillators, or if they occur in the centre of CsI#1. It turned out that those events occur almost everywhere in the scintillators. Therefore, even if there was a misalignment, it was not the cause of the small peak. On the other hand in the simulated spectra in Figure 3.12, this peak appears only in the spectra with inelastic

processes, which implies that the peak was probably due to inelastic reactions in the CsI crystals. After all, the exact origin of this peak remains unknown, and these ambiguities in the spectra of the scintillators necessitate more comprehensive tests, in order to improve the calibration and the energy resolution of the detection system. All the components of these detectors including each of the CsI crystals, their photomultipliers, and the preamplifier board have to be taken apart and tested separately before connecting them together.

3.3.3 Discrepancies between simulated and experimental data

Table 3.3 presents the centroids and the widths of the peaks in the spectrum of the beam in each detector, obtained from a Gaussian fit. The results of run 3 and run 4 are given, and the calibration of the scintillators is presented with both methods as explained in Section 3.2. The statistical errors were mainly the fit errors, and were estimated by $\sigma/\sqrt{N}$ for each Gaussian fit, in which N is the number of points used for the fit, and σ is the width of the fitted distribution. This error is around 0.1% for the scintillators and the DSSDs, and around 1% for the Si(Li)s, at the quoted energy for each detector.

The systematic errors are caused, to a great extent, by the manual choice of the fit interval. Since the full range of the experimental spectra does not resemble a Gaussian distribution, a small region around the peak of each spectrum is selected for the fit. Different choices of the fit interval can result in slightly different values of the deposited energy and the width. In order to evaluate this effect, many Gaussian distributions are fitted to different ranges in each spectrum, around the peak, producing a set of mean values (energy deposits in our case). The standard deviation of the obtained set of mean values was used as a measure of this systematic error, which is around 0.5% for the Si(Li)s and around 0.4% for the scintillators, at the quoted energies.

The comparison of the experimental and simulated data (Tables 3.1 and 3.3) shows that the simulation results do not reproduce the results of the experiment. Although, the general shape of the simulated spectra agrees reasonably well with the experimental ones, the energy losses of the beam in the detectors do not match properly. Indeed, the simulated energy deposits in the silicon detectors are higher than in the experimental data and inversely in case of the scintillators. According to the Bethe-Bloch formula for energy loss, if the initial energy of the beam in the simulation was higher, the protons would have lost less energy in the silicon detectors. Following this speculation, the same simulation was carried out but with a higher incident energy of 137 MeV.

Table 3.4 shows the results of this simulation. The agreement with the experimental data improves significantly in case of the Si(Li)s and to a lesser extent in case of the DSSDs; see Figures 3.17 and 3.18 (compare with Figures 3.4 and 3.5, respectively). In these figures, the experimental data are shown under a trigger condition that chooses events originating from the beam. In the simulated data, some energy conditions on the other detectors define a similar condition as the experimental trigger.

Table 3.3: The energy deposit of the proton beam in each detector, in runs 3 and 4. The numbers for the DSSDs are averaged over all strips of each side. The calibration of the scintillators is presented with both methods, explained in section 3.2: including the leakage and ignoring it. Notice that the calibration coefficients for the scintillators are obtained from run 5, assuming a beam energy of 133 MeV. The statistical uncertainties were estimated to be around 0.1% for the scintillators and the DSSDs, and around 1% for the Si(Li)s. The systematic uncertainties are less than 1%.

Detector	Energy	FWHM
run 3		
DSSD#1 [keV]		
p-side	280	86
n-side	190	63
DSSD#2 [keV]		
p-side	320	110
n-side	260	100
Si(Li)#1 [MeV]		
average of four pads	7.1	0.83
Si(Li)#2 [MeV]		
one pad	7.5	0.86
CsI scintillators [MeV]		
include leakage	118.1	2.1
ignore leak., CsI#1	118.3	1.6
ignore leak., CsI#2	117.4	1.7
run 4		
DSSD#1 [keV]		
p-side	510	150
n-side	380	120
DSSD#2 [keV]		
p-side	840	210
n-side	760	200
Si(Li)#1 [MeV]		
average of four pads	12.9	1.3
Si(Li)#2 [MeV]		
one pad	15.9	1.7
CsI scintillators [MeV]		
include leakage	39	7
ignore leak., CsI#1	38	7
ignore leak., CsI#2	37	6

Table 3.4: The simulated energy deposit of the proton beam in each detector. Everything is the same as Table 3.1, but the incident beam energy is changed to 137 MeV for this simulation.

Detector	Energy [MeV]	FWHM [MeV]
run 3 (137 MeV)		
DSSD#1	0.28	0.06
DSSD#2	0.31	0.08
Si(Li)#1	7.2	0.85
Si(Li)#2	7.6	0.85
Scintillators	120.5	1.7
Total	136.1	0.80
All	137.0	0.7
run 4 (71 MeV)		
DSSD#1	0.48	0.08
DSSD#2	0.73	0.15
Si(Li)#1	12.4	1.1
Si(Li)#2	15.0	1.5
Scintillators	43.1	6.2
Total	71.2	3.8

Table 3.5: The centroid and width of the peak in the energy spectrum of the scintillators. The incident beam energy is assumed to be 137 MeV.

	Energy [MeV]	FWHM [MeV]
run 3		
include leakage	121.4	2.1
ignore leak., CsI#1	121.9	1.8
ignore leak., CsI#2	121.1	1.7
run 4		
include leakage	39.8	7.1
ignore leak., CsI#1	39.7	7.1
ignore leak., CsI#2	38.5	6.6

It should be noted that the calibration of the scintillators is based on the simulated energy of the incident beam; therefore, increasing the beam energy in the simulation results in larger calibration factors for the experimental spectra of the scintillators, which finally translates to higher energy signals of the scintillators. The calibrated energies of the scintillators with the assumption of a 137-MeV beam are given in Table 3.5. By comparing the scintillator energy deposits in Tables 3.4 and 3.5 we

can see that, assuming a higher beam energy in the simulation does not improve the situation for the scintillators. This simulation has been repeated a few times with different beam energies between 133 and 137 MeV, and in all cases, there is a discrepancy between the simulated and experimental values of the energy deposit in the scintillators between 1 to 3 MeV. It shows that, with the current method of calibration, the simulated energy deposit of the scintillators in run 3 always lies below the experimental values with a significant difference.

Two conjectures were suggested as possible causes of this discrepancy, neither of them explaining it completely: the possible non-linearity of the response of the scintillators or photomultipliers, and the geometrical effects such as the thickness of the Si(Li)s. The assumption of linearity became important when the calibration factors from run 5 were applied to the data of run 3. There, we assumed that the response of the scintillators, including the light yield and leakage effects, varies linearly for different beam energies. In fact, a slightly non-linear response has been observed for a CsI(Tl) scintillator coupled to a photo-diode [72]. But the observed non-linearity in Reference [72] does not explain the disagreement of 1 to 2 MeV observed in this experiment[2]. On the other hand, in Figure 3.9 we can see that the light leakage between our crystals is linear, as expected. Therefore, the linearity of the CsI crystals and the leakage effects are verified within the range of interest in this experiment. Meanwhile, some doubts remain on the linearity of the photomultipliers, which was not tested within the scope of this experiment.

Besides the non-linearity effects, an inaccuracy of the thickness of the Si(Li)s could result in a different energy deposit in the Si(Li)s, and hence cause a discrepancy between simulated and experimental spectra. Specifically, in the simulation with the 133-MeV beam, if it was assumed that the Si(Li)s were a little thinner, 6.3 mm instead of 6.5 mm, the energy loss in the Si(Li)s would be smaller, matching the experimental data. Such an assumption was tested in a simulation. Although, the assumption of thinner Si(Li)s improved the agreement of the simulated Si(Li) spectra with the experimental ones, obviously it did not solve the disagreement of the scintillators.

So far a reliable explanation for this discrepancy could not be provided, and to the best of our knowledge all possible contributing effects except the linearity of the photomultipliers have been looked at.

3.3.4 Total-energy reconstruction

The energy resolution of each detector can be obtained from the given FWHM in Table 3.3. Obviously, the total-energy resolution of the setup is dominated by the CsI scintillators. Therefore, different calibrations of the scintillators result in different resolutions for the reconstructed total energy.

Figures 3.15 and 3.16 show the reconstructed energy spectra of the demonstrator using the first and second methods of calibration of the scintillators, respectively.

[2]It should be noted that in Reference [72] the scintillating crystal is coupled to a photo-diode as compared to the photomultipliers in the current experiment.

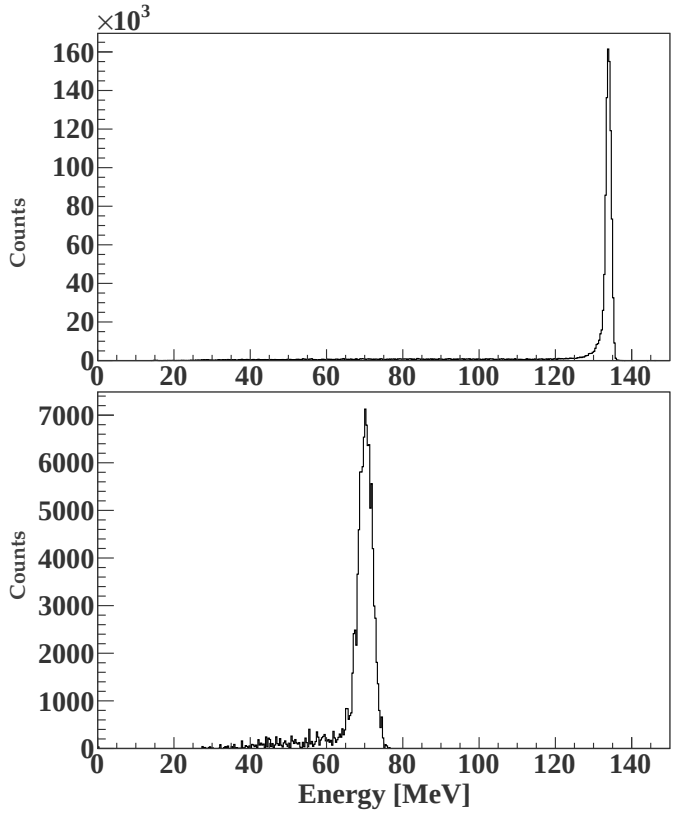

Figure 3.15: Reconstructed total-energy spectra of run 3 (top) and run 4 (bottom). The leaked light is included in calibration of the CsI scintillators.

In both cases, the total-energy reconstruction was obtained by summing the energy deposit of the beam in each detector event by event. The top plot in each figure is for run 3, and the bottom one is for run 4.

Table 3.6 gives the centroid and the width of the peak in the spectra in Figures 3.15 and 3.16. The given FWHM is the result of the energy fluctuations of the incident beam and the energy dispersion of the beam in the detectors. The effect of all passive elements in the beam line (air, the aluminium brick and the foils) was subtracted from the total width. The contribution of these passive materials in energy dispersion of the beam was calculated using simulated data. The width indicates the energy resolution of the demonstrator, which is obviously influenced by different methods of the calibration of the CsI scintillators. Nevertheless, it was expected that when the straggling of the beam in the passive elements is subtracted, the FWHM of run 4 will be roughly the same as that of run 3. But apparently this is not the case, which shows that there are issues in the setup that are not yet understood.

One should pay attention to the fact that the centroids in Table 3.6 depend on the calibration of the CsI scintillators, and this calibration is based on the initial energy

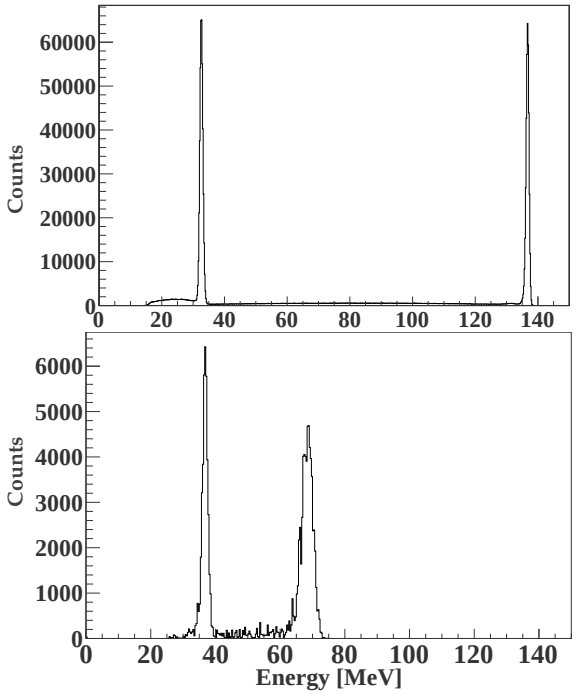

Figure 3.16: Reconstructed total-energy spectra of run 3 (top) and run 4 (bottom). The leaked light is ignored in calibration of the CsI scintillators.

of the beam, which has a considerable uncertainty. The initial energy of the beam was estimated to be roughly a Gaussian distribution with a width of FWHM $\sim$ 1 MeV. Therefore, when the given energy in Table 3.6 is used as a measure of the energy reconstruction of the present experiment, one should take into account that an uncertainty of a few MeV exists in the beam energy.

3.4 Conclusions

One would like to know whether the energy resolution of the demonstrator fulfils the requirements of the EXL design. For this purpose, it should be considered that:

- the obtained energy resolution for the demonstrator is bearing the energy spread of the incident beam which is around 1 MeV;
- the identification of different reaction channels imposes different requirements on the energy resolution of the detection system.

Therefore, it is unwise to make a general comment on the quality of the obtained resolution for all physics goals of EXL. Nevertheless, to get a feeling on how the resolution of the demonstrator compares to the EXL requirements, a single case is

Table 3.6: The centroids and the widths of the reconstructed total-energy for run 3 and run 4. Since the centroid mostly depends on the calibration of the CsI scintillators, it should not be used as an absolute measure of the reconstruction of the initial energy of the incident beam. These numbers are obtained assuming a beam energy of 137 (71) MeV for run 3 (run 4). Notice that the effect of air, aluminium brick and foils on energy dispersion of the beam is subtracted from the total width.

	Energy [MeV]	FWHM [MeV]
run 3 (137 MeV)		
include leakage	136.5	1.6
ignore leak. with CsI#1	137.2	1.2
ignore leak. with CsI#2	136.4	1.3
run 4 (71 MeV)		
include leakage	68.8	3.3
ignore leak. with CsI#1	69.8	3.0
ignore leak. with CsI#2	68.3	2.4

described as follows. First, the energy spread of the beam was subtracted from the energy resolution of the demonstrator in run 3 as

$$\sqrt{1.4^2 - 1^2} \approx 1 \text{ MeV};$$

The width of 1.4 MeV is the average of the values given in Table 3.6 for run 3. Then, we chose, for comparison, a typical reaction channel such as ^{136}Xe(p , p') with a beam energy of 350 MeV/u and an excitation energy of $E^\star = 15$ MeV. The simulations and theoretical calculations for this reaction channel were performed and presented in the Ph.D. dissertation of H. Moeini [73], Table 3.1. The table gives the expected resolution for the EXL setup, in order to distinguish two different states of ^{136}Xe with a 300 keV energy difference at different scattering angles. For example, in the scattering angle range of 35.1° to 52.6° in the centre-of-mass frame (corresponding to 55° to 65° in the LAB frame) an energy resolution of 510 to 530 keV is required to identify two states 300 keV apart. Therefore, if a set of detectors such as the one tested here is going to be placed in the angular range of 55° to 65° in the LAB frame, its total energy resolution should be two times better than obtained in this test experiment in order to separate the two energy levels.

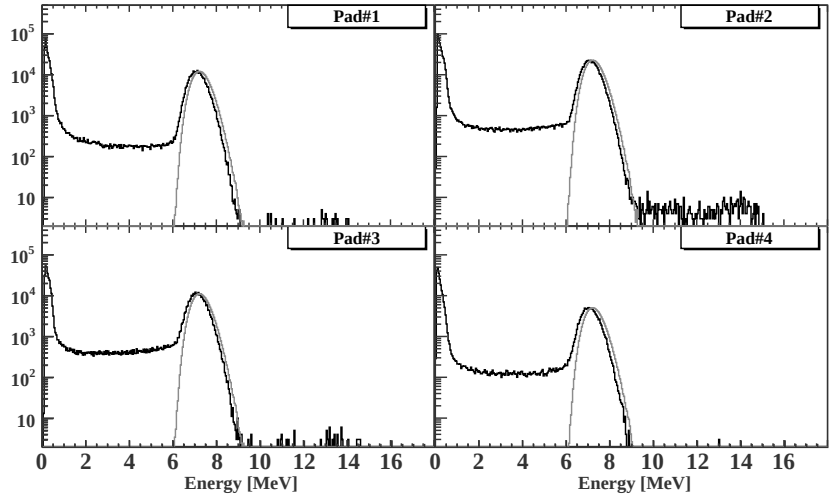

Figure 3.17: The experimental (black) and simulated (grey) spectra of Si(Li)#1; the initial energy of the beam in this simulation was 137 MeV, which shows a better agreement with experimental spectra.

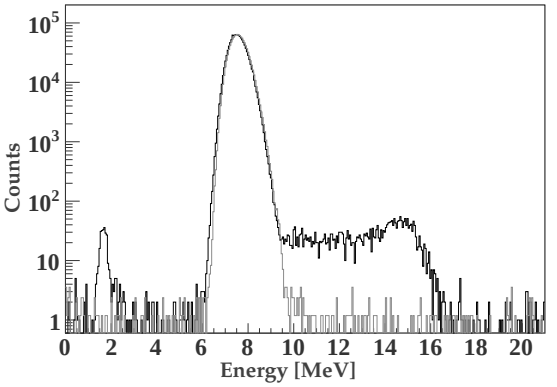

Figure 3.18: Same as Figure 3.17 but for Si(Li)#2. The events in the high-energy continuum (10 – 16 MeV) are correlated with the high-energy peak ($\sim$ 115 MeV) in the spectrum of the CsI scintillators (see Figure 3.10, the top-left panel), which shows they are due to the pileup of two proton hits.

Chapter

S393 Experiment

The experiment labelled S393[1] was carried out at the GSI facility in Darmstadt, Germany (see Figure 4.1). The beam of ions was produced in the ion source and then passed through the UNIversal Linear ACcelerator (UNILAC), which can accelerate ions up to 11.4 MeV per nucleon. Following acceleration in UNILAC, the beam was injected into the SIS18 (SchwerIonenSynchrotron) for acceleration to higher energies. SIS18 is a versatile synchrotron that is able to accelerate stable and radioactive ions up to energies of 1000 MeV per nucleon. In this experiment, a primary beam of ^{40}Ar ions was produced and accelerated to 500 MeV per nucleon. The argon beam was impinged on a primary target, and the fragmentation products were injected into the FRagment Separator (FRS) for selection of the ions of interest.

The Fragment Separator is an achromatic magnetic spectrometer which is used for production of the radioactive ion beams of interest. Secondary beams of radioactive ions can be produced via projectile fragmentation at a high rate, and then be separated efficiently, using in-flight technique [74, 75].

In this experiment, the secondary beams of oxygen isotopes were desired at energies above 400 MeV per nucleon. For this purpose, the primary beam of argon was impinged on a production target of beryllium with a thickness of around 4 g/cm^2 at the entrance of the FRS. Six different settings of the FRS produced six different cocktail beams covering different regions of the oxygen isotope chain, from ^{13}O to ^{24}O (see Table 4.1). The secondary beams produced by the FRS included a few other ions in the neighbourhood of oxygen isotopes, from Li to Ne. The extended range of ions in the beam made it possible to pursue several experimental goals in one experiment.

In the FRS beam line, there are two thin rectangular plastic scintillators, which produce the time information for particle identification and beam monitoring. Each detector is read out via two photomultipliers from left and right. The first one, called S2, is placed in the middle focal plane of the fragment separator (see Figure 4.2).

[1] A code, such as S393 for our experiment, is assigned to every experiment at GSI. S393 was used as a name to refer to this experiment, and so I have used it throughout this dissertation.

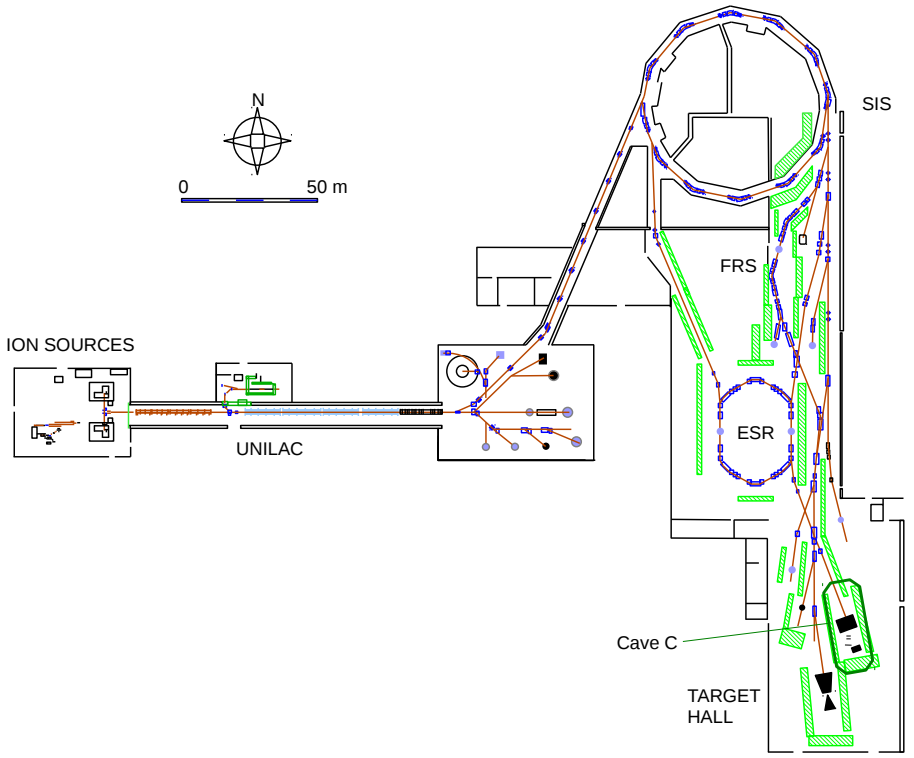

Figure 4.1: The schematic top view of the GSI experimental facility.

Table 4.1: Six FRS settings, delivering different sets of ions.

setting	ions of interest
1	neutron deficient ions; $^{13-15}$O
2	stable ions; $^{16-18}$O
3	moderately neutron rich ions; $^{18-20}$O
4	more neutron rich ions; ^{21,22}O
5	neutron drip line ions, focus on low charges; ^{8,9}Li, ^{14,15}B
6	neutron drip line ions, focus on high charges; ^{23,24}O

Unfortunately, malfunctions of this detector worsened the quality of its data; occasionally, the signal from one of the photomultipliers is absent, and eventually, the data of this detector were not used in further analysis. The second scintillator, called S8, is placed at the end of the FRS beam line. Figure 4.2 shows a schematic view of the FRS with connections to the SIS18, the Experimental Storage Ring (ESR) and the caves in the target hall.

After production and separation, the beam was injected into cave C (see Figure 4.1)

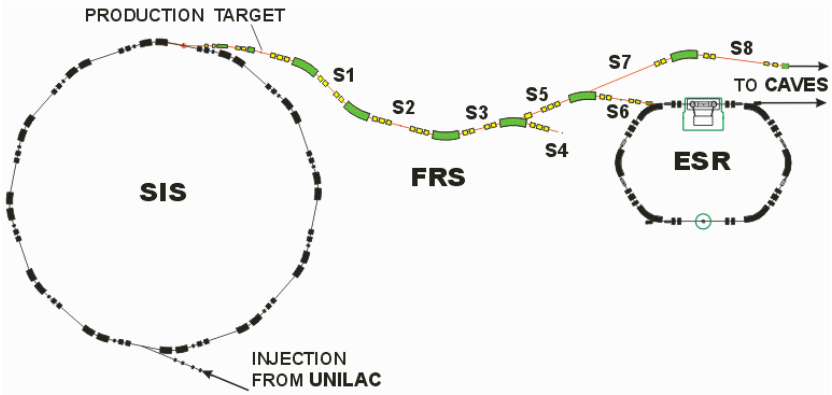

Figure 4.2: The schematic view of the FRS (coloured part) including beam monitoring detectors, S1 to S8.

in the target hall to impinge on the reaction target. Figure 4.3 shows a schematic view of the detection setup in cave C. The beam from the FRS passes through three beam diagnostic systems; a POsition Sensitive scintillator (POS), an active slit called ROLU (Rechts, Oben, Links, and Unten), and a Position-Sensitive Pin-diode (PSP). Then, the beam enters the reaction chamber surrounded by a spherical array of NaI scintillators, called Crystal Ball, to impinge on the target. The Crystal Ball detector provides a nearly 4π detection coverage for the gamma-rays emerging from the target. The photomultipliers in the forward hemisphere of the Crystal Ball detector have an extra read-out channel tuned for the detection of high-energy protons.

The interaction of the beam of radioactive ions with the target generates many reaction products, among which the products of the quasi-free scattering contain key information about the spectroscopic factors. Observation of the quasi-free reaction products requires a so-called kinematically-complete setup. This means that one has to measure the kinematical variables of the emerging protons and neutrons as well as the residual ions and fragments. For this reason, A LArge DIpole magNet (ALADIN) is placed right after the Crystal Ball detector, through which all the beam ions and reaction products exit the reaction chamber. The dipole magnet deflects the charged particles in different directions, while neutrons proceed directly to the Large Area Neutron Detector (LAND). Accordingly, the detection setup after the dipole magnet is divided into three branches; the neutron branch, the fragment branch and the proton branch. In Figure 4.3, the lowest branch after the dipole magnet is the proton branch, which includes two drift chambers (PDC) and an array of scintillators as a time-of-flight wall (DTF) at the end of the branch. The middle branch is the fragment branch including two scintillating-fibre detectors (GFI) and a time-of-flight wall (TFW) at the end of the branch. The neutron branch is the horizontal branch containing only the neutron detector (LAND), with a charged-particle veto detector in front of it.

This chapter explains the flow of signals from their creation in the detection system in cave C to the calibrated spectra used for the physics analysis. The first section is

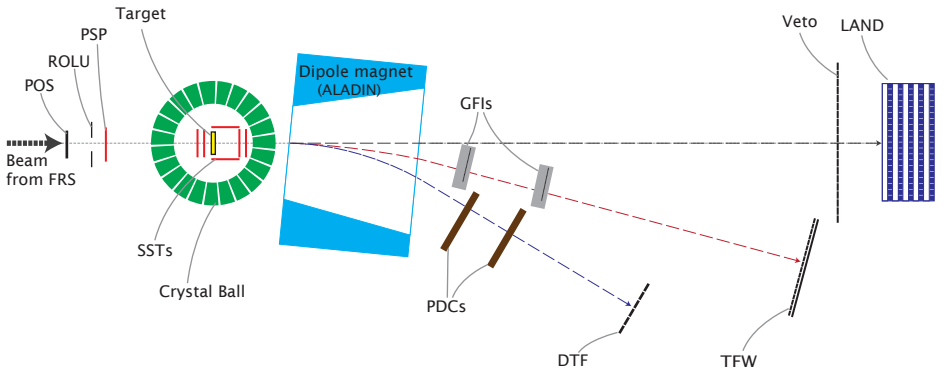

Figure 4.3: The schematic view of the detection setup in cave C.

dedicated to the general ideas of the calibration and reconstruction processes. The detection elements of the setup are described in three sections: before target (4.2), target chamber and surrounding (4.3), and after target (4.4). The calibration of each element is explained along with the description of the setup. Since the focus of the KVI group in the calibration phase was on the proton branch, the calibration of the drift chambers is described in more detail in subsection 4.4.4. Afterwards, the trigger scheme of the experiment is presented briefly in Section 4.5, and then, identification of the fragment masses is explained in Section 4.6. Section 4.7 describes the evolution of the present setup to the future R^{3}B experiment.

4.1 General ideas of calibration

The calibration of the LAND-R^{3}B setup is organised in several steps. Six well-defined steps are implemented in an analysis toolkit called `Land02`, originally developed by Håkan T. Johansson as a calibration and analysis tool for the LAND-R^{3}B setup [76]. These steps are defined as follows:

RAW: In the RAW level, the output data from the data-acquisition system are transferred to a `ROOT`[2] file without any operation on the data. In this level, the data of each read-out channel are structured as a `ROOT` tree, and stored in a `ROOT` file.

TCAL: The calibration at the TCAL level transforms the time signals from channel numbers to units of nanosecond. The energy signals undergo a pedestal subtraction which puts the zero of energy on the origin of the scale. For the time calibration at the TCAL level, the `tcal` programme of `Land02` was used. `tcal` uses the data of a time calibrator module, which are recorded during the experiment along with their specific trigger, and produces a set of time calibration coefficients that can be copied to the calibration files of `Land02`. The time calibrator data make it possible to monitor the possible gain fluctuations of the time-to-digital converters (TDC). For

[2] A data-analysis framework, `http://root.cern.ch/drupal/`.

determination of the pedestals, the `clock` programme was used. This programme reads the energy signals of each charge-to-digital converter (QDC), when the beam spill trigger and all detector triggers are absent, and only the pedestal values are stored in the data. Again, here, the gain fluctuations of the QDC modules can be monitored during the experiment.

SYNC: As is implied by the name, at this level, the calibrated time data from different channels are synchronised. Most of the detectors in this setup have several read-out channels, and in order to be able to compare the time information from different channels, all the channels have to be synchronised. In addition, a gain-matching factor is applied to the energy data from the TCAL level. For this calibration, different detectors are treated differently, as is explained in the next sections of this chapter. The `phase1`, and `phase1_gfi` programmes were used for the calculation of the synchronisation and gain-matching factors of scintillation detectors.

DHIT: At this level, the hits (particle interacting with the detector, resulting in a signal) are reconstructed in the frame of the detector, using the data which are time and energy calibrated. Reconstruction of each hit in a detector needs one or more valid signals from the detector. For most of the detectors, there are some validity tests, which filter events caused by noise. Moreover, some errors are calculated and stored along with the detector data.

HIT: The detector-specific data of the DHIT level are used to reconstruct kinematical variables, such as position and angle. In addition, the origin of position measurement is changed in this level, usually to the centre of the active area of the detector.

TRACK: In this level the positions from the HIT level are used to reconstruct the tracks of particles. In addition, the atomic numbers of incoming ions and their mass-to-charge ratios are extracted, which can be used for incoming particle identification. The reconstructed tracks and kinematical variables shall be used for further analysis to obtain the physics results such as cross sections and momentum distributions.

4.2 Detection system before target; Beam diagnostic

The first detector in the beam line of cave C is the POsition-Sensitive scintillator (POS), which provides time and position information. This thin scintillator (0.5 mm) is read out using four photomultipliers from four sides. When an ion passes through the scintillator, four signals are detected using the four photomultipliers. Using these signals, the position of the hit can be calculated. In this experiment, however, POS was used only for triggering and time information. The master trigger of the setup is defined when at least two of the POS photomultipliers fire within a defined time window.

The second detector in the beam line is ROLU, which determines the transverse spread of the beam. ROLU stands for Rechts (right), Oben (top), Links (left), Unten (bottom), and indicates the position of the four scintillators that form a rectangular aperture for the beam. These thin scintillators are remotely movable and allow

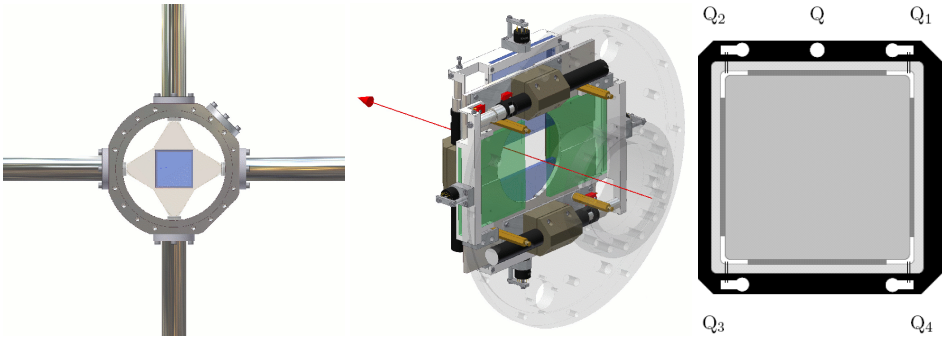

Figure 4.4: The drawings of POS with the four photomultiplier tubes (left), the active slit with its moving system, ROLU (middle), and the pin-diode, PSP (right).

the user to adjust the size of the aperture. If the trajectory of an ion occurs out of this aperture, one of the scintillators gives a signal that is considered as an anti-coincidence trigger to veto the event.

The next detector is the Position-Sensitive Pin-diode (PSP), which is the last in-beam detector before the beam enters the scattering chamber. This detector is an n-type silicon diode, with dimensions $45\times45\times0.3$ mm^3. When an ion passes through the diode, the released electrons are read out from four corners on the anode side (front). Using these four signals, one can calculate the position of the hit on the detector. The total charge is read out from one junction on the cathode side (back). PSP has an energy resolution of approximately 1% and a nominal position resolution of 0.2 mm.

Figure 4.4 shows the drawings of the three beam-diagnostic detectors. The information obtained from POS and PSP combined with the parameters of the Fragment Separator were used for identifying incident ions. The atomic number of each ion is calculated directly from its energy deposit in PSP[3], and the mass-to-charge ratio is reconstructed from the magnetic rigidity of the ion,

$$B\rho \propto \frac{A}{Z}\frac{v}{c}\gamma, \tag{4.1}$$

in which Z is the atomic number, and v, c, and $\gamma = 1/\sqrt{1-v^2/c^2}$ are the ion velocity, the speed of light, and the relativistic Lorentz factor, respectively. The magnetic rigidity of each ion is determined by the last dipole magnet of the Fragment Separator, and the velocity is calculated from the time of flight of the ion between S8 and POS. Figure 4.5 shows an example of the incoming particle identification for setting 3 of the Fragment Separator, which was optimised for ^{19}O and ^{20}O (see Table 4.1).

[3]The energy deposit of an ion in a material has a relation with its atomic number (Bethe-Bloch formula); therefore, atomic numbers can be identified using the energy-deposit signals of the detectors.

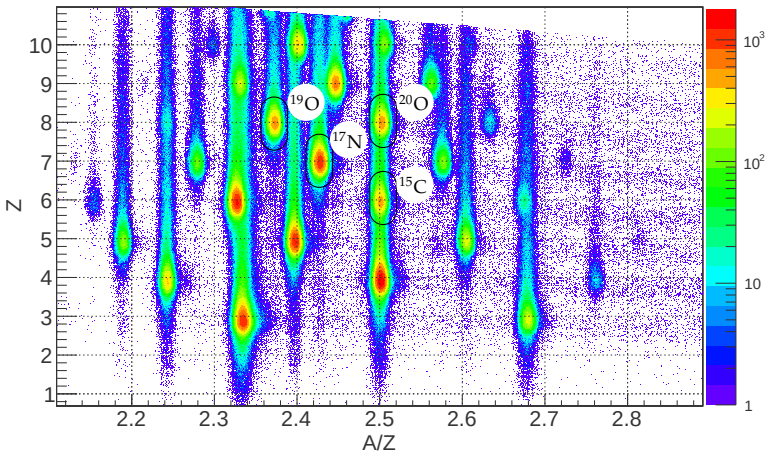

Figure 4.5: An example of the incoming particle identification, using data of FRS, POS, and PSP. Some of the ions are indicated by ellipses. The incoming-ion gate in the analysis is smaller than the indicated ellipse (see Subsection 5.1.1).

Table 4.2: The reaction targets used in the experiment. CH_2 material was used as proton target, carbon was used in order to subtract the carbon contribution to the reactions when CH_2 target is used. Lead is used for the Coulomb dissociation reactions, because it has a large atomic number.

Target material	Thickness [mm]	Thickness [mg/cm^2]
CH_2	5	458
CH_2	9.8	922
carbon	3	558
carbon	5	935
lead	1.5	2145

4.3 Scattering chamber and Crystal Ball

After the beam passes through the above-mentioned beam-diagnostic detectors, it enters a spherical scattering chamber. The scattering chamber has a diameter of around 50 cm, and is made of Aluminium with a thickness of 2.5 mm. The chamber holds a target wheel and eight silicon strip detectors. The target wheel has seven frames holding five reaction targets, a titanium target for background measurements, and one frame is left empty for calibration purposes. The reaction targets are listed in Table 4.2 along with their thicknesses. In addition to the experimental runs with these targets, a few hours of beam time in each setting was spent on the background runs, in which an empty target frame was placed in the beam line.

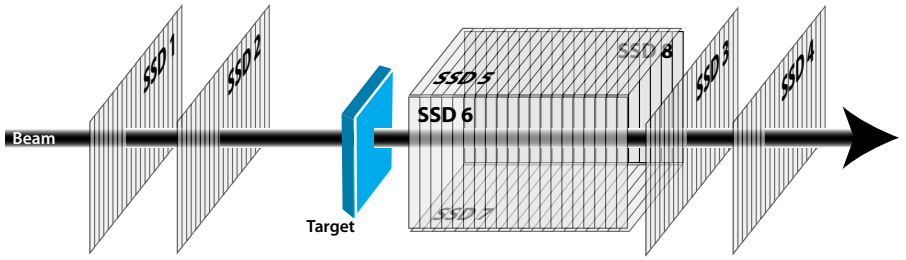

Figure 4.6: The schematic geometry of the eight silicon strip detectors with respect to the target. The arrow shows the beam direction.

4.3.1 Silicon strip detectors

The reaction target is surrounded by eight Silicon Strip Detectors (SSDs). Four of the strip detectors are placed in the beam line, perpendicular to the beam direction; two before the target, and two after. The other four strip detectors are put together in such a way that they form the four sides of a rectangular cube, parallel to the beam line. The latter four SSDs, sometimes referred to as box silicon detectors, are placed right after the target frame (see Figure 4.6).

Each silicon strip detector has a thickness of 0.3 mm and a surface area of 72×40 mm^2. Strip pitches of 27.5 μm are implanted on the junction side (p-side), of which every fourth strip is connected to a read-out channel, and the rest are left free. Thus, the read-out pitch on the p-side is 110 μm. On the ohmic side (n-side), the implantation pitch is 104 μm, with every strip read out. This yields 640 strips on the p-side and 384 strips on the n-side, that is a total of 1024 read-out channels for each silicon strip detector. The p-side strips are vertical and the n-side strips horizontal, forming a grid for two-dimensional positions measurements. The design of the silicon strip detectors of the LAND-R^{3}B setup is based on the silicon trackers of the Alpha Magnetic Spectrometer (AMS-02) experiment [77]. More information on the structure and properties of the strip detectors can be found in Reference [78].

The purpose of the silicon strip detectors was to measure the trajectory and energy loss of the particles impinging on and emerging from the target. Not only their position resolution is good, but also the energy loss of the reaction products from proton to oxygen can be measured using these detectors. In this experiment, the malfunctioning of two of the box detectors diminished their role. Specifically, SSD#5 and SSD#6 were not functional except for few strips. At least two position measurements with the azimuthal-angle difference of $\Delta\phi \sim 180^\circ$ are required in order to detect the emerged nucleons from a quasi-free reaction. However, the functional SSDs (SSD#7 and SSD#8) are places side by side, and not opposite to each other. Therefore, the box detectors were not used for the reconstruction of the scattering angles of the outgoing protons.

Calibration

Since no time information was read out from the SSDs, we only deal with the energy and position calibration. The pedestals are measured using the `clock` programme (see Section 4.1). For each ion passing through a silicon detector, several strips fire with different intensities, because of the capacitive coupling of the strips. The fired strips form a cluster with a charge distribution similar to a Gaussian distribution. The position of a hit is determined as the charged-weighted mean (here called the centre of gravity) of the cluster charge distribution, and the energy deposit of the ion is proportional to the integral of the charge distribution. The position information of the SSDs is influenced by a few effects, as described in the following. By correcting these effects, it is possible to get a position resolution better than the strip pitch.

Each 64 strips are connected to one read-out electronic board, equipped with a VA64-HDR9A preamplifier-shaper circuit from IDEAS, Norway. The VA64 circuits can have different gains, and their gains should be matched. However, before the gain-matching of the VA64 chips all other effects should be corrected, namely charge sharing between strips, and faulty or broken strips. The faulty strips are the ones whose signal is considerably different from the other strips, due to a different capacitance with the neighbouring strips or a loose bounding to the read-out circuit. The broken strips are the ones that do not produce any signal. In general, nothing much can be done for these strips, except estimating their signal strength using that of the two neighbouring strips. This only works if a broken or dead strip is in between two working strips.

In addition to the above-mentioned corrections for the silicon strip detectors, the charge sharing between the strips should be corrected. Although each strip is electrically isolated from the neighbouring strips, diffusion of electric charge within the bulk of the silicon detectors can result in the charge-sharing effects. When an ion impinges on a silicon strip detector, the total charge (and hence the output signal) depends on the position at which the ion hits the strip. This effect is minimum if the ion passes through the detector perpendicular to and in the middle of a strip; on the contrary, if the ion passes through in between two strips or travels through the detector with an angle, this effect will be large. In order to quantify this effect we define the *inter-strip parameter*, η, as the fractional part of the centre of gravity. Therefore, an inter-strip parameter of zero means a hit in the centre of the strip, and an inter-strip parameter of 0.5 means a hit exactly in the middle of two strips.

The energy signals of each strip show a dependence on the inter-strip effect, which deteriorates both position and energy resolutions. Therefore, this effect should be corrected for both energy signals and reconstructed positions. For this purpose, the energy deposit signals of a SSD are drawn versus its inter-strip parameter, η, under the selection of a specific atomic number. The left panel in Figure 4.7 shows such a plot, which illustrates the inter-strip effect as a nearly Gaussian shape. Then we corrected for this effect using the energy shifts obtained by the fit of a Gaussian distribution. The right panel in Figure 4.7 shows the corrected energy deposits versus η. The reconstructed positions of each SSD is also corrected using the evaluated inter-strip parameter.

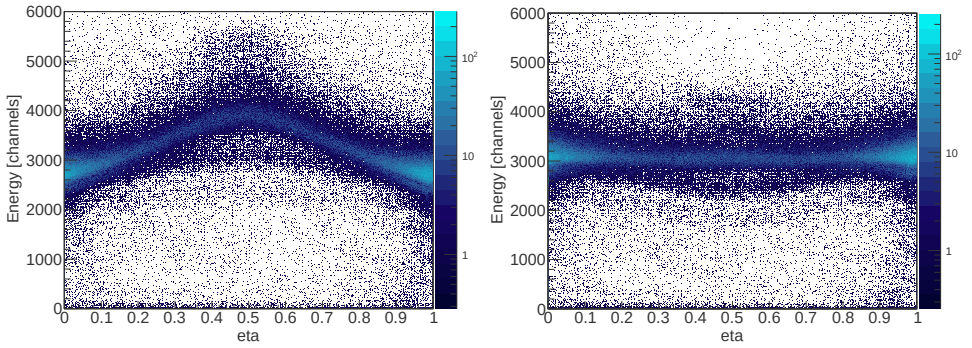

Figure 4.7: The gain correction of the charge-sharing effect. Here the energy deposit of oxygen ions in SSD#3 has been drawn versus inter-strip parameter, η; left: before correction, right: after correction. A condition on the outgoing charge is required using the TFW energies.

More information about the correction procedure can be found in the theses of F. Wamers [79], J. Taylor [20], and C. Langer [80]; who discuss the procedure in more detail. Figure 4.8 illustrates the correction of charge-sharing effect for the reconstructed position; upper and lower panels for before and after the correction, respectively.

4.3.2 Crystal Ball detector

The emitted photons from reactions in the target were detected in a spherical array of scintillators surrounding the scattering chamber. This array of scintillators, called Crystal Ball, is composed of 162 NaI scintillators and covers an almost 4π solid angle around the scattering chamber, in such a way that each one of the scintillators has a nearly equal solid-angular coverage of 77.6 msr. In order to achieve this coverage, four different shapes of the NaI crystals are used. This sphere of scintillators has an inner radius of around 25 cm and a thickness of 20 cm. Each crystal is wrapped in a metal case with a thickness of around 0.5 mm. More details on the properties of the Crystal Ball detector are given in Reference [81].

In addition to Coulomb excitations, the quasi-free reactions are studied using this setup. Therefore, in addition to gamma rays, the knocked-out nucleons of quasi-free reactions should be detected. For this reason, each photomultiplier tube in the forward angles has another read-out channel in addition to the photon read-out, which is optimised to measure the energy of protons. The proton channel is, in fact, a read-out from dynode number 8 of each photomultiplier, which is the dynode before the final stage of electron multiplication. The photon channel is read out from the last dynode (the pick-up anode). The raw signal from each read-out channel of each photomultiplier tube is split to two channels, in order to obtain time and energy information of each signal. Based on simulations, for protons with kinetic energies around 280 MeV or higher there is a probability of punching through the Crystal Ball detector, while the kinetic energies expected from the quasi-free reac-

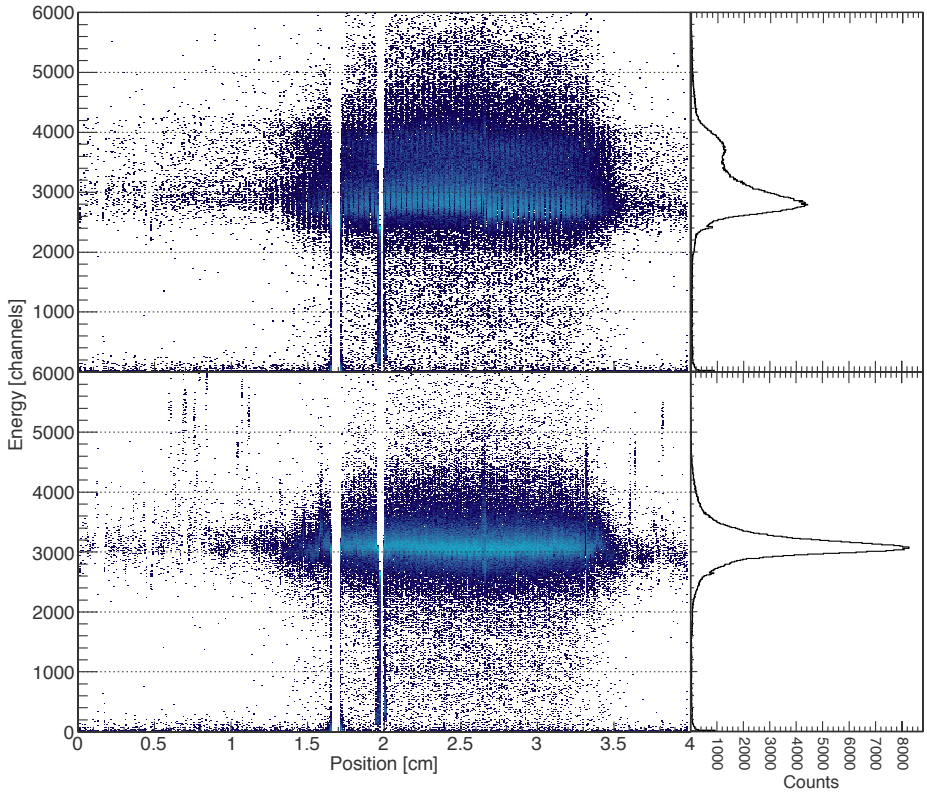

Figure 4.8: The position correction of the charge-sharing effect. Here, the energy deposit of oxygen ions in SSD#3 has been drawn versus the reconstructed position; top: before correction, bottom: after correction. A condition on the outgoing charged particle is required using the TFW energies.

tions in S393 are from a few tens to a few hundred MeVs. Therefore, it is not possible to measure the total energy of the high-energy protons. Nevertheless, the necessary information from the knocked-out protons are multiplicity and the scattering angle.

Calibration

The energy calibration of the photon and the proton read-out channels are mainly based on the use of radioactive calibration sources and cosmic muons, respectively. In S393, three gamma-ray sources were used for the Crystal Ball calibration: ^{22}Na, ^{88}Y, and ^{60}Co. Figure 4.9 illustrates a typical fit of a ^{22}Na spectrum for calibration of the gamma spectrum of a crystal. Such a fit was performed for each crystal, using both ^{22}Na and ^{60}Co sources. The peak positions obtained from these fits are used to calibrate the energy spectra of the Crystal Ball detector. Figure 4.10 demonstrates the quality of the calibration. This plot shows the energy spectrum of photons in a background run, without beam. The 511-keV peak of the pair production events

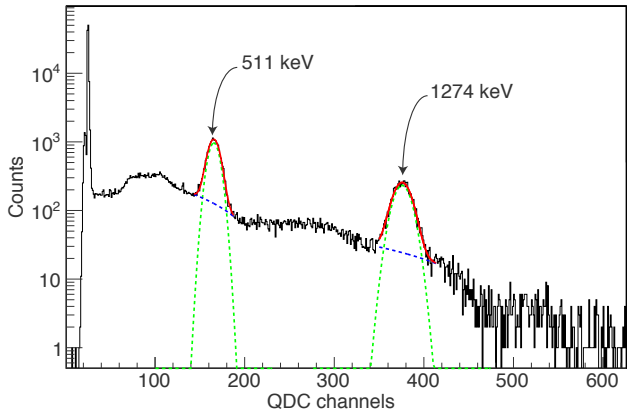

Figure 4.9: The raw gamma spectrum of ^{22}Na in the Crystal Ball detector. Peak positions are obtained using a Gaussian fit (red curve) on top of a linear background (dashed blue line). This histogram is from crystal number 13.

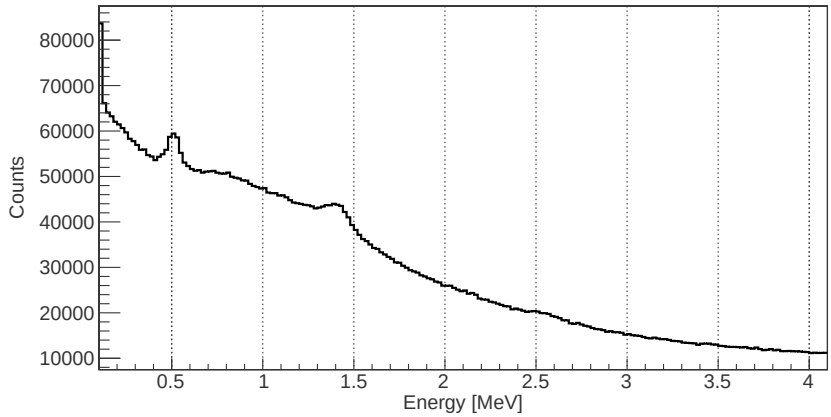

Figure 4.10: The photon spectrum of the Crystal Ball detector in a background run. The peaks at 0.511 and 1.46 MeV are caused by the pair production events and decay of ^{40}K, respectively.

and 1.46-MeV peak from the decay of ^{40}K are obvious, and the weak bump at energies around 2.5 MeV could be a signature of the ^{232}Th background.

After calibration of the photon read-out, the proton read-out can be calibrated by applying a correction factor to the calibration of the photon read-out. However, the proton energies obtained using this calibration bear large fluctuations from crystal to crystal. The proton energies measured with the crystals are much larger than the photon energies of the radioactive sources used for the calibrations. Small fluctuations in the radioactive-source calibration scale up when that calibration is extrapolated for the proton read-out. Therefore, the calibration of the proton read-out channels are performed using cosmic muons.

Since cosmic muons have nearly random paths, and hence nearly random energy deposits in the Crystal Ball detector, it is necessary to choose specific muons which have a definite energy deposit in the Crystal Ball detector. Therefore, only two sets of cosmic events are selected; the *opposite-passing* cosmic muons which travel through two opposite crystals with respect to the centre of the Crystal Ball detector, and the *grazing* ones which pass through several crystals but do not enter the scattering chamber. The criteria for the selection of the cosmic-muon events assert that each one of these two muon sets (opposite-passing and grazing) have a rather well-defined path in the Crystal Ball detector, and therefore, their energy deposit can be used for the final calibration of the proton energy channel. A detailed overview of the Crystal Ball detector calibration can be found in Reference [82], including the algorithms used for the selection of the two sets of muon events. Figure 4.11 illustrates the calibration using the cosmic muons. The left and right panels show the energy deposit of the opposite-passing cosmic muons in the Crystal Ball detector versus the crystal number, before and after the calibration, respectively.

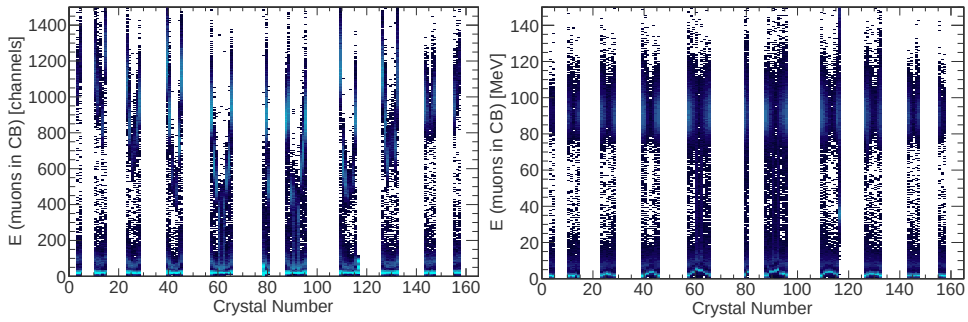

Figure 4.11: Energy deposit of the opposite-passing cosmic muons in Crystal Ball versus the crystal number; left: before the calibration, right: after the calibration. The crystal numbers with no counts are the crystals that do not have proton read-out.

After the energy calibration, a so-called add-back algorithm is employed to cluster the energy signals of the crystals. The algorithm sorts the energy signals of each read-out channel (photon and proton) in a list. The top energy in each list is considered to be the central crystal of a cluster in that list. If the second crystal in the list is an immediate neighbour of the first one, its energy is added to the first cluster, otherwise it is considered to be the central crystal of the second cluster. Similarly, for each crystal in the list: if it is a neighbour of a central crystal of an established cluster, its energy is added back to that cluster, otherwise it forms a new cluster. This procedure is performed for both photon and proton read-out channels. For a detailed description of the clustering procedure see Reference [83].

For the time calibration, first the channel numbers of the TDC are multiplied by the TDC gain, 0.025 ns in S393, and then they are synchronised using a straightforward procedure as follows. The data of the gamma-ray sources ^{22}Na and ^{60}Co are used, in which two photons are detected in coincidence. After suppression of random coincidences, the time difference of the detected decay photons is saved in a histogram for each pair of crystals. Then, using a simple fit, the mean value of each

histogram is obtained as the time difference between the two crystals. The set of time differences for all crystal pairs is used to synchronise the crystals.

Reference [82] gives an extended account of efficiency calculations for the Crystal Ball detector. Three different methods have been employed, among which the most trustworthy one gives efficiencies of 36.44 ± 0.77 % and 34.65 ± 0.65 % for detecting the photo-peaks of the ^{60}Co gamma-rays at 1173 keV and 1332 keV, respectively.

Doppler-shift correction

The decay photons are emitted from the reaction residues, which are travelling at high velocities. Therefore, the photon frequencies, and hence, energies are shifted to different values based on the angle of detection (the Doppler shift). Since the ions are moving at relativistic velocities, the Doppler shift is significant and must be corrected, in order to obtain the photon energies in the rest frame of the ions. This correction has been performed using the following equation:

$$E_{rest} = \gamma E_{LAB}[1 - \beta \cos(\theta_{LAB})]. \tag{4.2}$$

Here, E_{LAB} is the detected energy of photons by the Crystal Ball detector after clustering, $\gamma = \sqrt{1-\beta^2}$ and $\beta = v/c$ are the Lorentz factor and the ion velocity, respectively.

4.4 Detection of the reaction products and fragments

As already mentioned, the detection system after the magnet is divided in three branches, containing five different detection elements in total. These elements are briefly explained in the following subsections; first LAND in the neutron branch, and then the two scintillating fibre detectors (GFI) and TFW in the fragment branch, and at the end the two drift chambers (PDC) and DTF of the proton branch are explained.

4.4.1 Large-Area Neutron Detector (LAND)

The Large-Area Neutron Detector is used for the measurement of the energy, the time of flight, and the position of the knocked-out neutrons from reactions. It has a total size of $2\times2\times1$ m^3, and is made of 10 layers of detection paddles. Each layer is composed of 20 paddles, each paddle being a sandwich structure of alternating iron sheets (11) and organic scintillators (10). The two outer iron sheets in each paddle are 2.5 mm thick, while the other iron sheets are 5 mm thick. The thickness of each scintillator is 5 mm, thus giving rise to a 100-mm-thick paddle. Figure 4.12 shows a schematic drawing of the iron and scintillator sheets, and their connection to the photomultipliers.

The iron sheets are used as passive converter materials. When a neutron enters LAND, it interacts with the iron sheets and ignites a shower of charged particles

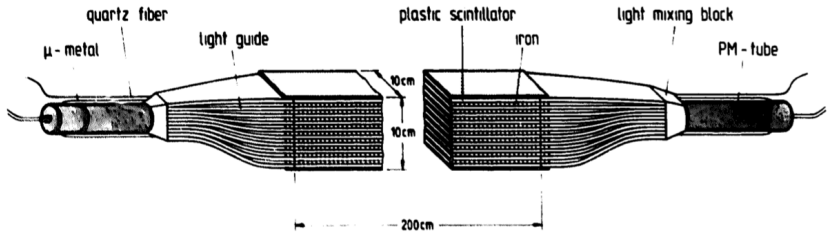

Figure 4.12: The arrangement of the iron and scintillator sheets in a LAND detection paddle, adapted from [84].

that can be detected in the scintillators. The scintillation light from each scintillator sheet in each paddle is guided to two photomultiplier tubes at both ends, and these two photomultipliers are shared between all scintillators of that paddle. Using the time difference between these two photomultiplier tubes, the position of the hit in the paddle can be reconstructed. The energy resolution of LAND is 5.3% for neutrons of 1 GeV energy, and its efficiency is larger than 90% for neutrons with energies larger than 550 MeV. With a good synchronisation and gain-matching, a time resolution of 250 ps is achievable as well as an intrinsic position resolution of around 5 cm [84].

In order to remove the background of charged particles, an array of 20 vertical scintillating paddles, called veto wall, is placed in front of the LAND detector. Each paddle has dimensions of $200\times10\times0.5$ cm^3 and together they cover the front face of LAND. Any signal from the veto wall is used to veto the read-out of charged particles in the LAND detector.

Calibration

The energy calibration and synchronisation of LAND is based on cosmic muons, and the time offset is adjusted using the high-energy photons that are emitted from the reaction target at forward angles. The position information is reconstructed based on the same method as the one for TFW, and it will be explained in subsection 4.4.3. For more details on the calibration of LAND, see Reference [85].

4.4.2 Large-area scintillating fibre detector (GFI)

The large-area scintillating fibre detectors provide horizontal position information of ions after the dipole magnet. Each GFI detector is composed of 475 vertical scintillating fibres, each fibre being 1 mm wide and 500 mm high, giving rise to an active area of 475×500 mm^2 for each one. The fibres are placed side by side, and are optically isolated from each other. The measurement of the position relies on the determination of the fibre that is hit. For this reason, the scintillation light emerging from the top of each fibre is conducted through a separate light guide to a pixel mask, which is connected to a position-sensitive photomultiplier tube. The position-

sensitive photomultiplier tube includes a grid of 18×16 anode wires placed right after the photo-cathode. The charge distribution on the anode grid is correlated with the light spot on the photo-cathode, making it possible to identify the fibre that is hit. With a successful determination of the fired fibre, a position resolution of 1 mm is assured. The other end of each fibre is connected to a conventional photomultiplier tube, which sums the energy deposited in all fibres and also provides time information [86].

In this experiment, two GFI detectors were used for tracking the ions in the fragment branch. Different ions with different charge-to-mass ratios are deflected to different angles in the dipole magnet. Two position measurements after the magnet combined with the information of the silicon strip detectors allow us to determine the deflection angle of the ions. The deflection angle is used in the tracking procedure which gives the momentum of the beam-like ions.

Calibration

The calibration of the scintillating fibre detectors is based on the so-called *sweep runs*, in which the electric current of the dipole magnet increases from zero to maximum and returns to zero smoothly. In a sweep run all the fibres are irradiated rather uniformly, and therefore, all pixels of the mask are illuminated. After pedestal subtraction using the `clock` programme (see Section 4.1), the `phase1_gfi` programme is used to match the gains of the anode wires.

Each hit in a fibre lights up a spot on the photocathode, which is generally large enough to create electric signals in a few anode wires in both directions of the grid, (u, v). The charge distribution of the grid in each direction resembles a Gaussian shape. The `phase1_gfi` programme employs an algorithm that fits Gaussian distributions to the charge distributions of the anode grid in u and v directions. Then the differences of charge of each wire from that determined from the Gaussian distribution are used to match the gains of all wires. The gain-matching procedure is explained in more details in [87] and [88].

4.4.3 Time-of-flight wall (TFW)

The Time-of-Flight Wall is the last detector of the fragment branch, located downstream of the GFIs, for the measurements of the time-of-flight, the energy deposit, and the position of the fragments. TFW is composed of 18 horizontal and 14 vertical scintillator paddles placed side-by-side, the vertical ones being behind the horizontal ones. The horizontal paddles are longer than the vertical ones, and both are 100 mm wide and 5 mm thick, creating an active area of 189×149 cm^2. Each paddle is read out from both ends via photomultiplier tubes, which makes it possible to reconstruct the position of hit. However, the position of ions are measured with a higher precision using the GFIs, and therefore, the position sensitivity of the TFW paddles has little importance, while their time resolution is crucial in the data analysis. See Section 5.2.6 about the position resolution of TFW.

Calibration

In this subsection, the general calibration of a scintillator paddle is described. This procedure is used for the calibration of the TFW, LAND, and partially for the DTF. The output signal of each photomultiplier of the scintillator paddles is divided to two signals, one for the time measurement using a TDC and the other one for energy measurement using a QDC. For the primary time calibration the `tcal` programme is used, which transfers the time data to units of nanosecond. For QDCs, however, the primary calibration includes pedestal subtraction and gain matching, in which, the pedestals are determined using the `clock` programme (see Section 4.1). In order to match the gains of the two photomultipliers of a paddle and synchronise their time, the following method is used.

Figure 4.13 shows a schematic view of a hit in a scintillator paddle. For a scintillator paddle of length L, the measured time and energy signals depend on the position of hit, x, as

$$\begin{aligned} t_1 &= \frac{x}{v_{\text{eff}}} + t, \\ t_2 &= \frac{L-x}{v_{\text{eff}}} + t, \end{aligned} \tag{4.3}$$

and

$$\begin{aligned} E_1 &= Ee^{-x/\lambda}, \\ E_2 &= Ee^{-(L-x)/\lambda}, \end{aligned} \tag{4.4}$$

respectively. v_{eff} is the effective velocity of light in the scintillator material, and λ is the attenuation coefficient of the scintillator material. t and E are the time and total energy deposit of the hit.

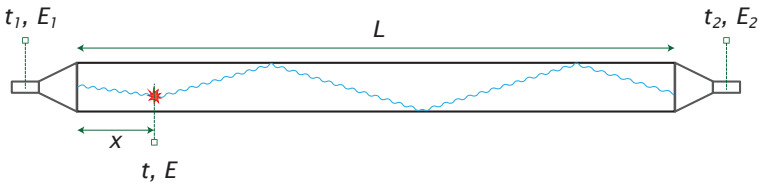

Figure 4.13: Schematic view of a hit in a scintillator paddle.

Using Equations 4.3 or 4.4, the position of hit can be calculated as

$$x = \frac{L}{2} + \frac{v_{\text{eff}}}{2}(t_1 - t_2) \tag{4.5}$$

or

$$x = \frac{L}{2} - \frac{\lambda}{2}\ln\frac{E_1}{E_2}, \tag{4.6}$$

respectively. The origin of the position measurement is finally shifted to the centre of the active area of TFW.

For each TDC signal, an offset is adjusted in a way that the hits in the centre of the paddle give a time difference of zero in the two photomultipliers, thus synchronise the photomultipliers. Moreover, QDC gains are matched using the same set of hits, which have energy signals of the same size in both photomultipliers. This is only possible for the detectors that have crossed paddles, in which we can use the central paddle in the horizontal array to locate the centre of the vertical paddles and vice versa.

After time synchronisation and gain matching of the photomultipliers of each paddle, the next step is to remove the time shifts and energy differences of different paddles with respect to each other. This step is achieved by using a large amount of beam-time data, in which every pair of crossing paddles are hit at least once. Taking into account all possible pairs gives rise to the synchronisation and matching of the paddles with respect to each other. The calibration of the paddles is discussed more extensively in the dissertations of D. Rossi [85] and S. Paschalis [88].

To complete the energy calibration, the channel numbers should be converted to the units of energy which depends on the response of the detector to the beams, and should be performed by the user. Similarly, the synchronisation of each detector with respect to the whole setup should be implemented by the user. For the calibrations of this dissertation a simple simulation in `Geant4` produced time and energy deposit data, for the beams of interest. The simulated time of flight and energy deposit were plugged in the calibration process of the `Land02` manually. The calibration of TFW including time synchronisation and gain matching of the paddles are illustrated in Figure 4.14. Each panel in Figure 4.14 shows the energy deposit of the reaction residual ions in TFW versus their reconstructed position, when the incoming ion is gate on ^{20}O; the left panel was produced after time conversion to nanosecond, but before synchronisation and energy calibration, and the right panel was produced after all the calibration steps.

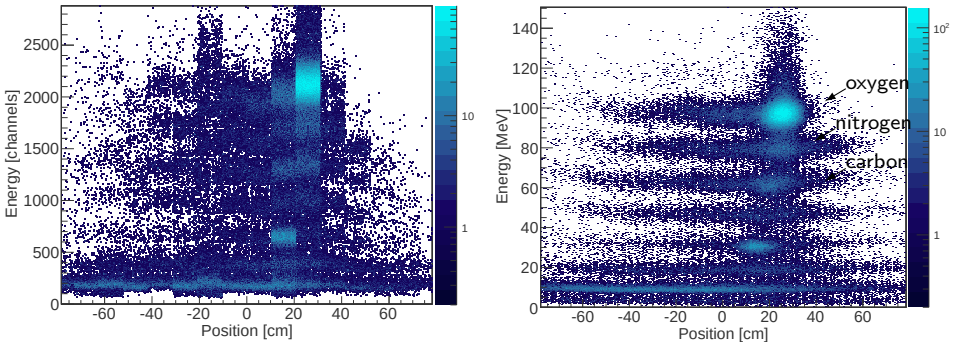

Figure 4.14: Energy deposit of outgoing ions in TFW versus their reconstructed position; left: after time calibration, but before synchronisation and energy calibration, right: after all calibration steps. Incoming ion is gated on oxygen.

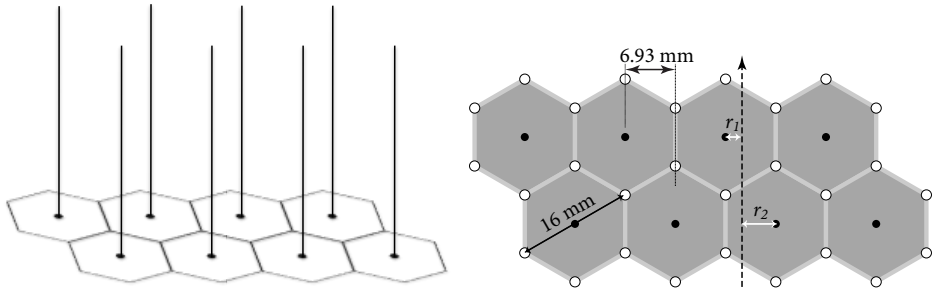

Figure 4.15: The schematic view of the PDC wires; left: a small portion of the wires of a PDC X layer, right: the top view of eight wires. The black dots and hollow circles show the sense and field wires, respectively. The dashed arrow indicates a proton trajectory. r_1 and r_2 are distances of the trajectory from the two nearest wires.

4.4.4 Proton drift chamber (PDC)

The Proton Drift Chambers, designed for tracking of protons, are located after the dipole magnet (see Figure 4.3). Each PDC is composed of two layers, one with 144 vertical wires (X layer) for the measurement of the horizontal coordinate of the traversing proton, and the other one with 112 horizontal wires (Y layer) for the measurement of the vertical coordinate. The chamber gas is a mixture of 80% Argon and 20% CO_2, and flows continuously during the operation time. The distance between wires is 6.93 mm in the perpendicular direction to the beam (see Figure 4.15), and the active area of each chamber is 100×80 cm^2, providing enough angular acceptance for the detection of protons after the dipole magnet. Figure 4.15 shows a schematic view of the construction of a PDC layer.

In order to optimise the acceptance, the drift chambers should be placed as close as possible to the dipole magnet; however, if the position is too close to the magnet the drift chamber might obstruct the path of the fragment branch. Therefore, the first drift chamber is placed at around 2.5 m away from the centre of the dipole magnet. The total size of each drift chamber including the frames is $120\times100\times15$ cm^3, with the entrance and exit foils as large as the active area. The entrance and exit foils are made from Mylar, metalled from the inner side to prevent charging of the foils.

Like every other wire chamber, the detection of a particle in the PDCs is based on the ionisation of the gas along the path of the particle. The drift of the electrons occurs due to an electric field produced between sense and field wires. The field wires are 75 μm in diameter, and form a set of hexagonal cells surrounding two rows of 25 μm-thick sense wires in the centres of the cells, as is illustrated in Figure 4.15.

In this experiment, two drift chambers were used in the proton branch. The angular distribution of the protons, after the dipole magnet, can be determined using the PDCs in the same manner as for the recoil ions using the GFIs. However, the PDCs provide a better position resolution than the GFIs (1 mm resolution). The measured position resolution of the PDCs in this experiment was obtained to be on average 0.35 mm (see Figure 4.18 and Table 4.3).

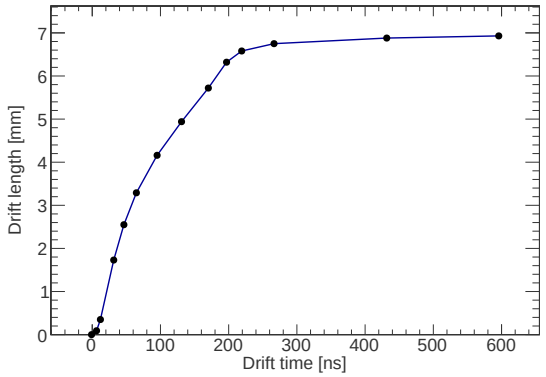

Figure 4.16: An example of the *rt*-curve after the optimisation iterations.

Reconstruction of proton trajectories

When a proton exits the dipole magnet, its trajectory is tracked using the drift chambers. Each drift chamber measures the position of the proton at one point along its trajectory, and each point is measured in two dimensions using vertical and horizontal wires. The vertical and horizontal wires are placed in two different layers of each drift chamber. The drift chambers provide the possibility to reconstruct the proton tracks at two levels. The first level is a simple reconstruction using the position of the wires, such as

$$\text{position of trajectory} = \left(\frac{x_i + x_{i+1}}{2}, \frac{y_i + y_{i+1}}{2} \right),$$

in which the indices i and $i+1$ correspond to the positions of the two wires straddling the proton trajectory for the x and y coordinates.

The second level, a more subtle reconstruction, is based on the determination of the distance of the proton trajectory from the two nearest wires. This distance is correlated to the drift time of the ionisation electrons, and this correlation is given by a look-up table, called *rt*-curve. A primary *rt*-curve is obtained from a simulation using `GARFIELD` (a simulation software for gas chambers [89]). An optimisation function embedded in `Land02` uses the primary *rt*-curve to produce a better one. A user can perform this optimisation iteratively until the desired resolution is obtained or the *rt*-curve does not change any more. Figure 4.16 shows an example of the *rt*-curve.

A function in `Land02` uses *rt*-curve and the drift time of the ionisation electrons to calculate the distances of a proton trajectory from the two nearest wires, r_1 and r_2 (see Figure 4.15). Having r_1 and r_2 for each coordinate, we can write

$$\text{position of trajectory} = \left(\frac{x_i + r_{x,i} + x_{i+1} - r_{x,i+1}}{2}, \frac{y_i + r_{y,i} + y_{i+1} - r_{y,i+1}}{2} \right).$$

Figure 4.17 shows typical plots of r_1 and r_2, which were plotted using the data ex-

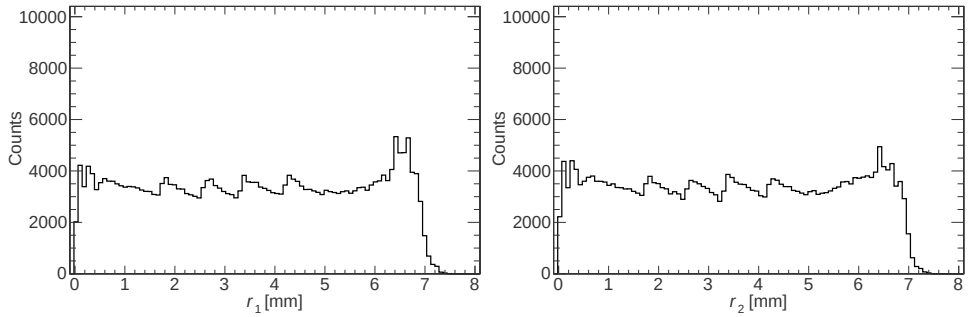

Figure 4.17: The reconstructed distance of a proton trajectory from the nearest wires; r_1 and r_2. The wavy shape of the histograms is an indication of the number of the used *rt*-curve points. If a large number of points is used, the wavy shape becomes smooth.

tracted at DHIT level[4]. As was intended, r_1 and r_2 have a uniform distribution. Indeed the uniform shape of the plots of r_1 and r_2 is the criterion that is used in the optimisation procedure of the *rt*-curve. This criterion is based on the assumption that the chances of a proton track at any point between two adjacent wires are equal. The wavy shape of the histograms is an indication of the number of the used *rt*-curve points. If a large number of points is used, the wavy shape becomes smooth, but it only adds to the computation time, and no improvement is gained on the resolution.

Ideally, the sum of r_1 and r_2 should equal the distance between two adjacent wires, that is to say the plot of $r_1 + r_2$ should peak around 6.93 mm. A typical case of such plot is shown in Figure 4.18 that peaks around 7.14 mm. The position resolution of each layer is measured by the width of this plot; $\frac{\sigma_{r_1+r_2}}{\sqrt{2}}$. Table 4.3 gives the resolutions of the two layers of the two drift chambers.

In Figure 4.19, the left and right panels show the correlation plots of the first drift chamber versus the second one in horizontal and vertical coordinates, respectively. In the left panel, two major bands can be seen; the main band which extends from almost the top right to the lower left corner, and a shorter band which extends from the lower left corner to the middle of the plot. Identifying the origin of the two bands turns out to be not trivial. Simply, one could think of using the time of flight of the particles creating the two bands. However, it seems that the events in the lower band are not in coincidence with the DTF. To be more specific, requiring a non-zero energy deposit in the DTF limits the geometrical acceptance of the drift chambers, which appears as rather sharp cuts in the correlation plot (see Figure 4.20). These sharp cuts indicate that the geometrical width of the DTF is not enough to cover the whole acceptance of the drift chambers.

Another way of investigating the two bands is using the time-over-threshold data of the drift chambers, which are related to the energy deposit of particles. Clearly

[4]The data of setting#2 (see Table 4.1) has been used for the calibration, analysis, and efficiency calculations of the drift chambers. For other settings, only a different time offset should be applied.

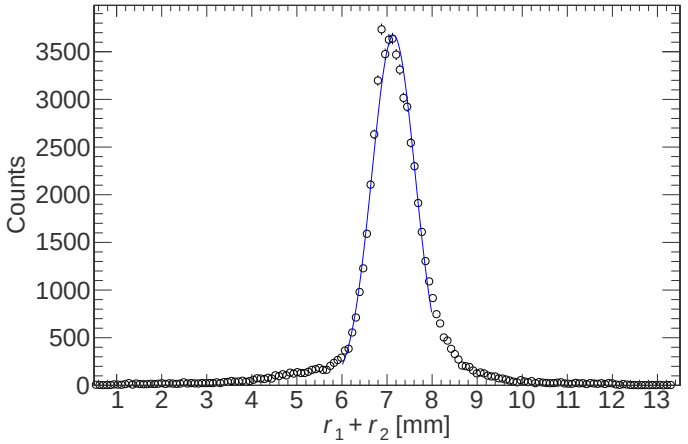

Figure 4.18: The sum of the distances of a proton trajectory from the two nearest wires. The mean value of the fit is 7.14 mm and the width is $\sigma = 0.48$ mm, resulting in a position resolution of $\frac{0.48}{\sqrt{2}} = 0.34$ mm. In order to select the hits perpendicular to the PDC layer, a hit on the DTF paddle #3 was required.

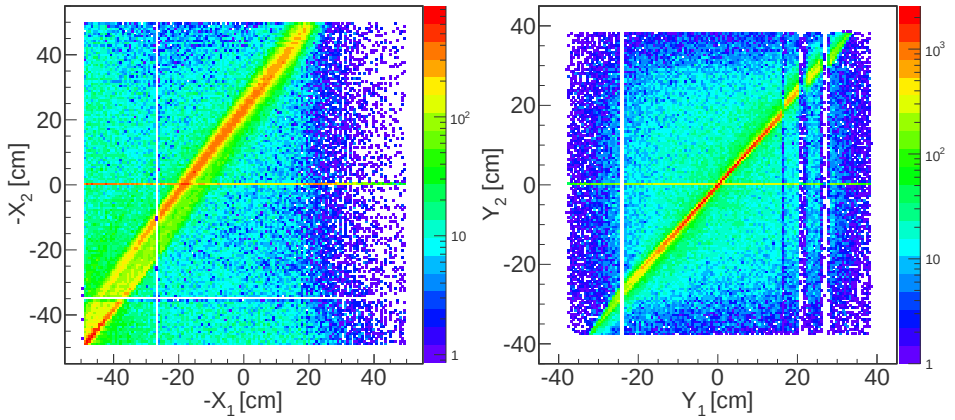

Figure 4.19: The reconstructed x (left) and y (right) coordinates of the first drift chamber versus the respective coordinates of the second drift chamber. The gaps are due to the broken or faulty wires.

the events in the lower band are from hits at smaller x values on the drift chambers, meaning that they are deflected at smaller angles through the dipole magnet. This would then imply that the particles in the lower band have larger magnetic rigidities than the ones of the main band. Possible cases are very light ions such as deuterons or ^{4}He ions, which have larger A/Z ratio as that of protons, and thus, deposit more energy in the drift chambers, which would appear as larger time-over-threshold values in data. This idea was tested by studying $\Delta x = x_2 - x_1$ of the drift chambers under different time-over-threshold conditions.

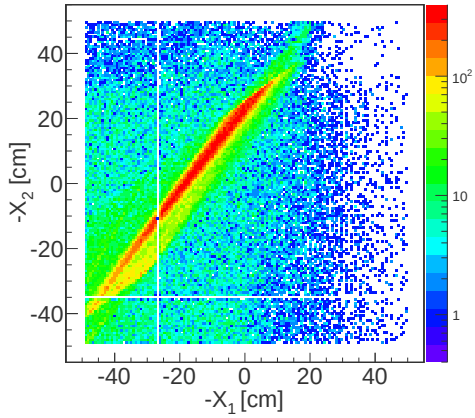

Figure 4.20: The horizontal-coordinate correlation of the drift chambers under the DTF trigger condition.

Table 4.3: The resolution ($\frac{\sigma_{r_1+r_2}}{\sqrt{2}}$) and efficiencies of the different layers of the drift chambers. The statistical uncertainties on resolution are small, on average 0.003 mm. The combined efficiency of the two drift chambers is 78.8(0.5)%.

PDC layer	Resolution [mm]	Efficiency [%]
X1	0.34	94.4 (0.3)
Y1	0.34	89.3 (0.4)
X2	0.36	96.2 (0.2)
Y2	0.35	97.2 (0.2)

Different time-over-threshold intervals from both drift chambers are selected and the corresponding Δx values are drawn, as shown in Figure 4.21. We expect that the intervals with larger time-over-threshold enhance the number of events with smaller Δx. These intervals are selected from a two-dimensional histogram of the time-over-threshold of the first drift chamber versus that of the second, as illustrated in Figure 4.22. In Figure 4.21, the top panel shows the Δx when the incoming beam was gated on ^{15}N ions, and has two peaks corresponding to two bands of the correlation plot shown in Figure 4.19. The other panels from the upper one to the lower show the same as the top panel, selected with the gates defined in Figure 4.22. We observe that when a condition of higher time-over-threshold for both drift chambers is applied (like region 5), the lower peak, corresponding to the lower band of the correlation plot, is enhanced. This observation agrees with the assumption of a heavier particle in the lower band of the correlation plot.

In spite of the above, the origin of the lower band is not exclusively determined; however, the events in this band have different magnetic rigidities compared to protons. Therefore, in the analysis of the data throughout this thesis, only the events in the main band are selected using a graphical gate (see Subsection 5.1.4).

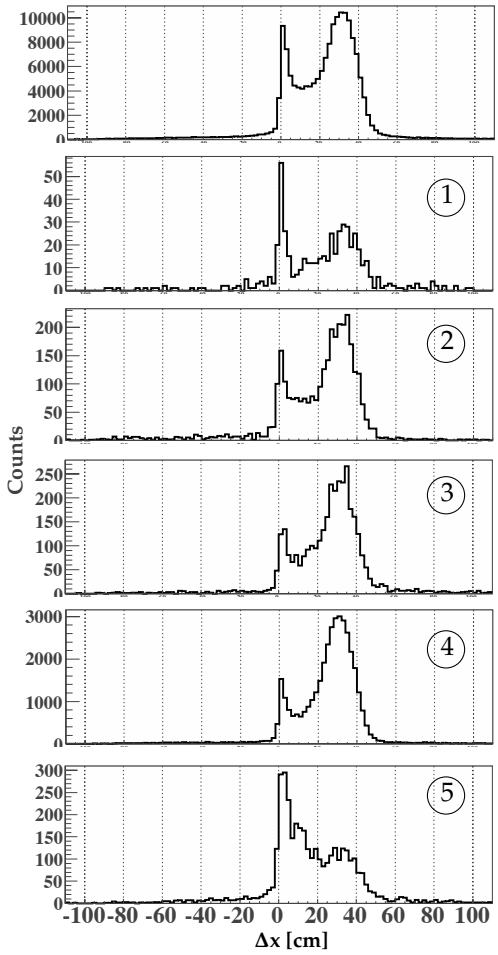

Figure 4.21: The Δx of raw data under different time-over-threshold conditions; all the plots are produced with the selection of ^{15}N as incoming ions. The top panel has no other conditions, and the panels labelled 1 to 5 have undergone the time-over-threshold cuts 1 to 5 illustrated in Figure 4.22.

Efficiencies of the drift chambers

The efficiencies of a layer in one of the drift chambers is calculated as

$$\text{efficiency} = 1 - \frac{N_0}{N_0 + N_1}, \tag{4.7}$$

in which N_0 and N_1 are the number of events with multiplicity zero and one in that layer, respectively, while the multiplicity of the other PDC layers are one. In this method, events with multiplicity larger than one do not appear in the efficiency calculation. Accordingly, the number of these events are counted and taken into account for calculation of cross sections. In other words, through this thesis the

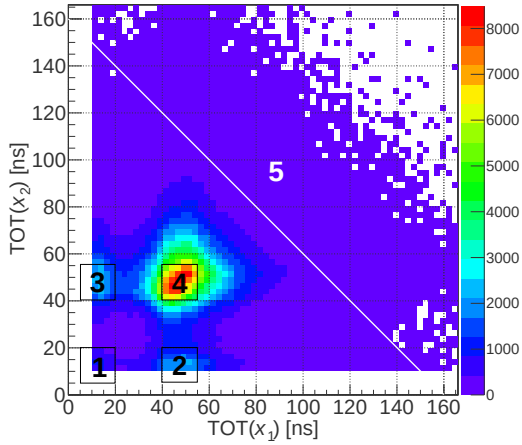

Figure 4.22: The time-over-threshold (TOT) of the X2 layer versus that of X1 layer. The five numbered regions define five gates on the time-over-threshold to be used in Figure 4.21. Gates 1 to 4 are the events inside the squares, and gate 5 is the whole area above the diagonal line.

events that have a multiplicity of two or larger in both drift chambers are excluded.

In order to explain the multiplicity conditions used for calculation of the efficiency, the terminology $[mnopq]$ is used to indicate a multiplicity of m, n, o, and p in X1, Y1, X2 and Y2 layers of the drift chambers, respectively, and q in the proton time-of-flight wall. For example, the multiplicity conditions for the efficiency calculation of the X1 layer can be given as: $N_0 = [01110^+]$, $N_1 = [11110^+]$, and similarly for other layers. The condition 0^+ means a multiplicity of larger than zero in the proton time-of-flight wall. This condition remains the same for the efficiency calculation of all layers.

On top of the multiplicity conditions, *correspondence conditions* are applied when counting both N_0 and N_1. The correspondence condition in horizontal direction, Δx, is only applied for efficiency calculation of Y layers. The Δx condition limits the events to the proton-peak region as shown in Figure 4.23, left panel. Similarly, a Δy condition is applied when the efficiency of X layers is calculated (see Figure 4.23, right panel). The correspondence region, indicated as blue shade, is an interval centred at the mean-value of a Gaussian fit, with a width of 2 times the FWHM.

Using Equation 4.7, the efficiencies are obtained for each layer of the drift chambers, and are given in Table 4.3. The combined efficiency of the two drift chambers is obtained by multiplication of individual efficiencies and is 78.8(0.5)%.

The efficiency of a drift chamber can vary in different regions of the active area. In order to calculate the efficiency for each region of the first drift chamber, the position information of the second drift chamber is used to define an array of pixels and vice versa. In this way, we obtain so-called *efficiency profiles* of the drift chambers such as in Figure 4.24, showing the efficiency profile of the first and second drift chambers, respectively. In each figure, the left panel shows the efficiencies and the right panel

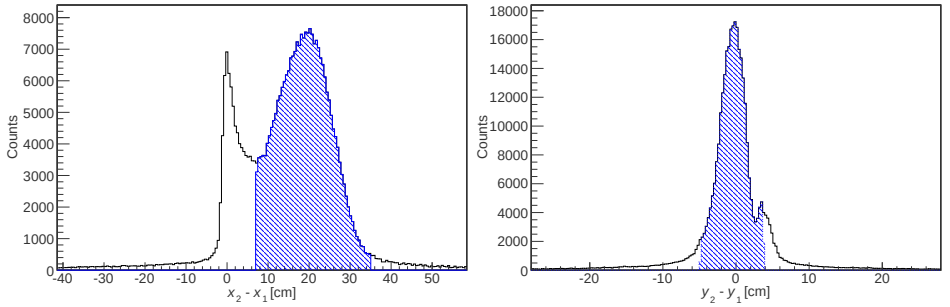

Figure 4.23: The shaded region indicates the selected range of Δx and Δy as conditions for efficiency calculation of Y and X layers, respectively.

shows the statistical uncertainties for each pixel. The white area on the right side of the first chamber profile, and on the left side of the second is due to a geometrical displacement of the chambers with respect to each other.

4.4.5 Proton time-of-flight wall (DTF)

The proton time-of-flight wall is an array of scintillator paddles, similar to TFW, for triggering and the time measurement of protons. DTF is composed of six vertical and two horizontal paddles, all of them read out from both ends using photomultiplier tubes. The horizontal paddles are installed at the back of the vertical paddles, which are placed side by side. Each vertical paddle has dimensions of $120\times20\times1.5$ cm^3, giving rise to a total active area of 120×120 cm^2.

Calibration

The calibration procedure of DTF is to some extent the same as that of TFW. However, the gains of the paddles were matched versus each other differently, because DTF does not have crossing paddles such as TFW (see Subsection 4.4.3). In order to match the gains and calibrate the QDC channels to common energy units, the cosmic muon data were used. A simple `Geant4` simulation was carried out, as explained in the following, to determine the energy deposit of cosmic muons in a DTF paddle.

The geometry included in the simulation contains only one DTF paddle. The event generator in this simulation generates muon particles with kinetic energies randomly and uniformly selected from an interval of 0.4 to 1.4 GeV. The generation points of the muons are uniformly distributed over a flat circle with a radius of 10 m, whose centre is located 2 m above the centre of the paddle. The muons are generated downward, with a uniform azimuthal-angle distribution, while their polar-angle distribution is weighted with a $\cos^2(\theta)$ distribution.

The energy-deposit spectrum of a DTF paddle in this simulation is depicted in the right panel of Figure 4.25. The maximum position of this spectrum was used to

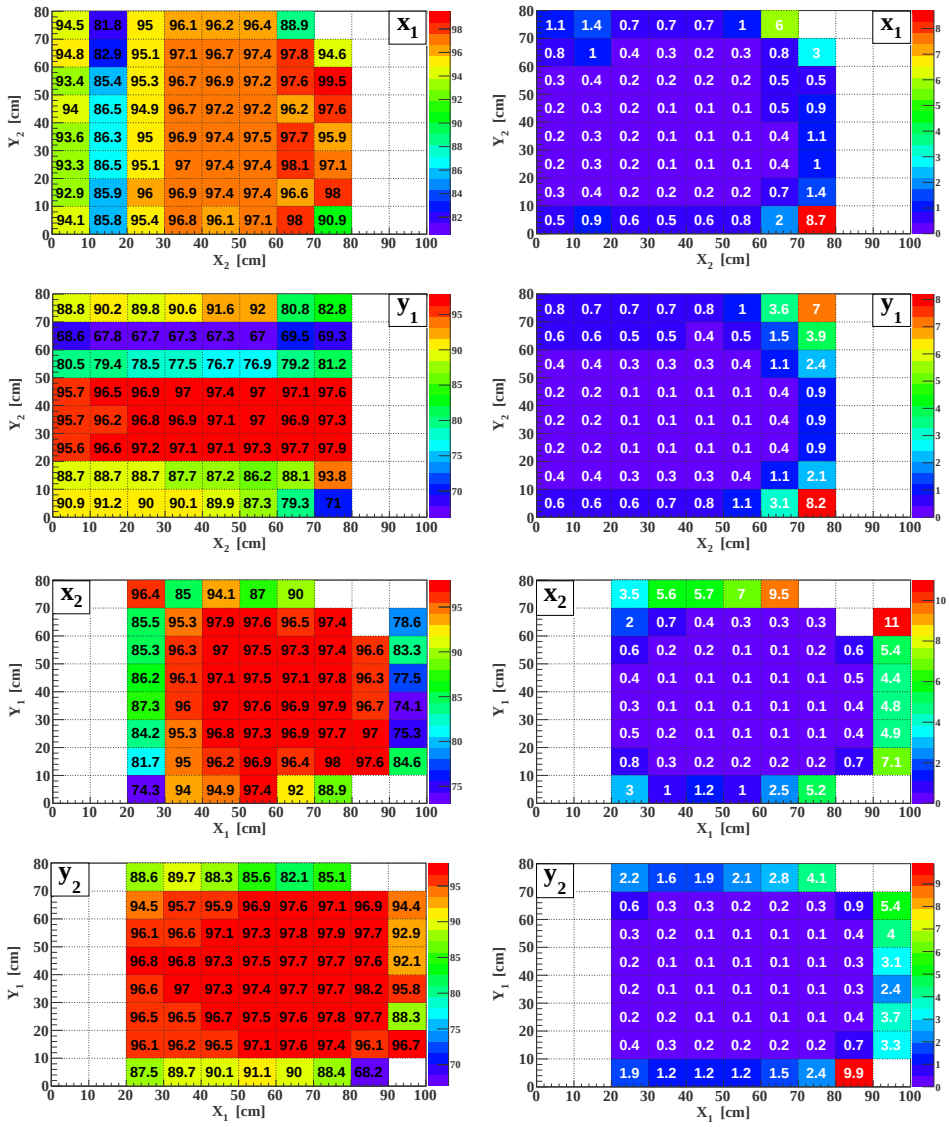

Figure 4.24: The efficiency profiles of the drift chambers. The left column gives the efficiencies per pixel, and the right column gives the statistical uncertainties for the corresponding pixels. The upper (lower) two rows are for the first (second) drift chamber. The malfunction of few wires reduces the efficiency in the region along those wires.

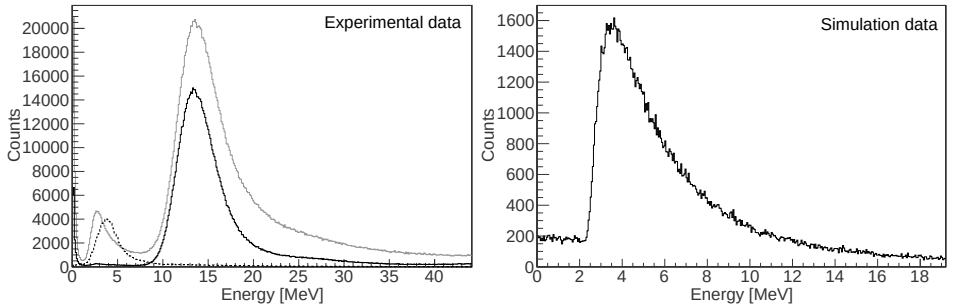

Figure 4.25: Left: energy spectrum of DTF under different trigger conditions; the grey and solid black histograms are generated under the DTF PROTON and the CRYSTAL-BALL SUM trigger conditions, respectively, and the dashed histogram is triggered mainly by cosmic events (the DTF COSMIC trigger pattern). Right: the simulated energy-deposit spectrum of a DTF paddle for cosmic muons.

match the gains of the DTF paddles versus each other and convert the energy values to MeV. The result of this process is shown in the left panel of Figure 4.25, in which different histograms are created under different trigger conditions. The grey histogram is the calibrated spectrum of the DTF under the trigger condition of the DTF itself (DTF PROTON, Tpat#16)[5], while for the solid black histogram, the CRYSTAL-BALL SUM trigger (Tpat#8) has been required, and the dashed histogram shows the events triggered mainly by the cosmic muons (DTF COSMIC, Tpat#4096).

4.5 Trigger scheme of S393

The general trigger scheme of S393 is the same as the previous LAND-R^{3}B experiments (see References [80, 85, 90]), but with slightly different combinations. Table 4.4 shows the trigger combinations forming different trigger patterns. Each trigger pattern ($Tpat$) is a 16-bit word[6], giving rise to 16 possible triggers ($Tbit$); $Tpat = 2^{(Tbit-1)}$. The position sensitive scintillator (POS) at the beginning of the setup generates the main trigger, only if at least two of its photomultipliers fire in coincidence. If the POS trigger is in coincidence with the Spill-on trigger from the synchrotron and is NOT in coincidence with the ROLU trigger, the so-called MINIMUM BIAS (MIN.B) trigger pattern is generated. This trigger pattern is the constant requirement of all physics trigger patterns (the first eight trigger patterns in Table 4.4). The Crystal Ball sum trigger is only produced if the sum of the analogue signals of the crystals exceeds a certain threshold, and it generates the CRYSTAL-BALL SUM trigger pattern, when it is in coincidence with the FRAGMENT trigger pattern. The CRYSTAL-BALL SUM trigger pattern is used as the condition for selection of the events with reaction. In other words, the reactions of interest in this work were gated us-

[5]For more information about the trigger scheme of S393 see Section 4.5.
[6]Only 15 bits are used in S393.

Table 4.4: The trigger patterns in S393. Here, ANDs and NOTs indicate coincidences and anti-coincidences, respectively. In this table and throughout this thesis, the names of the trigger patterns are typed in the SMALL CAPS `typewriter` fonts to be distinguished from the names of the trigger bits and detectors.

Number	Name	Description
1	MINIMUM BIAS (MIN.B)	Spill-on AND POS NOT ROLU
2	FRAGMENT	TFW AND MIN.B NOT pile-up
4	FRS S8	Spill-on AND S8
8	CRYSTAL BALL SUM	Crystal Ball sum AND FRAGMENT NOT late-trigger
16	DTF PROTON	DTF AND FRAGMENT
32	GOOD BEAM PILE-UP	MIN.B NOT pile-up
64	PIXEL†	Pixel detector AND MIN.B
128	NEUTRON	LAND AND FRAGMENT
256	CRYSTAL BALL MUON	Crystal Ball sum delayed NOT MIN.B
512	LAND COSMIC	LAND cosmic NOT MIN.B
1024	TFW COSMIC	FRAGMENT delayed NOT MIN.B
2048	CRYSTAL BALL GAMMA	Crystal Ball OR delayed NOT MIN.B
4096	DTF COSMIC	DTF delayed NOT MIN.B
8192	NTF‡ COSMIC	NTF NOT MIN.B
16384	CRYSTAL BALL L/R MUON	Crystal Ball L/R NOT MIN.B

†The pixel detector is a rectangular mask with an array of 21×21 pixels, each one filled with a small scintillator. This detector was located in front of the PSP for position calibration. However, it did not work during S393.
‡ NTF (New Time-of-Flight wall) was used in S393 only for test, and it had no role in the physics triggers.

ing a bit-wise AND operator[7], by the condition $(\texttt{Tpat\&8}) == 8$. The events with no reaction are selected using the FRAGMENT trigger pattern, $(\texttt{Tpat\&2}) == 2$.

Some of the trigger patterns are scaled down, in order to enable the data-acquisition system to process the events more effectively. For instance, the FRAGMENT trigger pattern is scaled down by a reduction factor of 64, because the events with this trigger pattern have not registered any reaction in Crystal Ball. This means that at every instance of trigger pattern 2, the data-acquisition system checks whether this trigger pattern has been recorded in the last 63 instances; if yes, this instance is ignored (the corresponding trigger bit remains null), if no, it is recorded. If all the trigger bits in an event remain null, that event is discarded. In this way, the system spends most of its time on the events with significant probability of reaction. CRYSTAL-BALL SUM is not scaled down, because it signals a reaction.

[7] & and == represent the bitwise AND and equality operators, respectively.

Trigger Pattern	Total	Dead-time correction	Scaled down	Dead time	Down-scale factor
========== IN SPILL ==========					
TPAT01: Good_Beam	38587514	21522599	168146	44.2%	128.0
TPAT02: GP+TFW	25372589	14977535	234024	41.0%	64.0
TPAT03: FRS_S8	170033323	95493176	46628	43.8%	2048.0
TPAT04: GP+CB_Sum	1018900	596457	596457	41.5%	1.0
TPAT05: GP+DTF	199851	117876	117876	41.0%	1.0
TPAT06: GB-pileup	26030422	15361787	120014	41.0%	128.0
TPAT07: PIX	1633	1324	1324	18.9%	1.0
TPAT08: GP+LAND	891288	522269	522269	41.4%	1.0

Figure 4.26: A typical output of the `showscaler` programme from setting#3. In the left column, "TPAT" followed by the trigger bit (*Tbit*) indicates the trigger pattern, and the last column shows the reduction factor for each trigger pattern.

The reduction factors of each trigger pattern may change during the experiment, specially when a new beam with new set of ions is used. In order to keep track of the reduction factors, a programme has been developed within `Land02` that uses the scaler values and gives the exact number of events under each trigger pattern before and after the scaling. Figure 4.26 shows a portion of a typical output of this programme. In each row, the precise value of the reduction factor can be obtained by division of the dead-time-corrected number (fourth column) by the scaled-down number (fifth column).

4.6 Fragment mass identification

An accurate determination of the reaction-fragment mass is necessary for a clean selection of the reactions of interest. In addition, the momentum distributions of the reaction products are determined using the reconstructed mass in combination with the measured time of flight. In S393, mass identification of the fragments relies on the tracking of ions before, through, and after the dipole magnet. A tracking programme has been developed[8], which evaluates the mass number of ions, A, based on their magnetic rigidities, $B\rho$ (see Equation 4.1). The tracking programme requires information of almost all in-beam detectors in order to reconstruct the mass of the reaction products.

To begin with, an incoming ion should be selected based on the reconstructed incoming charge and mass. Then, the measured position of the ion on the silicon strip detectors after the target (SSD#3 and SSD#4) are used to determine the angle and position at which the ion enters the magnetic field. Evaluation of the magnetic field at each point is performed using a set of field maps that have been measured for a few electric currents running through the magnet (see Figure 4.27). The magnetic field for other values of electric current are interpolated in between the measured ones.

Having the magnetic field at each point of the dipole magnet, it is possible to predict

[8]Ralf Plag. `http://ralfplag.de/tracker/`

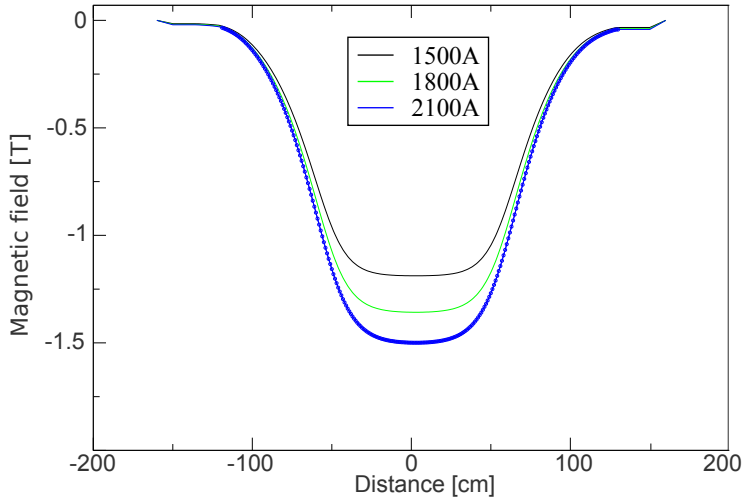

Figure 4.27: The measured magnetic fields at various distances from the centre of the magnet for different currents of the dipole magnet (Adapted from Ralf Plag).

the trajectory of the ion in the magnet. Following this trajectory the angle of the ion at the exit of the magnet is determined. This information is then used in determining the positions of the ion on the scintillating-fibre detectors. Subsequently, the difference between these obtained positions and the measured positions are minimised using a fit procedure. The fit procedure takes as input

- the ion position on SSD#3 and SSD#4,
- the ion position on the scintillating-fibre detectors,
- the electric current running through the magnet,
- the charge, mass, and velocity of the incoming ion.

The information of the incoming ion is used as primary guesses for the charge, mass, and velocity of the fragment, in order that a primary track can be generated. Then, the mass is varied in different directions until an optimum fit is found between the reconstructed track and the measured one. The optimum mass, from the fit, is used to reconstruct the velocity of the fragment. By comparing the reconstructed velocity with the incoming one, the time of flight of the fragment from the target to TFW is calculated. If the calculated time of flight differs substantially from the measured one, the difference is given as an input to the tracker for improving the time synchronisation. The tracking procedure is then repeated with the fragment velocity obtained in the first round, which improves the mass resolution. Similarly, other inputs of the tracking procedure can go through an iteration in order to optimise the mass resolution. Since this optimisation is highly charge-sensitive, a clean selection of the incoming and outgoing charges must be given as input. Also the nominal outgoing charge should be specified separately. Multiple charges can be tracked at the same time, provided that a nominal outgoing charge is assigned to each peak in the TFW energy spectrum.

The tracking procedure explained above is highly sensitive to the field maps. The

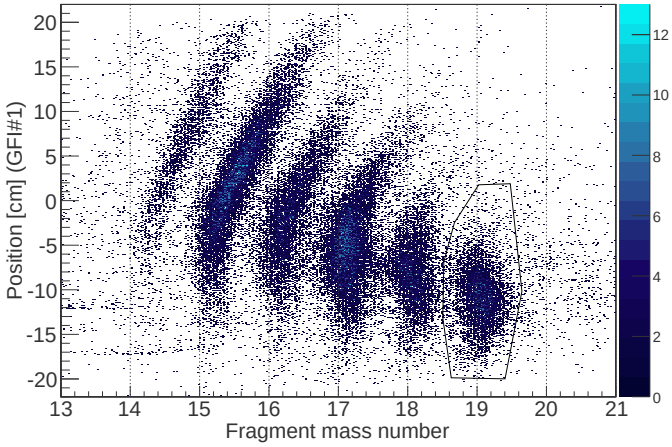

Figure 4.28: The fragment position in the GFI#1 versus the reconstructed mass from the tracker. The black polygon shows a typical graphical gate used to select the mass $A = 19$. The CRYSTAL BALL SUM trigger pattern and an energy-deposit condition for $Z = 7$ has been applied. Therefore, the selected events correspond to ^{19}N.

present evaluated field maps are from rather old measurements, and they are prone to large uncertainties. In order to tackle the lack of accuracy in the magnetic field, a method has been developed that varies the measured positions of the fragment before and after the magnet in directions that result in better mass resolutions. This method produces an optimum set of calibration offsets to be applied to the measured positions. These offsets, eventually, compensate for the lack of accuracy of the magnetic field. Due to the sensitivity of the tracking method to the selected charge and mass, if the calibration offsets are optimised for a certain ion, only that ion and its next neighbours can be tracked reliably using these set of offsets.

Figure 4.28 illustrates an example of the mass reconstruction for the reactions with incoming ^{20}O and outgoing nitrogen. The plot shows the fragment position on the first scintillating-fibre detector versus its reconstructed mass from the tracker, with a graphical gate around mass 19, shown as the black polygon. This gate is used as the outgoing mass selection during the data analysis which will be explained in the next chapter. In this example, the position offsets are optimised for ^{20}O. It can be observed that the mass of ^{19}N is nicely reconstructed, but the lighter masses show a dependence on the positions measured by the scintillating fibre detectors.

4.7 Outlook of the setup: R^{3}B at FAIR

The LAND setup has proven to be a successful device during the last two decades. However, in order to extend or improve the physics goals of the setup, a major upgrade is necessary. The R^{3}B (Reactions with Relativistic Radioactive Beams) programme is proposed as part of the FAIR project in order to facilitate investigations of nuclear reactions, using direct-reaction techniques. Figure 4.29 shows a schematic

view of the R^{3}B experimental setup. Obviously, the overall structure of the future setup is similar to the current LAND setup. However, the R^{3}B setup will include several complementary elements, namely a mass spectrometer and a versatile recoil detector around the reaction target.

As indicated in Figure 4.29, the setup can be operated in two modes: 1) Large-acceptance mode, in which the reaction products are deflected toward left (looking in the direction of the beam), using the large-acceptance dipole magnet. In this mode, the whole solid-angle acceptance of the setup is used for detection of the outgoing particles; 2) High-resolution mode, in which the reaction products are guided to the magnetic spectrometer using the dipole magnet. This mode of operation is foreseen for precise measurements of momentum and mass.

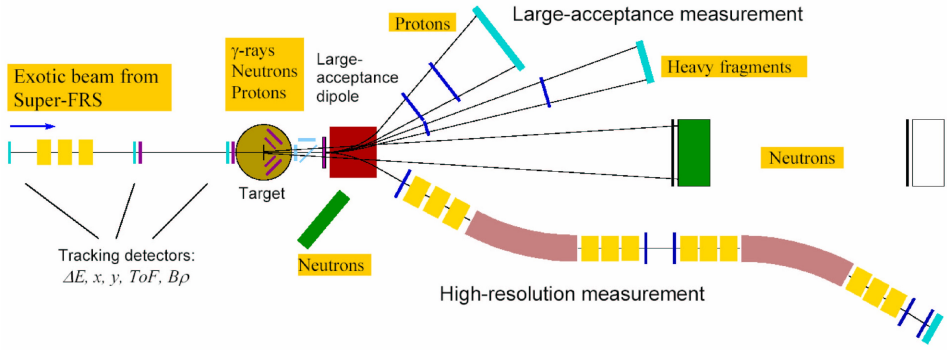

Figure 4.29: The schematic view of the future R^{3}B setup.

The reaction target will be surrounded by a recoil detector, including an array of silicon strip trackers and a calorimeter. The silicon strip trackers will measure the track angle of the charged reaction products as well as their energy deposit, and the calorimeter is meant for the total energy and a rough measurement of the angle of the particles. The calorimeter comprises an array of CsI(Tl) scintillators that not only fully absorb and detect the decay photons, but also detect the knock-out protons in the forward angles. The present design of the calorimeter, called CALorimeter for In-Flight gammA detection, CALIFA, accommodates more than two thousand CsI(Tl) crystals in a barrel-like geometry. When ultimate resolutions are required for the energy measurements of the decay photons, the use of a Germanium calorimeter, called Advanced GAmma Tracking Array, AGATA, is envisaged, as an alternative. Both CALIFA and AGATA are at medium stages of construction, while samples of their crystals are tested in combination with different read-out systems (see References [91, 92] for CALIFA, and [93] for AGATA). Some other elements of the R^{3}B setup have already been manufactured and are used in the current experiment, namely the proton drift chambers and the silicon strip detectors.

The R^{3}B setup will provide the facility to investigate nuclear structure and reactions in the regions of the nuclear chart near or even beyond the drip lines.

Chapter

Analysis and Results

In the previous chapter, the calibration of the experimental data and the track reconstruction were explained. These data will be used for the selection of the reactions of interest as will be explained in Section 5.1. Subsequently, some observables are introduced in Section 5.2, and the analysis methods that are involved in obtaining them are described. The final results are presented in Section 5.3 along with a brief explanation of systematical uncertainties, that is followed by a discussion of the findings and conclusions.

5.1 Selection of events

In this thesis, the reactions of interest are quasi-free proton- and neutron-knockout from ^{20}O, namely $p(^{20}\mathrm{O}, pp^{19}\mathrm{N})$ and $p(^{20}\mathrm{O}, p^{19}\mathrm{O})n$. We seek reactions in which a proton or a neutron has been knocked out from ^{20}O via a quasi-free collision with a proton in the CH_2 target. ^{20}O as the incoming ion and ^{19}N or ^{19}O as the outgoing ion should be selected to guarantee only one-nucleon-removal reactions. Furthermore, to make sure that only the quasi-free reactions are considered, more conditions need to be applied.

The trigger conditions were explained in Section 4.5: the CRYSTAL-BALL SUM trigger pattern is used to select the events with a reaction in the target, and the FRAGMENT trigger pattern for the selection of events without a reaction. The proton multiplicity is limited to 2 for the proton knockout reactions; either two protons detected in the Crystal Ball, or one proton in the Crystal Ball and another one in the drift chambers. For the neutron knockout reaction, detection of only one proton has been required; either one proton in the Crystal Ball and none in the drift chambers or one in the drift chambers and none in the Crystal Ball. Selection of the incoming and outgoing ions as well as other conditions that are used for the selection of the events of interest are described in this section.

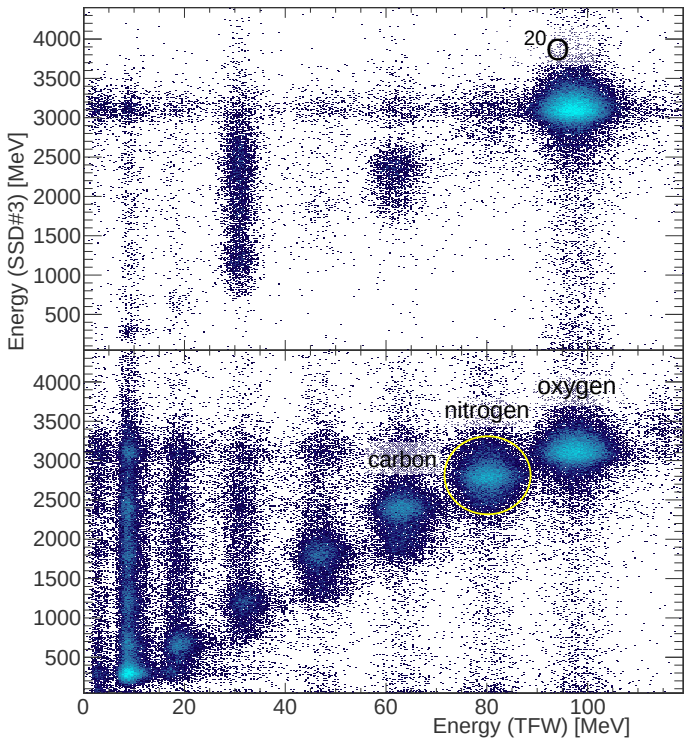

Figure 5.1: Selection of the outgoing-ion charge. The energy signals of SSD#3 versus TFW gated by the FRAGMENT trigger (upper panel), and by the CRYSTAL-BALL SUM trigger (lower panel). The ellipse in the lower panel shows the gate for the selection of nitrogen.

5.1.1 Incoming and outgoing ion selection

As explained in Section 4.2, the charge identification of the incoming ions is based on their energy deposit in the pin-diode, and the determination of their mass on the Fragment Separator (FRS) information (see Figure 4.5). The incoming-ion was gated using the conditions: $7.5 < Z < 8.5$ and $2.48 < A/Z < 2.52$, which results in a very clean selection of ^{20}O ions. The outgoing ion is selected in two steps: the charge is selected using the energy deposit information of SSD#3 and TFW, as illustrated in Figure 5.1. This figure shows the energy values of SSD#3 versus those of TFW, when the incoming beam is gated on ^{20}O. The upper panel shows the events gated by the FRAGMENT trigger that selects the events with no reaction, while the events in the lower panel are gated by the CRYSTAL-BALL SUM trigger that triggers on reactions. In the upper panel, the strong concentration of events at the top-right is due to the beam ions without reaction, and hence, corresponds to the atomic number $Z = 8$. The corresponding locus in the lower panel is then assigned to oxygen.

Similarly, the incoming ion can be gated on other ions, and the concentrations of events on the diagonal line in the lower panel can thus be labelled correspondingly.

It is then easy to select the outgoing charge of interest by an elliptic gate, defined as

$$\left(\frac{E_{\mathrm{TFW}} - E_{0,\mathrm{TFW}}}{\Delta E_{\mathrm{TFW}}}\right)^2 - \left(\frac{E_{\mathrm{SSD}} - E_{0,\mathrm{SSD}}}{\Delta E_{\mathrm{SSD}}}\right)^2 < 1, \tag{5.1}$$

in which E_{TFW} and E_{SSD} are the energy deposits of ions in TFW and SSD#3, respectively. E_0 and ΔE for each detector are obtained by using the fit of a Gaussian distribution to the one-dimensional energy spectrum of that detector. An example of this gate is shown in the lower panel of Figure 5.1. In some events the charge of the outgoing ion changes on the path from SSD#3 to TFW. These events appear as the events far from the diagonal line, and they are filtered out using the elliptic gate.

In the second step, the mass number is selected using the tracking procedure explained in Section 4.6.

5.1.2 Angular correlations

By selecting the incoming and outgoing ions, we select the one-nucleon-removal reactions, but we need more information to ensure selection of quasi-free knockout reactions. A clear signature of the quasi-free scattering is the angular correlation of the knocked-out nucleons. In the energy range of S393 (beam energies above 400 MeV per nucleon), the binding energy of nucleons in the nucleus (around 8 MeV) is very small compared to their kinetic energy. Therefore, kinematics of the two outgoing nucleons in a quasi-free knockout reaction is dominated by nucleon-nucleon elastic scattering. Angles are defined in spherical coordinates, with the z-axis in the direction of the beam and the origin at the centre of the target. In this frame, the two nucleons scatter at an angle around 81° with respect to each other, and the momentum vectors of the projectile and the scattered particles are in the same plane.

Figure 5.2 shows the kinematic calculation of the scattering angles. These calculations were carried out using a code originally developed by L. Chulkov and later translated from `FORTRAN` to `C` and improved by Valerii Panin[1]. The code assumes an isotropic distribution of the scattered nucleons in the centre-of-mass frame, and calculates the kinematic variables of a quasi-free knock-out reaction based on the conservation of energy and momentum. Figure 5.2 shows what we could expect from the experimental data for $p(^{20}\mathrm{O}\,, pp^{19}\mathrm{N})$ at a bombarding energy of 415 MeV per nucleon in the laboratory frame. The momenta of the projectile-like fragments are described by Gaussian distributions, the width of which are given to the code manually from the measured momentum distributions.

Figure 5.3 shows the measured angular correlations between two protons, using the data of the Crystal Ball detector. As mentioned in Subsection 4.3.1, the information of the box silicon detectors are not used in this analysis, and all the angles in Figure 5.3 are obtained from the Crystal Ball information. The events in this figure are gated on the incoming ions ^{20}O, the outgoing ions ^{19}N, and the `CRYSTAL-BALL SUM` trigger. Although the Crystal Ball detector has a relatively poor angular resolution, the correlation between the scattered protons is clearly visible.

[1] Private communication.

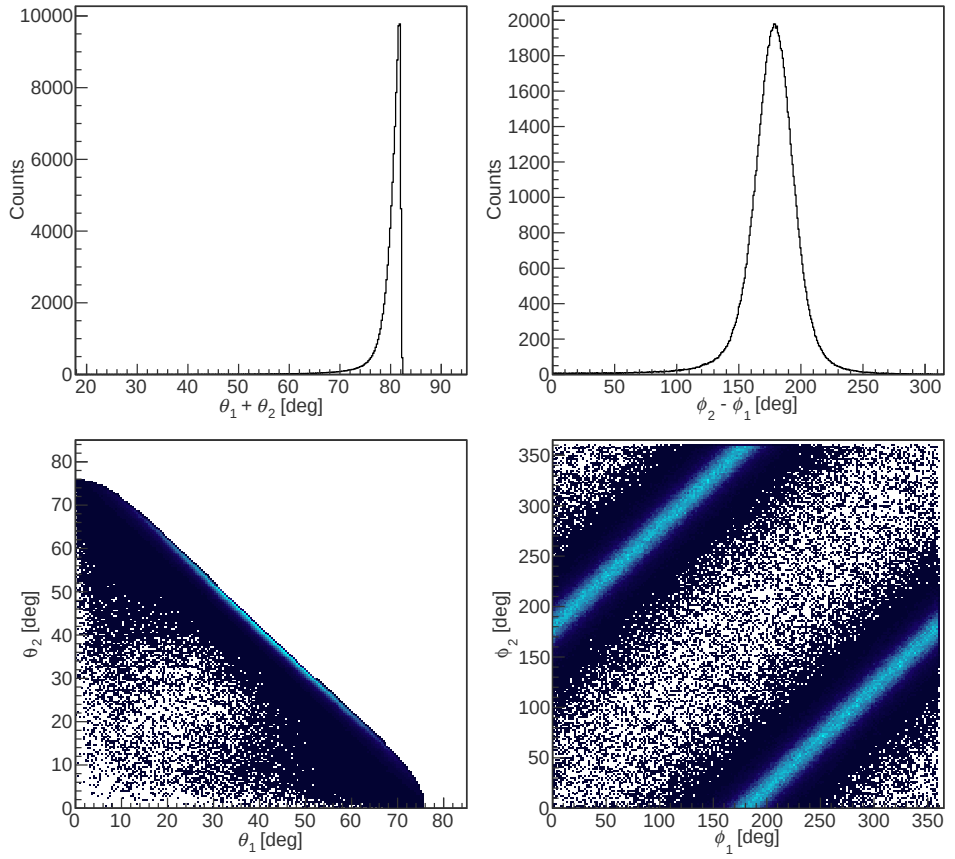

Figure 5.2: The calculated angular correlations of the knocked-out protons, using L. Chulkov's kinematic code. θ and ϕ are the polar and azimuthal angles in a spherical coordinate frame, in which the z-axis is in the direction of the beam, and the origin is at the centre of the target.

Based on the histograms in Figures 5.2 and 5.3, the following angular conditions were required for the selection of the quasi-free proton knockout reactions:

$$\theta_1 + \theta_2 \in [60, 100] \tag{5.2}$$

$$|\phi_1 - \phi_2| \in [100, 260], \tag{5.3}$$

in which $\{\theta_1, \theta_2\}$ and $\{\phi_1, \phi_2\}$ are the polar and azimuthal angles of the scattered protons, respectively. No angle condition is applied for the neutron-removal reactions, because the detection of neutrons in Crystal Ball has a very low efficiency and in most of the neutron knockout events only the scattered proton is observed. Instead, a multiplicity condition is used to remove random coincidences as much as possible. This condition admits only the events with either one proton in Crystal Ball and none in the proton branch or one in the proton branch and none in Crystal Ball.

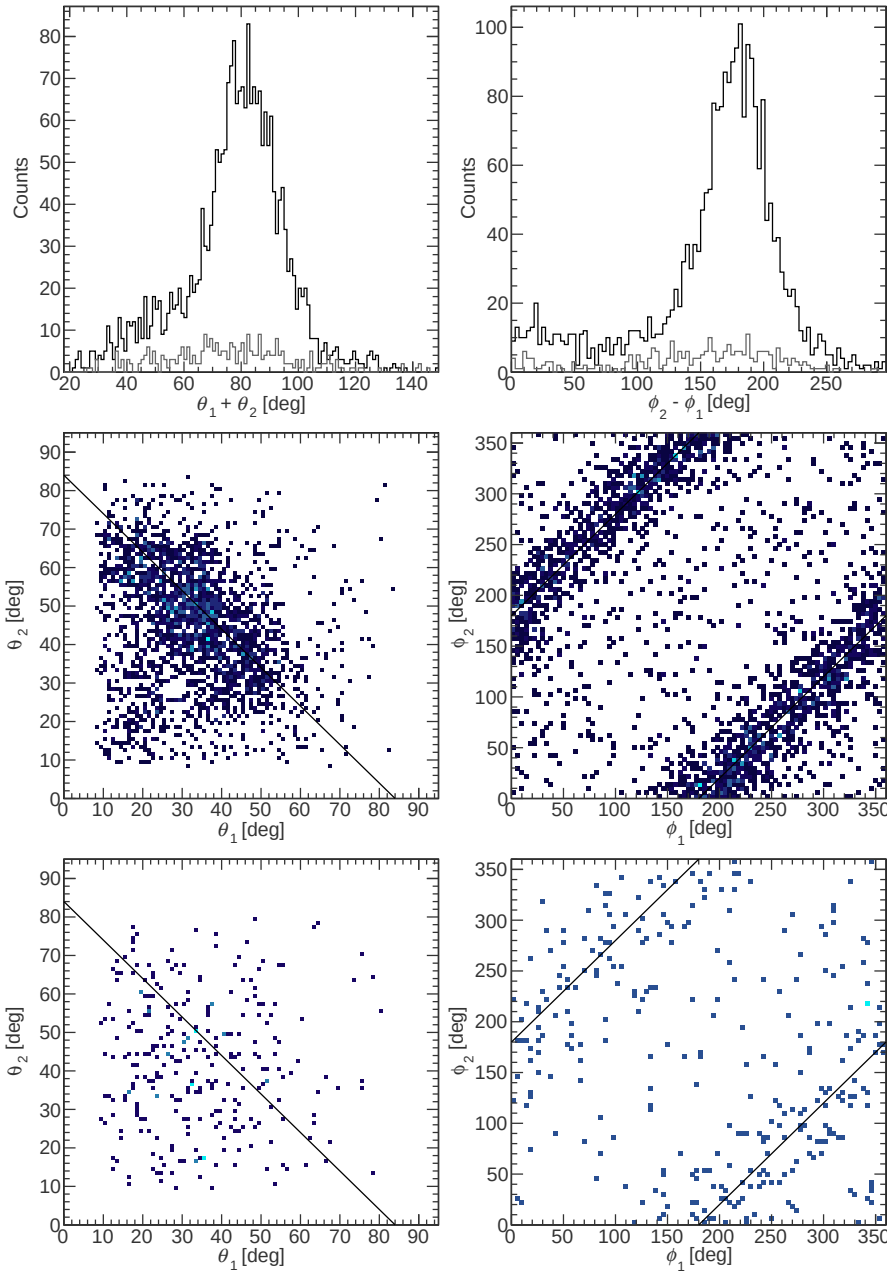

Figure 5.3: Same as Figure 5.2, but from the Crystal Ball data. The black and grey histograms in the top panels are from CH_2- and carbon-target data, respectively. The histograms in the middle and bottom panels come from the CH_2- and carbon-target data, respectively.

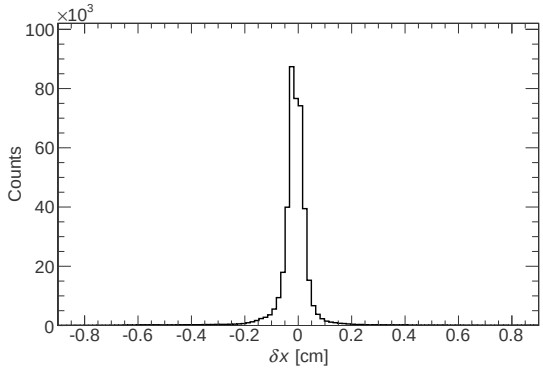

Figure 5.4: Position residual of the first fibre detector. See text for details.

5.1.3 Tracking condition

A complementary condition is applied to remove the events that have not been tracked successfully. The tracking programme gives *position residuals*, which are defined as the reconstructed positions minus the measured ones (see Section 4.6). The reconstructed positions are obtained from the fitted track. The programme optimises every track so that these residuals are minimum; however, deviations from zero may occur. Figure 5.4 shows the position residuals of the first fibre detector. A cut has been set to remove every event whose position residuals on the scintillating-fibre detectors are larger than 0.1 cm or smaller than -0.1 cm. This interval was selected based on the position resolution of the fibre detectors (0.1 cm).

5.1.4 Position on the drift chambers

As discussed in Subsection 4.4.4, when the reconstructed horizontal position of particles on the first drift chamber is plotted versus that of the second one, two distinct bands are observed (see Figure 4.19 left panel). It was argued that the lower band is due to light ions with larger magnetic rigidities than that of protons, such as deuterons or ^{4}He ions. A graphical gate is applied on the horizontal positions of the two drift chambers, in order to exclude events that are from this band or other sources of background in the drift-chamber data. Figure 5.5 illustrates the graphical gate applied on the correlation of the horizontal positions of the protons obtained from the two drift chambers.

5.2 Analysis concepts

As explained in Section 2.2, the inclusive cross sections are required in order to obtain the spectroscopic factors. In the previous section, the criteria for the selection of the reactions of interest were explained. Since the CH_2 target has a considerable

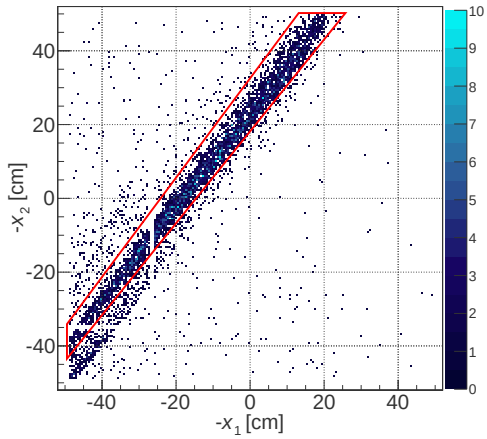

Figure 5.5: The selection of events on the drift chambers. The red quadrilateral shows the gate applied in order to select the events of interest.

amount of carbon, reactions of the beam with the carbon nuclei contribute to the total cross section. In this section, first the cross section formula is given and then the background subtraction method is explained.

5.2.1 Cross section

For the reaction of an ion beam with a certain target, the cross section is given by

$$\sigma = \frac{R}{I}\frac{1}{n} \tag{5.4}$$

in which, R is the reaction rate, I the beam intensity, and n the number density of the target. The number density is $n = t\ N_A/M$, where N_A is Avogadro's constant, M is the molar mass of the target material (the scattering centres), and t is the areal density of the target in $\mathrm{g/cm^2}$.

The reaction rate is obtained from the number of reactions in a certain time interval, and the beam intensity comes from the total number of incoming ions in that interval. The number of reactions is counted using the selection criteria explained in Section 5.1, and it should undergo a certain number of corrections accounting for the efficiencies and geometrical effects. These corrections will be explained in Subsections 5.2.3 and 5.2.4. The number of incoming ions is counted using the FRAGMENT trigger pattern, multiplied by the trigger reduction factor, which is 64 for the data of this thesis (see Section 4.5).

5.2.2 Invariant mass

The invariant mass of a system is the subtraction of its total momentum from its energy. The invariant mass of any system has to be conserved when the configuration

of the constituents of the system changes. A specific example of interest in the current work is the decay of an unbound nucleus. The invariant mass of an unbound nucleus at rest is the sum of its rest mass (the mass in the lowest energy state) and the possible excitation energy. Consequently, if the invariant mass of an unbound nucleus is determined using the energy and momentum measurements of its decay products, the excitation energy can be obtained by subtraction of the rest mass from the invariant mass,

$$E^{\star} = \mathcal{M} - m_I, \tag{5.5}$$

where m_I is the rest mass of the mother nucleus and $\mathcal{M}$ is the invariant mass.

The invariant mass is determined using the energy-momentum four-vectors, $\mathcal{P}_i$, of all decay products,

$$\mathcal{M} = \left| \sum_i \mathcal{P}_i \right|. \tag{5.6}$$

Equations 5.5 and 5.6 will be used in Subsection 5.3.2 for obtaining the excitation energy spectrum of the unbound states of ^{19}N.

5.2.3 Subtraction of target background

In S393, CH_2 was used as the reaction target (see Table 4.2), which includes carbon and hydrogen nuclei. But we are only interested in reactions of the beam with hydrogen. Therefore, the background reactions with the carbon nuclei must be subtracted. For this purpose, a few hours of beam time were dedicated to experiments with the carbon target, in each FRS setting (see Table 4.1). Using these carbon-target data, we can determine the contribution of the carbon reactions in the CH_2-target runs. Here, the subtraction of the carbon contribution is demonstrated for the cross section measurements, but the method is the same for other variables, such as momenta and scattering angles.

The subtraction requires scaling both CH_2 and carbon-target data using their corresponding luminosities, where luminosity is defined as the number of incoming ions multiplied by the number of reaction centres per unit area. In cross-section calculations, the variable of interest is the number of reactions relative to the number of incoming ions. If the number of the reacted ions and the total number of incoming ions in the CH_2-target run are $N_r^{CH_2}$ and $N_i^{CH_2}$, respectively, and the same variables in the carbon-target run are N_r^C and N_i^C, respectively, the number of reactions with hydrogen nuclei in CH_2 is

$$N_r^H = \frac{1}{2}(N_r^{CH_2} - f N_r^C) \ , \quad f = \frac{L^{CH_2}}{L^C} \tag{5.7}$$

where f is the factor that normalises the number of reactions with carbon in the CH_2 run with respect to the same number in the carbon run, and L^{CH_2} and L^C are

the luminosities in the CH_2 and the carbon runs, respectively;

$$\begin{aligned} L^{CH_2} &= n_{CH_2} N_i^{CH_2} \quad \text{with} \quad n_{CH_2} = t_{CH_2} N_A / M_{CH_2} \\ L^{C} &= n_{C} N_i^{C} \quad \text{with} \quad n_{C} = t_{C} N_A / M_{C} \end{aligned} \tag{5.8}$$

t_{CH_2} : Areal density of the CH_2 target
t_C : Areal density of the carbon target
M_{CH_2} : Molar mass of CH_2
M_C : Molar mass of carbon

The coefficient $\frac{1}{2}$ appears, because the number of hydrogen atoms in CH_2 is twice as much as the number of carbon atoms. Now, using Equation 5.4 we obtain the cross section of reactions from protons in the CH_2 target:

$$\sigma_H = \frac{N_r^H}{N_i^{CH_2}} \frac{1}{n_{CH_2}}. \tag{5.9}$$

5.2.4 Efficiencies and acceptances

The cross sections given by Equation 5.4 are based on counting the number of reactions and the total number of incoming ions, and these counts bear uncertainties from the experiment. Besides the subtraction of the target background, which was explained in the previous section, other imperfections should be taken into account, in order to improve the accuracy of the cross-section determination. First of all, the detection elements of the setup are not perfect, and there is a chance that they fail to produce a signal for a hit, which results in the loss of events. In other cases, the geometrical coverage of the detectors may be smaller than the kinematical phase space of the reactions of interest.

Therefore, two distinct sources of event loss should be accounted for: the *geometrical acceptance* of the detection elements, and *detection efficiencies* which are due to imperfections of the detectors. Equation 5.4 can then be rewritten in the following form

$$\sigma = \frac{N_r}{\epsilon_{geom}.\epsilon_{det}} \frac{1}{nI}, \tag{5.10}$$

in which ϵ_{geom} and ϵ_{det} are the total geometrical acceptance and the total detection efficiency, respectively. N_r is the number of reactions counted under the conditions explained in Section 5.1. Without considering these corrections, Equation 5.4 gives the normalised *yield* of the reaction.

Part of these corrections (ϵ_{geom} and ϵ_{det}) can be dropped if equivalent selection criteria are applied when counting events with and without reactions. For instance, when calculating cross sections using Equation 5.4, if equivalent criteria are applied for evaluating both R and I, the same efficiencies will be involved in the numerator and denominator, and hence those efficiencies cancel out. The equivalent selection

criteria are possible for most of the detectors in the setup, but not for the Crystal Ball detector or the drift chambers. Therefore, their correction factors must be evaluated and taken into account. In the next subsections, various corrections are explained.

5.2.5 Geometrical acceptance of the setup

Every detection element whose data are used in the analysis should be either large enough to cover the whole geometrical spread of the particles, or its geometrical coverage should be evaluated. For position-sensitive detectors, the geometrical coverage has been verified using their position information. For instance, as shown in Figure 5.6 for TFW, the horizontal and vertical position distributions of the reacted ions are well within its geometrical coverage (189×149 cm^2). In each panel of Figure 5.6, the grey and black histograms show the position distributions for mass number 19 and 20, respectively.

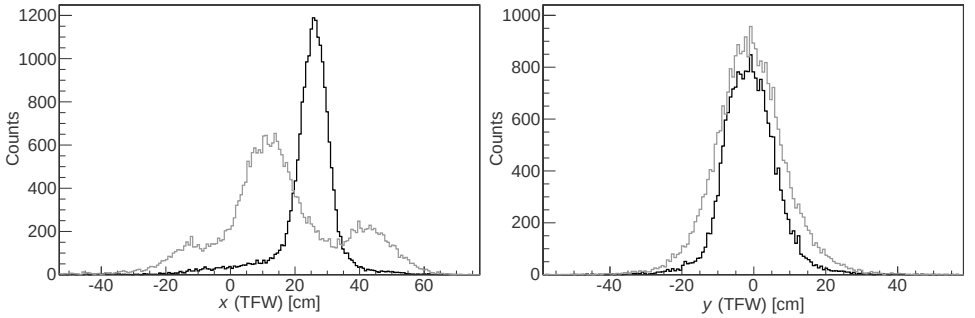

Figure 5.6: Geometrical coverage of TFW for the fragments of interest. The left and right panels show the horizontal and vertical distributions of the fragments with mass number 19 (grey) and 20 (black). Besides the mass-number selection, CRYSTAL-BALL SUM trigger has been required (see Subsection 4.4.3 for an explanation of the position measurement using TFW).

The geometrical acceptance of other position-sensitive detectors has been verified, in a similar manner, except for the drift chambers and Crystal Ball. The reconstructed positions on the first drift chamber are shown in Figure 5.7. The vertical positions of the events are well contained within acceptance of the drift chamber ($(-40, 40)$ cm for y coordinates). However, in the horizontal direction some events are cut out at the left edge of the active area of the detector, $(-50, 50)$ cm, which suggests that some of the protons have missed the drift chambers. Therefore, the geometrical acceptances of the drift chambers have been obtained from a simulation, as explained in the following.

Simulations for the detection acceptance

A simulation was performed within the package `R3BRoot` [94], which is a subpackage of `FairRoot` [95], and contains the geometry of the LAND-R^{3}B setup, but

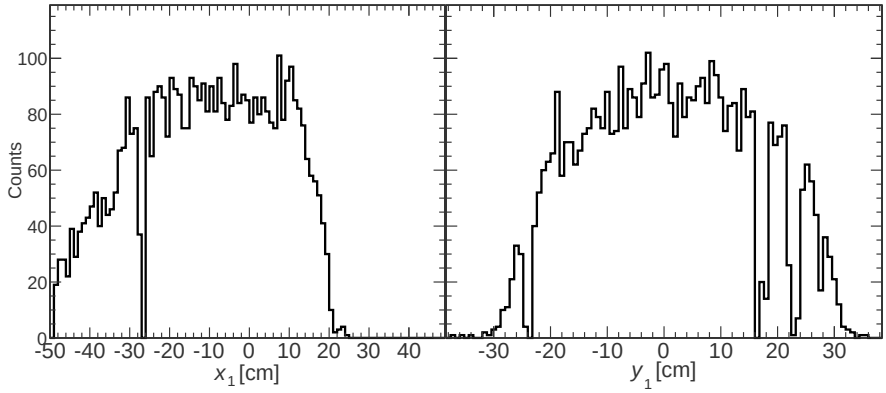

Figure 5.7: The reconstructed positions with the first drift chamber. The reaction selection conditions explained in Section 5.1 have been applied. It seems that the geometrical coverage of the first drift chamber is not enough on the left edge. The gaps are due to broken or faulty wires.

with no specific detector information such as detection thresholds and digitisation; therefore, the simulation is purely geometrical. In the geometry of the simulation, the positions of the drift chambers and the GFIs are the same as the ones in the S393 experiment. The event generator in this simulation is based upon the kinematics code by V. Panin (see Subsection 5.1.2), and it generates for each event two nucleons and the corresponding knockout residue fragment (two protons and a ^{19}N ion for the proton knockout reaction, and a proton, a neutron, and an ^{19}O ion for the neutron knockout reaction). The generation point is at the centre of the reaction target, and the z-axis is assumed in the direction of the beam in the experiment. The magnetic field is adjusted in a way that the position histograms of ^{19}N ions on the GFIs peak at the same positions as in the experiment. Figure 5.8 shows the simulated position spectrum (left panel) in comparison to the experimental spectrum (right panel).

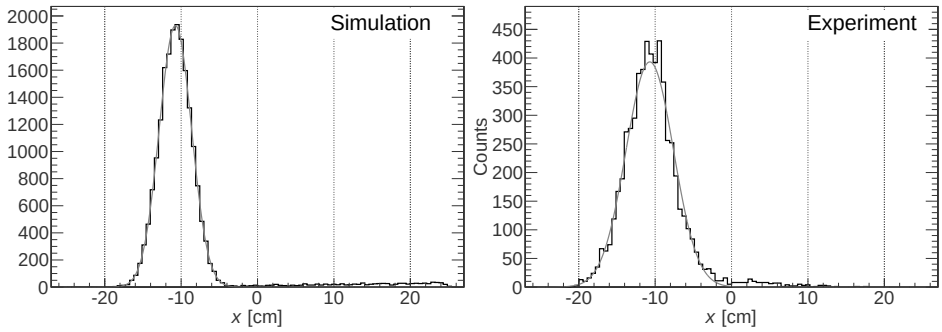

Figure 5.8: Left: position spectrum of GFI#1 for ^{19}N ions in the simulation (width $\sigma = 2.1$ cm); Right: the experimental position spectrum (width $\sigma = 3.1$ cm).

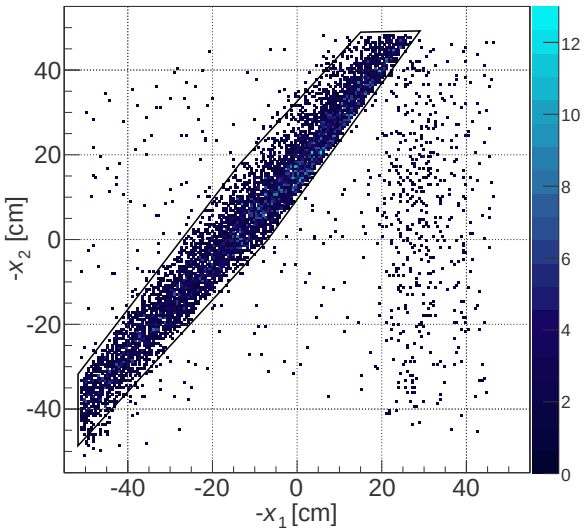

Figure 5.9: The correlation between the measured horizontal positions of protons on the first and second drift chambers, as obtained by the `R3BRoot` simulation.

Based on the geometry of the beam pipe, if the generated nucleons have a polar angle smaller than around 80 mrad, they travel through the exit pipe, which leads to the dipole magnet. The simulation shows that 97% of the events that travel through the exit pipe will be detected by the drift chambers.

Having the magnetic field adjusted as above, we obtain the correlation of the values of the horizontal position from the drift chambers in the simulated data, as depicted in Figure 5.9. Using this plot we can estimate the percentage of the events that are from a quasi-free reaction, and the knocked-out proton falls inside the graphical gate depicted in Figure 5.5 as

$$\epsilon_{gate}(\mathrm{PDC}) = 1 - \frac{n_{gate}}{n_{all}},$$

where n_{all} is the total number of events that satisfy the multiplicity conditions of the drift chambers, and if any of these events are included in the graphical gate in Figure 5.9, they are counted as n_{gate}. The simulation shows that around 10% of the protons that end up in the proton branch are excluded by the graphical gate, that is $\epsilon_{gate}(\mathrm{PDC}) = 90\%$. It must be noted that, based on this simulation, less than 0.5% of the quasi-free knockout reactions result in a proton that travels through the proton branch. It is to say, only $0.5\% \times 10\% = 0.05\%$ of the quasi-free-reaction events are excluded by the graphical gate. Therefore, the influence of this gate in the total detection efficiency can be ignored.

Crystal Ball acceptance

The Crystal Ball detector has a nearly full angular coverage around the scattering chamber, except for the entrance and exit beam pipes and the support system at the bottom. It gives an acceptance of around 97% for the detection of the prompt decay photons. Nevertheless, in the present analysis, all the final bound states of each reaction residue are included in the analysis. Thereby, no selection of the photon energies is necessary and the main interest is in the detection of the scattered and knocked-out protons rather than photons.

The protons from reactions eject in the forward direction, where every crystal has a read-out for protons; however, this does not ensure a complete detection of the forward-angle protons. The exit beam-pipe limits the angular coverage of the Crystal Ball to polar angles larger than 7.8° ($\theta > 7.8°$). Moreover, the larger the scattering angle, the smaller the kinetic energy of the proton, which implies that the protons scattered at large polar angles may be not energetic enough to reach the Crystal Ball. This is because of the aluminium wall of the vacuum chamber and other obstacles such as the target wheel and its moving machinery. We are thus interested to know the range of the scattering angles at which protons are energetic enough to reach the Crystal Ball detectors. This has been carried out using the same simulation as explained in the last subsection.

The Crystal Ball geometry in the simulation is the same as the one in the experiment, including 162 crystals in four different shapes. In addition, some other geometrical elements have been implemented in the geometry; such as the metal case of each crystal, the reaction chamber, the silicon detectors, the target wheel, and part of the holding structure of the silicon detectors.

Figure 5.10 shows the distribution of the polar angles of the generated (grey) and detected (black) quasi-free-scattered protons. The black histogram shows the detected protons in the Crystal Ball if the proton multiplicity equals two. From the output of this simulation it can be seen that the protons scattered at angles above 71° do not reach the Crystal Ball detectors. Therefore, the geometrical acceptance of Crystal Ball is between 7.8° and 71°.

5.2.6 Detection efficiencies

Fragment branch

There are three detectors in the fragment branch, GFI#1, GFI#2, and TFW, for which the efficiencies have been calculated. These efficiencies are determined based on the position information of the detectors. First, the total number of events that satisfy the FRAGMENT trigger pattern and have a non-zero multiplicity in at least two of the three detectors is counted as n_{all}. Subsequently, a track is reconstructed using the position information of two of the three detectors. The reconstructed position of the track on the third detector is then compared with the actual position measured by that detector. If these two positions match, the event is counted for n_{track}. Finally, the efficiency is obtained from $\epsilon = n_{track}/n_{all}$. For these calculations, ten million

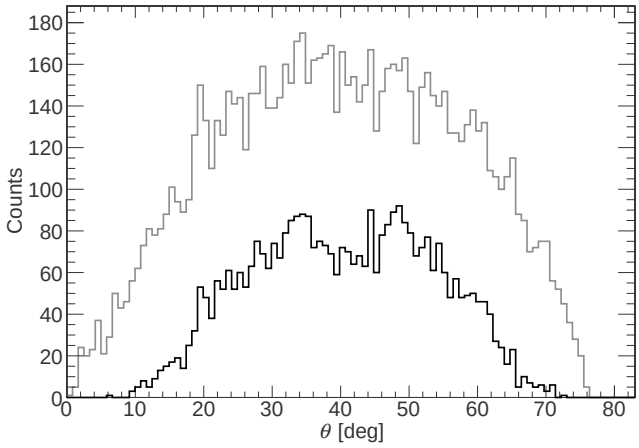

Figure 5.10: The simulation of the polar angle of the quasi-free-scattered protons in Crystal Ball. The grey histogram shows the angles of the generated protons, and the black histogram shows the angles of detected protons with a proton-multiplicity condition of 2, respectively.

Table 5.1: The tracking efficiencies of the fragment-branch detectors using different tolerances.

Tolerance [mm]	GFI#1 [%]	GFI#2 [%]	TFW [%]
14.5	86	88	62
29	95	96	73
100	97	98	84

events have been considered, in which the incoming charge and mass are gated to select ^{20}O, and the FRAGMENT trigger pattern is required.

Since the geometrical centre of the beam does not necessarily coincide with the geometrical centres of the detectors, first the three detectors should be aligned with respect to the beam. For this purpose, the position values of each detector are shifted by an offset that puts the centre of the corresponding position histogram at zero.

After the alignment, a tolerance is defined to check how well the measured positions match the track position. To be strict, the tolerance was first set to the uncertainty in the determination of the track position, which is obtained from folding the position resolutions of TFW and GFI. The position resolution of TFW in S393 is 14.5 mm (see the next subsection). Table 5.1 shows the efficiencies obtained with different tolerances. Three tolerances have been taken into account: 14.5 mm, the position uncertainty of the track caused by the detector resolutions; 29 mm, double the track uncertainty; and 100 mm, the width of a paddle.

The obtained efficiencies are just for the purpose of knowing the behaviour of the detectors in the tracking and analysis, and were not used further in the analysis. The selection criteria applied based on the data of these detectors are used for counting

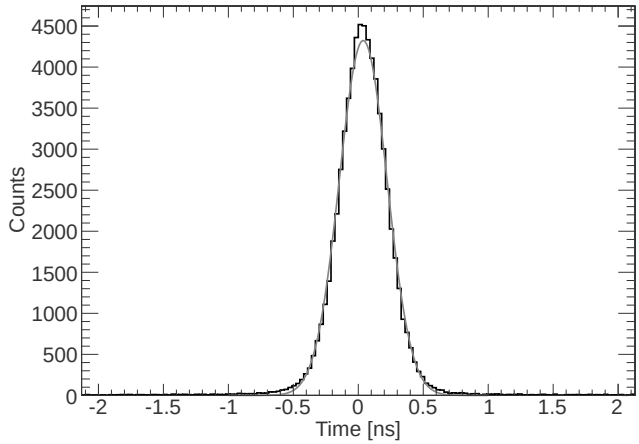

Figure 5.11: The time difference of the horizontal and vertical paddles of TFW. A Gaussian fit gives a width of $\sigma = 0.184$ ns. The FRAGMENT trigger pattern has been required. The statistical error is negligible (around 0.5%).

the number of reactions, and also for counting the number of incoming ions with no reaction. Therefore, these detector efficiencies appear in the denominator as well as the numerator of Equation 5.10, and therefore, are cancelled out.

Time and position resolution of TFW

The position resolution of TFW is determined from its time resolution. In order to determine the time resolution of TFW, the time difference between horizontal and vertical paddles are used. Figure 5.11 shows the spectrum of the time difference under the FRAGMENT trigger pattern. Fitting a Gaussian distribution to the spectrum gives a width of $\sigma = 184$ ps, which results in a time resolution of $184/\sqrt{4} = 92$ ps for TFW. The square root of 4 appears because the values in the histogram of Figure 5.11 are obtained from four individual time measurements; two from the horizontal paddles, and two from the vertical ones.

Having the time resolution, the position resolution of TFW can be obtained easily via

$$\sigma_x = v_{\text{eff}}\,\sigma_t = 158\ (\text{mm/ns}) \times 92 \times 10^{-3}\ (\text{ns}) = 14.5\ \text{mm},$$

where v_{eff} is the effective velocity of light in a TFW paddle, around $0.53\,c$, and is obtained by `Land02` based on the time information of the photomultipliers.

Efficiency of proton detection

In order to obtain the total efficiency for detecting one-proton-knockout events, ϵ_p, we rely on the `R3BRoot` simulation explained in Subsection 5.2.5. This efficiency is obtained as the number of events with a proton multiplicity of 2 divided by the total number of generated events. The proton energies in the Crystal Ball have

been clustered to form proton hits, and the proton multiplicities are determined by the number of proton hits. The total efficiency then becomes $\epsilon_p = 37.4 \pm 0.7\%$. It must be noted that the angular distribution of the simulated protons was determined assuming an isotropic distribution of the scattered nucleons in the centre-of-mass frame, which results in the distribution shown in Figure 5.10 in the laboratory frame (grey histogram). The assumption of isotropic distribution has been verified by comparing the results of the calculations based on this distribution against an equivalent calculation in which the kinematic variables were parametrised based on the proton-proton scattering data. It was shown that up to beam energies of around 500 MeV/u, the assumption of isotropic distribution works well[2]. Therefore, we do not expect a significant systematic uncertainty from this assumption. The obtained efficiency will be applied to the measured yields to obtain the cross sections (see next section).

5.3 Results

In this section, the final results of the analysis of the S393 data are presented. The observations of the bound and unbound excited states of ^{19}N are presented in Subsections 5.3.1 and 5.3.2, respectively. In Subsection 5.3.3, the measured cross sections of the reactions of interest are given along with the theoretical calculations, which then give the quenching factor of the proton states in ^{20}O. Finally, the momentum distributions of the ^{19}N and ^{19}O ions are shown in Subsection 5.3.4.

5.3.1 Bound states of ^{19}N

After a nucleon removal reaction, the reaction residues are often in excited states. If the excited state is below the nucleon separation energy, the nucleus is deexcited by emitting photons; otherwise, it decays by ejecting a nucleon or a cluster of nucleons. Usually, ejection of a nucleon leaves the daughter nucleus in an excited state, which decays to its ground state by emitting photons.

The excited states of the bound reaction fragments can be observed using the prompt photon decay of the ions. Figure 5.12 presents the energy spectrum of the decay photons of ^{19}N detected by the Crystal Ball. A proposed level scheme of ^{19}N from a recent study by Sohler *et al.* [96] is depicted in Figure 5.13. Based on the proposed level scheme, the decay of the first excited state of ^{19}N to the ground state results in the highest intensity photon of 1141 keV. This transition is observed by the Crystal Ball detector at 1126 ± 18 keV, together with the second strongest transition at 574 ± 22 keV.

These two transitions were also observed in another experiment [97] at 529 ± 21 keV and 1137 ± 26 keV. Our observation of the second transition at 574 keV is not in agreement with the previous studies. The disagreement could be due to the con-

[2]Presentation by V. Panin in the Second International Workshop on Quasi-Free Scattering with Radioactive-Ion Beams, September 2013, Azores, Portugal.

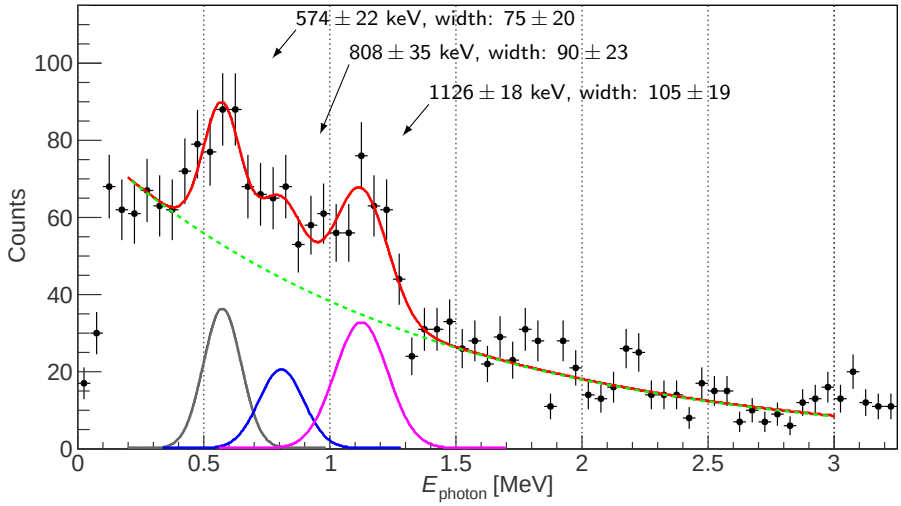

Figure 5.12: Energy spectrum of the decay photons of ^{19}N in the Crystal Ball detector. The strongest and the second to strongest transitions are observed at 1126 keV and 574 keV with widths of $\sigma = 105$ keV and $\sigma = 75$ keV, respectively. The red curve shows the fit of three Gaussian distributions (grey, blue, and cyan) on top of an exponential background (dotted green) to the data points shown as black dots. The widths of the Gaussian functions are not independent, but they are all proportional to one fit parameter, σ_0, that is a measure of the resolution ($\sigma = \sigma_0\sqrt{E}$). The fit gave a reduced chi-squared of $\chi^2/n.d.f. = 1.3$.

tamination from the so-called single escape peak, that is a consequence of the pair production by the 1126 keV photons. This ambiguity could not be resolved due to the poor energy resolution of the Crystal Ball combined with the high level of background.

In addition to the two strongest transitions, a hint of a third peak around 808 ± 35 keV is observed. This transition is not shown in the proposed level scheme of Sohler *et al.*, but it might be a transition from the fourth excited state at 2511 keV to the second state at 1676 keV (see Figure 5.13). Alternatively, we could think of this peak as a result of the Compton scattering of the 1126 keV photons. If a photon is scattered in the backward angles ($\theta_{Compton} \gtrsim 170°$), it escapes the Crystal Ball and its energy is lost, otherwise, its energy is summed up to form a cluster. Therefore, only the photons at the end of the Compton continuum remain, and the rest of the continuum is added back to the main peak. Since the end of the Compton continuum for the 1126 keV photons is at around 917 keV, the scattered photons are expected to form a peak at energies slightly smaller than 917 keV. With the current data, an unambiguous identification of this peak does not seem feasible.

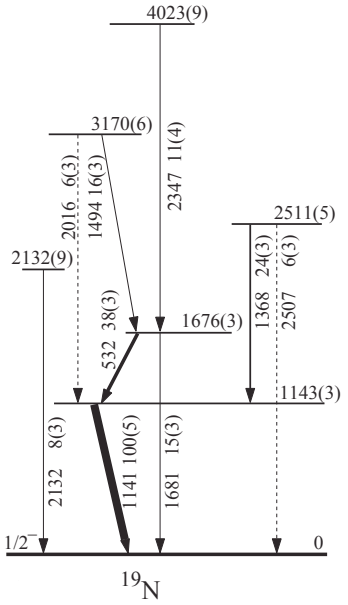

Figure 5.13: Proposed level scheme of ^{19}N by Sohler *et al.* [96]. Excitation energies, their errors and gamma-ray energies are given in keV. Transition intensities of gamma rays and their errors are given in percent where the gamma decay from first excited state to ground state is normalised to 100%.

5.3.2 Unbound states of ^{19}N

In a nuclear reaction, the reaction residues can be excited to energy states above the nucleon separation threshold. For example, when ^{19}N ions are excited to states above one neutron separation energy ($S_n = 5.3$ MeV), they are unbound and emit a neutron. This transition leaves the daughter nucleus, ^{18}N, in a bound state, which in most cases is not the ground state. For the observation of the unbound states, the invariant mass of the decay products should be compared with the rest mass of the mother nucleus (see Equation 5.5). If the daughter nucleus is in an excited state, the subsequent photon decay also should be added to the invariant mass calculation. Therefore, the excitation energy is given by

$$E^\star = \sqrt{\mathcal{P}_\mu \mathcal{P}^\mu} - m_{(^{19}\mathrm{N})} \tag{5.11}$$

$$\mathcal{P} = \mathcal{Q} + \mathcal{R} + \mathcal{S}$$

where $\mathcal{Q}$, $\mathcal{R}$, and $\mathcal{S}$ are the energy-momentum four-vectors of the daughter nucleus, the neutron, and the decay photon, respectively[3], and $m_{(^{19}\mathrm{N})}$ is the rest mass of ^{19}N. $\mathcal{P}_\mu \mathcal{P}^\mu$ denotes the scalar product of $\mathcal{P}$ with itself, which gives its magnitude squared. The four-vector of the daughter nucleus is formed as follows:

$$\mathcal{P} = (E\,,\ p\sin\theta\cos\phi\,,\ p\sin\theta\sin\phi\,,\ p\cos\theta),$$

[3]The four-vector calculations have been performed using the `TLorentzVector` libraries of `ROOT`.

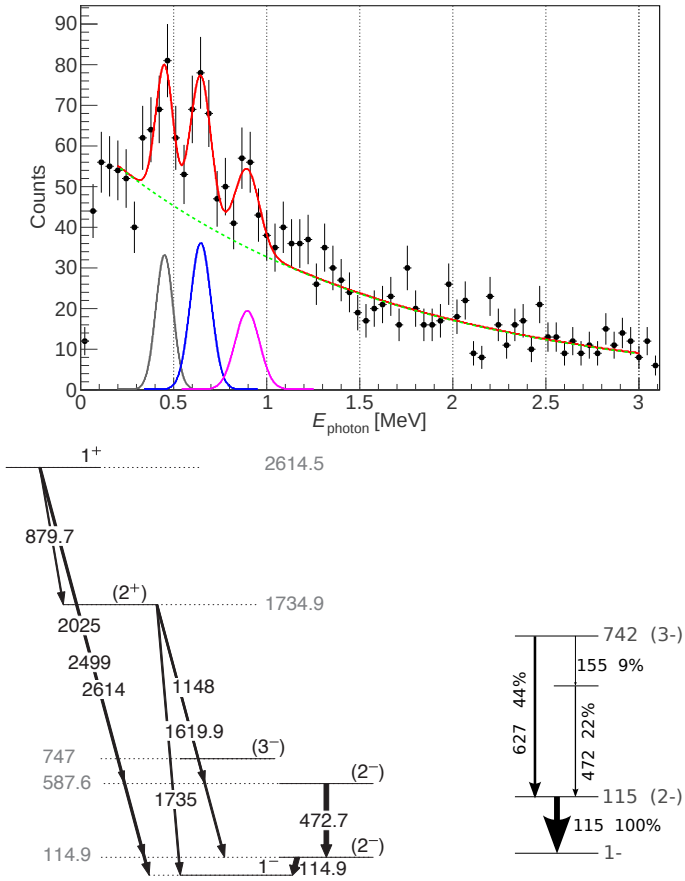

Figure 5.14: The photon spectrum of ^{18}N (top), along with its level scheme (bottom). Three peaks are visible in the spectrum at 452 ± 15 keV, 646 ± 11 keV, and 896 ± 20 keV.

$$p = \frac{m\beta}{\sqrt{1-\beta^2}},$$

where p and E are the total momentum and the total energy of the ion, and the velocity, β, is obtained using the time-of-flight measurement. The angles are determined from the position measurements of the silicon detectors. The four-vectors of the decay neutron and photon are constructed in a similar way, using the LAND and Crystal Ball data for the neutron and photon, respectively.

In order to suppress the background, only the events that have a ^{18}N ion in coincidence with a neutron and a photon are used. The decay neutrons travel almost in the same direction as the daughter nucleus, and therefore, they are mostly detected in LAND. The coincidence with photons was required based on the measured photon spectrum of ^{18}N shown in Figure 5.14, top panel.

Our measured photon spectrum is compared with the suggested level scheme from

the NNDC database[4], lower left panel in Figure 5.14. Three peaks are visible in the spectrum: the first and third peaks at 452 ± 15 keV ($\sigma = 46$ keV) and 896 ± 20 keV ($\sigma = 66$ keV) (shown in grey and cyan) are in agreement with the transitions $2^- \rightarrow 2^-$ and $1^+ \rightarrow 2^+$, respectively. The second peak at 646 ± 11 keV ($\sigma = 56$ keV) (shown in blue) matches a transition of 3^- level to the lower 2^- state. Such a transition has not been indicated in the level scheme from the NNDC database, but it has been observed at 627 keV in a study of the nuclear structure of ^{18}N [98]. Their suggested level scheme is presented at lower right in Figure 5.14.

The obtained excitation energy spectrum is shown in Figure 5.15. The upper and lower panels both show the excitation energy spectra, the upper panel presenting the CH_2-target contribution (black) and the carbon-target contribution (grey) separately before any normalisation, while the lower panel presents the spectrum when the normalised carbon-target contribution is subtracted from that of CH_2. The spectrum in lower panel is illustrated as the yield (count rate normalised to the units of cross section, but before applying the efficiencies) versus excitation energy.

Interestingly, the neutron separation energy of ^{19}N is well reproduced from the CH_2 histogram in the upper panel of Figure 5.15, that gives a minimum excitation energy of 5.8 ± 0.1 MeV. Based on the photon spectrum of ^{18}N, only the photons with an energy larger than $E_{\gamma\text{min}} = E_1 - 3\sigma_1 = 0.3$ MeV were considered, where E_1 and σ_1 are the centroid and width of the first Gaussian function (grey curve in the top panel of Figure 5.14). Taking into account the minimum energy of 0.3 MeV for the decay photons, it gives rise to a neutron separation energy of $5.8 - 0.3 = 5.5$ MeV, which is close to the previously determined value of 5.33 ± 0.03 MeV[5].

Despite the low statistics and large uncertainties, four peaks are visible in the excitation energy spectrum of ^{19}N that could be hints of four unbound excited states decaying via neutron emission. The widths and centroids of the states are determined from the illustrated fit in the lower panel of Figure 5.15, and are given in Table 5.2. The fit function is a sum of four independent Gaussian distributions with varying widths. The fitted mean value of each Gaussian distribution was limited to be within a range of 200 keV from the estimated mean value. In order to verify four independent peaks in this spectrum several different fit functions were tested as other possible hypotheses. For example, fit functions with two or three Gaussian distributions were considered. Although a conventional chi-squared test would not lead to rejection of any of the other considered fit functions, the fit with four Gaussian distributions seems to describe the spectrum better than other alternatives. In future, a more detailed statistical analysis of the excitation-energy spectrum will be carried out, preferably with methods that deal with low statistics better than the chi-squared test.

[4]The level scheme is generated using the RadWare software package (http://radware.phy.ornl.gov/main.html), and is based on the NNDC database, National Nuclear Data Center, Brookhaven National Laboratory, USA (http://www.nndc.bnl.gov/).

[5]NNDC database.

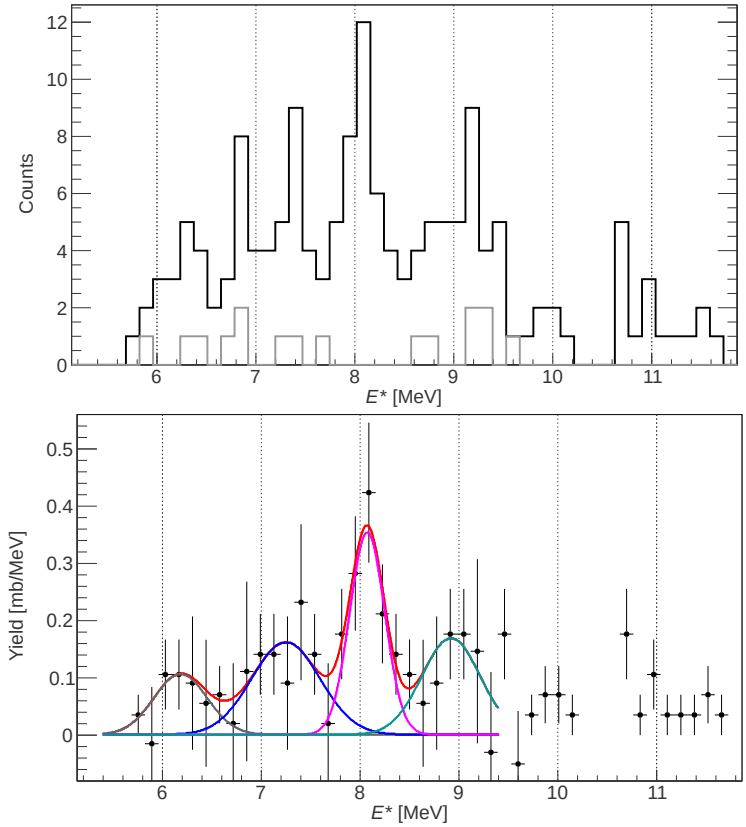

Figure 5.15: Top: The excitation-energy spectra of the unbound ^{19}N ions after a quasi-free knockout from ^{20}O, obtained with CH_2 target (black) and carbon target (grey). Bottom: the normalised spectrum due to hydrogen after subtraction of the spectra in the upper panel. The fitted function (red curve) is a sum of four independent Gaussian distributions (grey, blue, cyan, magenta).

Table 5.2: The four states of ^{19}N above its neutron separation energy. The widths are given as the σ parameter of the Gaussian distributions. The errors are purely statistical, and are given by the fit procedure.

$^{19}N^{\star} \rightarrow {}^{18}N + n +$ photon		
state	centroid [MeV]	width [MeV]
1^{st}	6.2 ± 0.2	0.3 ± 0.2
2^{nd}	7.3 ± 0.2	0.3 ± 0.2
3^{rd}	8.1 ± 0.1	0.2 ± 0.1
4^{th}	8.9 ± 0.2	0.3 ± 0.2

Table 5.3: Normalised yields in millibarns. The stated uncertainties are statistical only.

target	CH_2	carbon	proton
$p(^{20}\mathrm{O}\,,pp^{19}\mathrm{N})$	15.0 ± 0.4	3.1 ± 0.3	5.9 ± 0.5
$p(^{20}\mathrm{O}\,,p^{19}\mathrm{O})n$	82.9 ± 0.9	37.6 ± 0.9	22.7 ± 1.3

5.3.3 Measured and calculated cross sections

The measured yields for the $p(^{20}\mathrm{O}\,,pp^{19}\mathrm{N})$ and $p(^{20}\mathrm{O}\,,p^{19}\mathrm{O})n$ reactions are given in Table 5.3. These yields are integrated over all bound states available to the knock-out residues, ^{19}N and ^{19}O. However, the inclusive cross sections are obtained only after applying the efficiencies and geometrical effects. As was explained at the end of Section 5.2, the total efficiency for detecting two protons in the exit channel of the $p(^{20}\mathrm{O}\,,pp^{19}\mathrm{N})$ reaction is $\epsilon_p = 0.37$. The measured yield and its corresponding uncertainties were divided by this efficiency to obtain an inclusive cross section of

$$15.8 \pm 1.4^{stat} \pm 0.5^{sys}\ \mathrm{mb}$$

for this reaction. The given systematic uncertainty only includes the uncertainty in the thickness of the target, around 3%; therefore, it is a lower limit for the systematic uncertainty. Other sources of systematic uncertainties are the efficiency calculations based on simulations and the criteria applied for selecting the events of interest, but we do not expect them to be significantly larger than the presented systematic uncertainty. A detailed evaluation of the systematic uncertainties is beyond the time limits of this thesis and will not be presented here.

Since the total efficiency for the detection of the neutron-knockout reactions is not evaluated yet, the results for the $p(^{20}\mathrm{O}\,,p^{19}\mathrm{O})n$ reactions in this thesis are presented *without* the efficiency considerations. Therefore, we only report the measured yields, as given in Table 5.3, rather than inclusive cross sections.

Shell model calculations for the cross sections of the two reactions of interest were performed by Carlos Bertulani[6]. The cross sections for removal of a nucleon from each orbital, with their occupation numbers, are given in Table 5.4, summing to a total cross section of 42.81 mb for removal of a proton and 75.95 mb for removal of a neutron from ^{20}O. For these calculations, eikonal scattering wave functions with relativistic corrections were employed. Moreover, the nuclear absorption due to multiple scattering has been implemented in the calculations. Hartree-Fock-Bogoliubov calculations with SLy4 interaction were used to obtain the densities of ^{19}N and ^{20}O. The proton and neutron separation energies from ^{20}O were assumed to be 19.34 MeV and 7.6 MeV, respectively. The other separation energies for bound levels were taken from estimates using the Woods-Saxon potential, in which the separation energy of the last orbital is reproduced.

Using Equation 2.3, we obtain the quenching factor for the proton states in ^{20}O to be:

$$R = \frac{15.8}{42.81} = 0.37 \pm 0.03^{stat} \pm 0.01^{sys}.$$

[6]Private communication.

Table 5.4: Theoretical cross sections of the proton and neutron removal from different states of ^{20}O. A spectroscopic factor of 1 has been assumed in the calculations.

j	l	occupancy number	cross section [mb]
proton removal			
0.5	1	2	11.46
1.5	1	4	22.54
0.5	0	2	8.81
Total			42.81
neutron removal			
2.5	2	4	30.21
0.5	1	2	12.27
1.5	1	4	24.48
0.5	0	2	8.98
Total			75.95

The difference between the proton and neutron separation energies for ^{20}O is

$$\Delta S = S_p - S_n = 19.35 - 7.61 = 11.7 \text{ MeV}.$$

Therefore, the dependence of the obtained quenching factor, R, on ΔS appears as depicted in Figure 5.16, which seems to be in agreement with the general trend. It is worth mentioning that the observed quenching factor is integrated over a few states, and only gives an account of the total quenching of all the states below the nucleon separation energy. However, this result confirms the extra quenching of the deeply-bound proton states in neutron-rich ^{20}O, as compared to stable ^{16}O ions.

5.3.4 Momentum distributions

In a nucleon removal reaction, the momentum distribution of the nucleon after the reaction is characteristic of the single-particle state from which the nucleon is removed. For example, if the nucleon is knocked out of an s state, its momentum distribution would be different than when it is knocked out of a p or a d state.

After selection of the reaction of interest, the mass and velocity of each reaction fragment are used to calculate its momentum. The mass and velocity are obtained from the tracking procedure explained in Section 4.6. Then, the angular information from the silicon strip detectors (SSD#3 and SSD#4) are used to determine the transverse and longitudinal momenta, p_x, p_y, and p_z.

The momentum resolution of the setup combined with the straggling of the beam was determined using the data with no reaction. Figure 5.17 shows the p_x, p_y, and p_z distributions of the ^{20}O ions in the CH_2-target data. The criteria for selection of the events in these histograms ensure a minimum probability of any reaction.

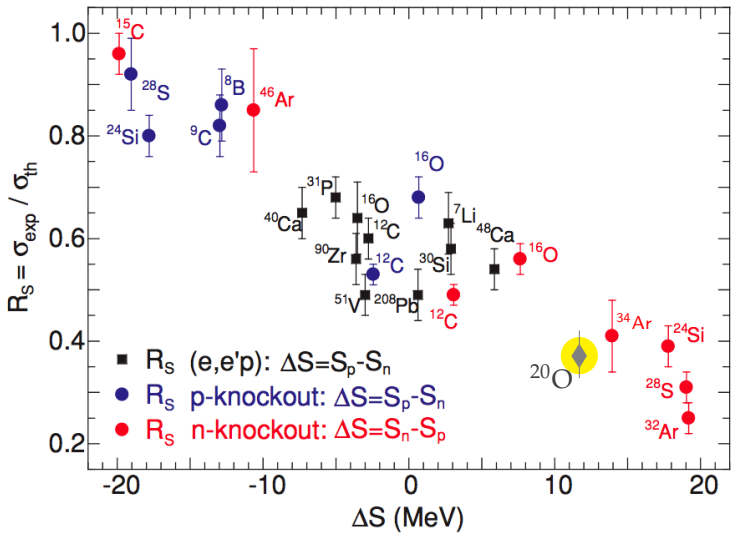

Figure 5.16: The same as Figure 2.1, but with our quenching factor included as the grey diamond. The yellow circle is just to guide the eyes. The shown error bar indicates a lower limit of the possible uncertainties.

Therefore, the width of these histograms is a combination of the momentum resolution of the setup, the momentum spread of the incoming beam, and the straggling of the beam in the materials in the beam path. Fits of Gaussian distributions (grey curves) to the histograms result in the following widths:

$$\begin{aligned} \sigma_{px} &= 42.8 \pm 0.1 \text{ MeV}/c, \\ \sigma_{py} &= 70.5 \pm 0.1 \text{ MeV}/c, \\ \sigma_{pz} &= 65.3 \pm 0.1 \text{ MeV}/c, \end{aligned} \tag{5.12}$$

giving rise to a total momentum width of $\sigma_{pf} = 105.2$ MeV$/c$ for the outgoing beam. The momentum spread of the incoming beam is $\sigma_{pi} = 32.6$ MeV$/c$.

It can be seen from Figure 5.17 that the p_y distribution does not follow a Gaussian shape as is the case for p_x, and also it is wider than the p_x distribution. This difference is due to the fact that the setup provides more information in the horizontal than in the vertical direction, and thus the momenta in x direction are better determined.

Figures 5.18 and 5.19 show the transverse and longitudinal momentum distributions of ^{19}N and ^{19}O in the $p(^{20}\text{O}\ ,\ pp^{19}\text{N})$ and $p(^{20}\text{O}\ ,\ p^{19}\text{O})n$ reactions, respectively. Upper, middle and lower rows present p_x, p_y, and p_z, respectively. The solid black histograms show the momentum distributions for the CH_2-target data, and the dashed grey ones for the carbon-target data. The right columns show the background-subtracted momentum distributions. In order to obtain the spectra in the right column, the corresponding histograms from the CH_2- and carbon-target data are first normalised to the luminosities of the corresponding experimental runs.

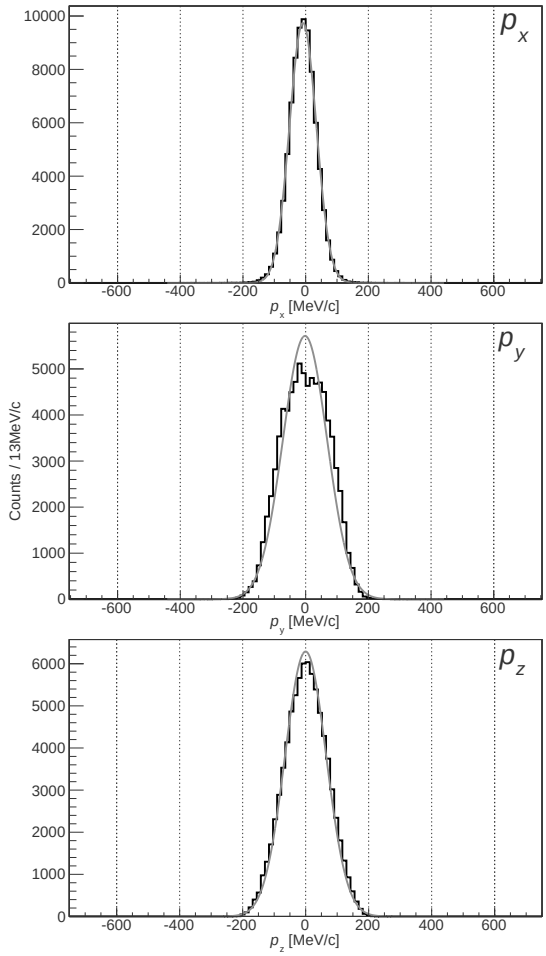

Figure 5.17: Momentum distribution of the ^{20}O ions in the CH_2-target data for events in which no reaction has taken place. The events in these histograms satisfy the FRAGMENT trigger pattern, and also the outgoing beam has been gated on ^{20}O.

Next, the histogram from carbon data is subtracted from the CH_2-data histogram, and then the resulting histogram is scaled by half (see Equations 5.7 and 5.9). Finally, the output is scaled again to account for the efficiencies and also to normalise for the bin widths. The efficiencies are only applied for the proton-knockout data in Figure 5.18. All momentum distributions are presented in the rest frame of the projectile, and the longitudinal distribution is shifted to zero to correct for the small recoil momentum.

Gaussian distributions are fitted to the momentum spectra (shown as red curve) in order to obtain the widths of the distributions. The fit parameters are given in Table 5.5. Although it is expected that the p_x and p_y distributions peak at zero, their centres slightly deviate from zero. Taking into account that the uncertainties in Ta-

Table 5.5: The centroids (mean value) and widths (σ) of the momentum distributions shown in Figures 5.18 and 5.19. σ_0s are the widths obtained from the Gaussian fits. σ_1s are the widths after subtraction of the resolutions given in Equation 5.12. The theory does not reproduce the experimental results.

distribution	centroid [MeV/c]	σ_0 [MeV/c]	σ_1 [MeV/c]	theory
^{19}N				
p_x	-13 ± 5	108 ± 4	99	
p_y	-5 ± 5	126 ± 4	100	114.9
p_z	0*	159 ± 5	124	98.7
^{19}O				
p_x	-6 ± 3	121 ± 3	113	
p_y	5 ± 3	129 ± 3	105	112.5
p_z	0*	176 ± 4	145	87.1

*Manually forced to zero.

ble 5.5 are merely statistical, it is clear that the centres of the p_x and p_y distributions are determined with less precision than given in Table 5.5. Therefore, if the systematic uncertainties are determined and included, the deviation will be within the accepted certainty interval, namely that they will agree will the value of zero.

The blue curves in Figures 5.18 and 5.19 represent the theoretical calculations of the momentum distributions[7], that are scaled to match the height of the experimental data. The fit to the experimental data appears to be slightly wider than the theoretical calculations, which is due to the fact that the experimental distributions contain the resolution of the detection setup. If the resolutions given in Equation 5.12 are subtracted from the widths of the experimental momentum distributions, they would be narrower than the theoretical ones. Besides, in the theoretical calculations, the transverse distributions are wider than the longitudinal ones, while in our measurements, it is the other way around. With these ambiguities, no conclusion can be drawn from the momentum distributions. Therefore, more analysis and theoretical studies are required to understand the momentum distributions better.

[7]Carlos Bertulani: Private communications.

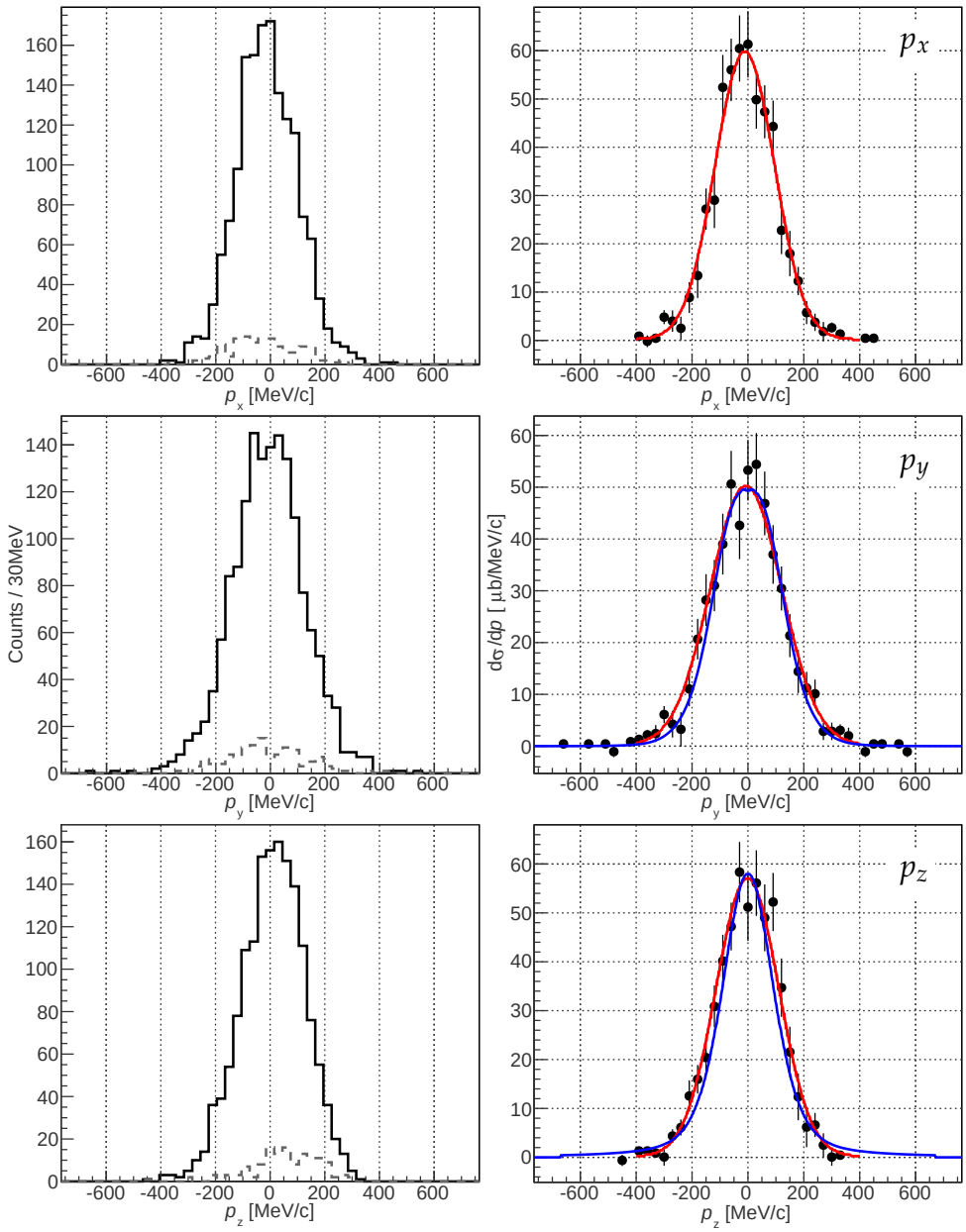

Figure 5.18: Reconstructed momentum distributions of ^{19}N from the $p(^{20}\mathrm{O}\ ,\ pp^{19}\mathrm{N})$ reaction. Upper, middle and lower rows represent the x, y, and z components of the reconstructed momentum (p_x, p_y, and p_z), respectively. In the left column, the solid black line shows the momentum distribution for the CH_2-target data, and the dashed grey line for the carbon-target data. The right column shows the background-subtracted momentum distributions. The errors are propagated accordingly. The red curves show Gaussian distributions fitted to the spectra, and the blue ones are the theoretical calculations normalised to the data.

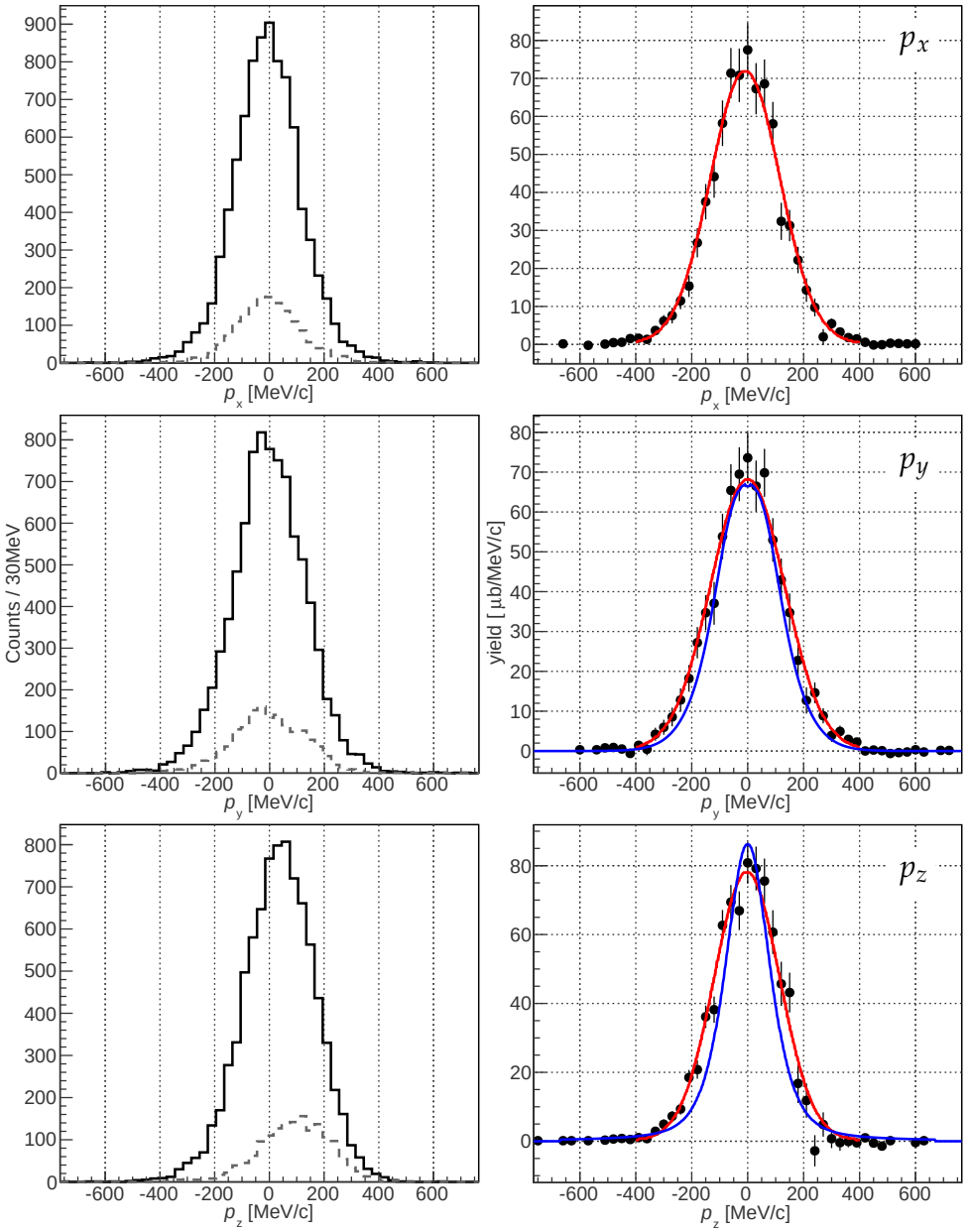

Figure 5.19: Same as Figure 5.18 but for the $p(^{20}\mathrm{O}\,,\,^{19}\mathrm{O})n$ reaction.

Chapter

Summary and outlook

A-century-long history of nuclear physics has given rise to the establishment of a rather unambiguous picture of the atomic nuclei found in nature; and yet, exotic features appear in unstable nuclei, specially in nuclei near or at drip lines. EXL and R^3B, parts of the future FAIR facility, are two major projects for extensive investigations of the unstable nuclei. EXL will mainly focus on the light-ion induced reactions in inverse kinematic performed in a storage ring. A particular feature of the envisaged EXL setup is the possibility of the detection of reactions with very low momentum transfer. R^3B will be able to study reactions with external beams of light to heavy nuclei, and its envisaged detection setup is designed to detect all the reaction products and fragments. R^3B will be more suitable for the high-momentum-transfer reactions, and hence, it is complementary to the EXL project.

The studies presented in the current thesis are composed of two independent parts. The first one, explained in Chapter 3, was a test of the response of a few detection units of the future EXL setup. The second part, which is the major part of this thesis, was an experimental study of the quasi-free reactions of ^{20}O within the LAND-R^3B campaign. LAND-R^3B is a predecessor of the future R^3B project. The experimental setup and the data calibration were explained in Chapter 4, and the results were presented in Chapter 5 with simulations for the evaluation of the efficiencies.

EXL demonstrator test

The foreseen detection system of the EXL project is an ambitious and sophisticated combination of a few thousand detection units, and requires many comprehensive tests and new developments. As a part of a large number of tests, a small module of the foreseen setup was prepared and tested at the accelerator facility of KVI, Groningen. This module, called the EXL demonstrator, contained two double-sided silicon detectors (DSSDs) and two lithium-drifted silicon detectors (Si(Li)s) located in between the DSSDs. All the silicon detectors were placed inside a vacuum chamber. In addition, two CsI scintillators were placed behind the vacuum chamber.

The EXL demonstrator was irradiated by a beam of protons in order to measure the response of each detector, and to reconstruct the initial beam energy from the sum of the energy signals of each detector. The energy spectra of the silicon detectors were calibrated using radioactive alpha-emitting sources, but in order to calibrate the CsI scintillators, `Geant4` simulations were used. The large uncertainty in the energy of the incident beam caused an ambiguity in the energy calibration of the CsI scintillators. More importantly, the leakage of the scintillation photons from one CsI scintillator to the other one (see Figure 3.9) increased the ambiguities. As presented in Subsection 3.3.4, the total energy reconstruction in the EXL demonstrator test depends on the way the scintillator energies are summed up.

With all the ambiguities, a total energy reconstruction of the demonstrator gave rise to an energy resolution that is already good enough for distinguishing a few of the reactions of interest in the EXL project. However, for most of the reactions the resolution has to be improved. For instance, assume that the ^{136}Xe(p , p') reaction with an excitation energy of $E^{\star} = 15$ MeV is going to be studied with the current demonstrator at scattering angles around 60 degrees (in laboratory frame). In such an experiment, to resolve two states with 300 keV energy difference, the current resolution has to be improved by a factor of two. As a result, it is necessary to either prevent the light from leaking between the calorimeter scintillators, or develop a method to correct for it.

Quasi-free nucleon knockout reactions of ^{20}O in S393 experiment

Independent-particle models have described many properties of the atomic nuclei, but their predictions of the nucleon removal cross sections are systematically higher than the experimental results. This observation has been interpreted as the fragmentation of the nucleon wave function among a few different single-particle states due to the nuclear correlations that are not taken into account in the independent-particle models. The nuclear spectroscopic factors were introduced in order to give an account of the occupancy of nucleon states (see Equation 2.1). Experimentally, quenching of the spectroscopic factors are obtained as the ratio of the measured cross section to the theoretical one (see Equation 2.3). By comparing the quenching factors determined from experimental cross sections, with the spectroscopic factors from the theoretical calculations, it is possible to quantify the strength of the correlations that are missing in the considered models.

It has been shown that the quenching of the spectroscopic factors of a nucleon depends on its binding energy; the deeper a nucleon state is bound, the more its spectroscopic factor is quenched. Although, this trend has been observed in the results of different experiments (see Figure 2.1), a systematic study that includes all isotopes of one element is still missing. Based on this motivation and along with the physics goals of the R^{3}B project, the S393 experiment has been performed to study this concept for oxygen isotopes with the LAND-R^{3}B setup.

The LAND-R^{3}B setup comprised three main parts: the detectors before the target that are mainly for identification of the incoming ion beams (Section 4.2), the detectors around the target that are aimed at the detection of the knocked-out protons

as well as the decay photons (Section 4.3), and the detectors after the target that detect the reaction fragments, the outgoing beam, the decay neutrons, and even the protons that travel in forward direction (Section 4.4). The calibration procedure for most of the detectors includes matching the gains and synchronising the time signals of their multiple readout channels.

The charge of the incoming ions were reconstructed using their energy-loss information, and their mass was obtained by using their time of flight combined with their magnetic rigidity. Identification of the outgoing beam and fragments is based on the same principles, but the technical procedure was not as straightforward. A tracking programme was developed for determining the optimum mass of the outgoing fragments using the kinematic measurements as well as the field maps of the magnet to fit a trajectory to the measured positions of each ion. The fit procedure varies the mass of the ions and strives at determining a trajectory which has minimum deviation from the measured positions of ions (Section 4.6). With the ion mass reconstructed with the fit, and energy loss measured in SSD#3 and TFW, the outgoing ions are identified unambiguously.

With identification of the incoming and outgoing ions, the one-nucleon-removal reactions from ^{20}O were selected. In order to ensure a clean selection of the quasi-free reactions, the angular correlations and some other conditions were applied (Section 5.1).

In order to find out what states of ^{19}N are populated in the quasi-free reactions, the excitation-energy spectra of ^{19}N of bound and unbound states were studied separately. Figure 5.12 presents the decay photon spectrum of ^{19}N, which shows two bound excited states. In addition, a hint of a third peak was observed which could be a third transition or a Compton edge. For observation of the unbound states, the excitation-energy spectrum of the ^{19}N ions were calculated using the invariant mass of the reaction products. A preliminary statistical analysis shows that the spectrum can be described by four independent Gaussian distributions, as illustrated in Figure 5.15. The centroids and the widths of these states are given in Table 5.2. Given the low statistics in the spectrum, a strong statement on the observation of unbound states of ^{19}N cannot be made. However, if the illustrated fit will stand more detailed analysis, it will be the first time, to the best of our knowledge that unbound states of ^{19}N have been observed in an experimental study.

One of the main goals of the measurement was to obtain the inclusive cross section to be used for determining the quenching of the spectroscopic factors. No selection was applied on the populated states of the reaction fragments; therefore, the obtained cross sections are inclusive of all bound states of the reaction fragments. The measured yields of the $p(^{20}\mathrm{O}\,,\,pp^{19}\mathrm{N})$ and $p(^{20}\mathrm{O}\,,\,p^{19}\mathrm{O})n$ reactions are

$$\begin{aligned} p(^{20}\mathrm{O}\,,\,pp^{19}\mathrm{N}): &\quad 5.9 \pm 0.5, \\ p(^{20}\mathrm{O}\,,\,p^{19}\mathrm{O})n: &\quad 22.7 \pm 1.3. \end{aligned}$$

The total efficiency for detecting the proton-knockout reaction is $\epsilon_p = 0.37$. Applying this efficiency to the measured yield of the reaction results in a cross section of $15.8 \pm 1.4^{stat} \pm 0.5^{sys}$ mb. The theoretical calculation of this cross section gives

$\sigma_{th} = 42.81$ mb, which is used to determine a reduction factor of

$$R = \frac{15.8}{42.81} = 0.37 \pm 0.03^{stat} \pm 0.01^{sys},$$

for the spectroscopic factors of the proton states in ^{20}O. The stated systematic uncertainties include only the uncertainty in the thickness of the target, and therefore, is the lower limit of the systematic uncertainties.

To further improve this study, the total efficiency of detecting the neutron-knockout reactions should be determined. Having this efficiency, it will be possible to determine the inclusive cross section of the $p(^{20}\mathrm{O}\,,\,p^{19}\mathrm{O})n$ reaction, and therefore, obtain the reduction of the spectroscopic factors of neutron states in ^{20}O.

Finally, the momentum distributions of ^{19}N and ^{19}O produced in the $p(^{20}\mathrm{O}\,,\,pp^{19}\mathrm{N})$ and $p(^{20}\mathrm{O}\,,\,p^{19}\mathrm{O})n$ reactions were presented in Figures 5.18 and 5.19, respectively. The general shape of the theoretical calculations and the measured distributions agree reasonably well. Nevertheless, further analysis of the experimental resolutions is necessary in order to verify our understanding of the momentum distributions. After understanding the discrepancies between the measured and calculated momentum distributions, it will be possible to use them to disentangle the contributions of the s and p states in the considered reactions. For this purpose the theoretical momentum distributions of the s and p states should be compared with the experimental distributions.

Nederlandse Samenvatting

Dit proefschrift beschrijft twee onafhankelijke studies. Het eerste onderwerp, wordt behandeld in hoofdstuk 3. Het gaat om het testen van de respons van enige detectie-elementen voor de toekomstige EXL opstelling. Het tweede deel, tevens het grootste deel van dit proefschrift, is een experimentele studie van de quasi-vrije reacties van ^{20}O binnen de LAND-R^{3}B campagne. De experimentele opstelling en de kalibratie procedure van de gegevens worden in hoofdstuk 4 toegelicht, en de resultaten worden gepresenteerd in hoofdstuk 5 te samen met simulaties voor de berekening van de efficiëntie.

EXL demonstrator test

Een kleine module van de geplande opstelling van EXL werd getest op de versneller faciliteit KVI, Groningen. Deze module, genaamd de EXL demonstrator, bevatte twee dubbelzijdige siliciumdetectoren (DSSDs) en twee "lithium-drifted" siliciumdetectoren (Si(Li)s) geplaastst tussen de DSSDs. Daarnaast werden twee CsI scintillatoren geplaatst. De EXL demonstrator werd bestraald met een protonenbundel om de respons van elke detector te meten, en de totale bundelenergie te reconstrueren uit de som van de energiesignalen van elke detector. De onnauwkeurigheden in de energie van de invallende bundel veroorzaakten hierbij een ambiguïteit in de energiekalibratie van de CsI scintillatoren. Belangrijk is dat de lekkage van de scintillatiefotonen van één CsI scintillator naar de andere (zie Figuur 3.9) de ambiguïteiten verhoogde. Ondanks alle ambiguïteiten, heeft een totale energiereconstructie van de demonstrator geleid tot een energieresolutie die al goed genoeg is voor het onderscheiden van een paar van de reacties van belang in het EXL project. Voor de meeste van de reacties zal de resolutie verbeterd moeten worden.

Quasi-vrije nucleonuitstootreacties van ^{20}O in het S393 experiment

Individuele-deeltjesschillenmodellen beschrijven vele eigenschappen van atoomkernen, maar hun voorspellingen van werkzame doorsneden van de nucleonuit-

stootreactie zijn systematisch hoger dan de experimentele waarden. Deze waarneming kan worden uitgelegd als het spreiden van de nucleongolffunctie in een paar verschillende ééndeeltjestoestanden, wat resulteert in de reductie van de spectroscopische factoren. Het is aangetoond dat de reductie van de spectroscopische factoren van een nucleon afhankelijk is van de bindingsenergie: hoe dieper een nucleontoestand gebonden is, hoe meer de spectroscopische factoren gereduceerd worden. Hoewel deze trend in de resultaten van de verschillende experimenten is waargenomen (zie Figuur 2.1), mist er nog een systematische studie die alle isotopen van een element bevat. Naar aanleiding hiervan, is het S393 experiment uitgevoerd om dit voor zuurstof isotopen te bestuderen met de LAND-R^{3}B opstelling (zie hoofdstuk 4).

Om te weten te komen welke toestanden van ^{19}N bezet worden in de quasi-vrije reacties, werden de excitatie-energiespectra van gebonden en ongebonden ^{19}N apart bestudeerd. Figuur 5.12 toont het vervalfotonenspectrum van ^{19}N, waarbij twee gebonden toestanden worden getoond. Bij waarneming van de ongebonden toestanden werden de excitatie-energiespectra van de ^{19}N-ionen berekend met behulp van de invariante massa van de reactieproducten. Uit een preliminaire statistische analyse blijkt dat het spectrum kan worden beschreven door vier onafhankelijke Gaussische verdelingen, zie Figuur 5.15.

Een belangrijke doelstelling van het S393 experiment was het meten van de inclusieve werkzame doorsnede om de reductie van de spectroscopische factoren te verkrijgen. Er werd geen selectie toegepast op de bezette toestanden van de reactiefragmenten. Daarom bevatten de verkregen werkzame doorsneden alle gebonden toestanden van de reactiefragmenten. De gemeten *opbrengst* (*yield*) van de $p(^{20}\mathrm{O}\,, pp^{19}\mathrm{N})$ en $p(^{20}\mathrm{O}\,, p^{19}\mathrm{O})n$ reacties zijn

$$\begin{aligned} p(^{20}\mathrm{O}\,, pp^{19}\mathrm{N}): &\quad 5.9 \pm 0.5, \\ p(^{20}\mathrm{O}\,, p^{19}\mathrm{O})n: &\quad 22.7 \pm 1.3. \end{aligned}$$

De totale efficiëntie van de detectie van de protonuitstootreactie is $\epsilon_p = 0.37$. Toepassing van deze efficiëntie leidt tot een werkzame doorsnede van $15.8 \pm 1.4^{stat} \pm 0.5^{sys}$ mb. De theoretische berekening van de werkzame doorsnede geeft $\sigma_{th} = 42.8$ mb, dit wordt gebruikt om een reductiefactor te bepalen

$$R = \frac{15.8}{42.8} = 0.37 \pm 0.03^{stat} \pm 0.01^{sys},$$

voor de spectroscopische factoren van de protontoestanden in ^{20}O. De aangegeven systematische fout bevat alleen de onzekerheid in de dikte van het trefplat. Tenslotte zijn de impulsverdelingen van ^{19}N en ^{19}O in de $p(^{20}\mathrm{O}\,, pp^{19}\mathrm{N})$ en $p(^{20}\mathrm{O}\,, p^{19}\mathrm{O})n$ reacties bepaald, deze worden respectievelijk in Figuren 5.18 en 5.19 getoond. De algemene vorm van de theoretische en de gemeten verdelingen komen redelijk met elkaar overeen. Niettemin is verdere analyse van de experimentele resoluties noodzakelijk; dit om de impulsverdelingen beter te kunnen begrijpen.

Acknowledgements

Though only my name appears on the cover, many other people have contributed to this dissertation, to whom I dedicate the following humble words.

First of all, I would like to express my earnest gratitude to Prof. dr. Nasser Kalantar who welcomed me in his group and supported me during the course of my Ph.D. His immense patience, constructive criticism, and valuable supervision helped to find my own way, and his high standards pushed me to work efficiently on my projects.

My daily supervisor Dr. Catherine Rigollet has been always a source of motivation and useful advise. She has been the first one to read my writings, and to comment on my mistakes patiently. I am deeply grateful for everything she has done for me.

I am extremely indebted to Dr. Masoud Mahjour-Shafiei for his supervision not only during the last year of my Ph.D., but also during my M.Sc project. During my M.Sc. project, he mentored me as a beginner in nuclear physics, and guided me toward pursuit of a Ph.D. Also during the last year of my Ph.D., when I was struggling with the final steps of analysis, he came to my support with a positive attitude and keen sense of analysis.

Furthermore, I would like to acknowledge and thank the reading committee of my thesis: I had the honour of several meetings with Prof. dr. Muhsin N. Harakeh, who read my thesis carefully and helped me to understand the less clear ideas. The gravity of his knowledge has always been an inspiration to me. Prof. dr. Thomas Aumann, welcomed me in the LAND-R^{3}B collaboration. I always admired his deep insight in both theoretical and experimental problems and enjoyed his guidance during the meetings and seminars. My thesis was significantly improved by the careful reading and detailed comments of Prof. dr. Remco Zegers. I am very much thankful for the time he spent for my thesis.

My friends and colleagues in the LAND-R^{3}B collaboration have been greatly generous by offering programmes, calibration data, and useful advise. Specially, I am grateful to Dr. Ralf Plag who provided the tracking programme and was a great source of technical information, Paloma Diaz Fernandez with whom I had many fruitful discussions and helped me with my simulations, and also many others who helped me in different ways: Dr. Valerii Panin, Marcel Heine, Ronja Thies, Dr. Haakan Johannson, Alina Movsesyan,

Matthias Holl, Dr. Christoph Ceasar, and Dr. Christoph Langer.

My sincere thanks go to the Nuclear and Hadron Physics group of KVI, from whom I learned a lot in our weekly meetings and friendly discussions. Specially, I am grateful to Mohammad Babai, whose rich programming skills and computer expertise were freely available, and also corrected the Dutch summary of this thesis. Moreover, I thank Wouter Dekens who helped me in writing the Dutch summary. Also, I am thankful for the help and support of my colleagues in the EXL collaboration; Mirko von Schmid, Dr. Brano Streicher, Dr. Tania Illieva, Dr. Oleg Kieselev, Prof. dr. Peter Egelhof, and Dr. Manfred Mutterer.

I appreciate the company of my great friends in Groningen who made my years of Ph.D. unforgettable: Qader, Ali, Ganesh, Olga, Olena, Soumya, Manisha, Hossein, Mohammad Babai, Johan, Saeedeh, Oksana, Myroslav, Elmaddin, Mehdi, Parisa, Ayan, Ola, Roxana, Wouter, Zahra, David, Ruud, Sybren, Santosh, Gianluca, and Mohammad Eslami. I can hardly ever exaggerate the value of friends like Qader and Ali, who have always been supportive, encouraging, and full of dexterous (sometimes wicked ت) surprises. Moreover, Qader was a great source of statistics knowledge.

I am blessed to have an incredible family. No words can truly express my appreciation of the significance of all they have done for me. I dedicate this thesis to them:

تقدیم به پدرم که مرا به همت بلند سفارش نمود، و مادرم که مرا بردباری آموخت.

تقدیم به برادرانم که مرا پشت و پناه‌اند، و خواهرم که سرچشمه‌ی نشاط است.

❊

محمدعلی نجفی

آذر ۱۳۹۲

Mohammad Ali Najafi

November 2013

Abbreviations

AGATA	**A**dvanced **GA**mma **T**tracking **A**rray
ALADIN	**A LA**rge **DI**pole mag**N**et
CALIFA	**CAL**orimeter for **I**n-**F**light gamm**A** detection
DESPEC	**DE**cay **SPEC**troscopy
DTF	**D**icke **T**O**F** wand
DSSD	**D**ouble-sided **S**ilicon **S**trip **D**etector
EGPA	**E**XL **G**amma and **P**article **A**rray
ELISe	**EL**ectron-**I**on **S**catt**e**ring in a storage ring
ESPA	**E**XL **S**ilicon **P**article **A**rray
EXL	**EX**otic nuclei studied in **L**ight ion induced reactions
FAIR	**F**acility for **A**ntiproton and **I**on **R**esearch
FRS	**FR**agment **S**eparator
GFI	**G**rosse **FI**ber scintillator
GSI	**G**esellschaft für **S**chwer**I**onenforschung
HISPEC	**HI**gh-resolution **SPEC**troscopy
ILIMA	**I**someric beams, **LI**fetimes and **MA**sses
ISOL	**I**sotope **S**eparation **O**n-**L**ine
LAND	**L**arge **A**rea **N**eutron **D**etector
LaSpec	**La**ser **Spec**troscopy
MATS	Precision **M**easurements of very short-lived nuclei with **A**dvanced **T**rapping **S**ystem
NUSTAR	**NU**clear **ST**ructure, **A**strophysics and **R**eactions
PCB	**P**rinted **C**ircuit **B**oard
PDC	**P**roton **D**rift **C**hamber
POS	**PO**sition-sensitive **S**cintillator

PSP	**P**osition-**S**ensitive pin **D**iode
QDC	**Charge**-to-**D**igital **C**onverter
R^{3}B	**R**eactions with **R**elativistic **R**adioactive **B**eams
ROLU	**R**echts, **O**ben, **L**inks, **U**nten
SIS	**S**chwer**I**onen**S**ynchrotron
SSD	**S**ilicon **S**trip **D**etector
Super-FRS	**Super FR**agment **S**eparator
TDC	**T**ime-to-**D**igital **C**onvertor
TFW	**T**ime-of-**F**light **W**all

Bibliography

[1] Pandharipande V. R., Sick I. & deWitt Huberts P. K. A. Independent particle motion and correlations in fermion systems. *Reviews of Modern Physics* **69**, 981 – 992 (1997). URL http://link.aps.org/doi/10.1103/RevModPhys.69.981.

[2] Townes C. H., Foley H. M. & Low W. Nuclear quadrupole moments and nuclear shell structure. *Physical Review* **76**, 1415 – 1416 (1949). URL http://link.aps.org/doi/10.1103/PhysRev.76.1415.

[3] Caurier E., Martínez-Pinedo G., Nowacki F., Poves A. & Zuker A. P. The shell model as a unified view of nuclear structure. *Reviews of Modern Physics* **77**, 427 – 488 (2005). URL http://link.aps.org/doi/10.1103/RevModPhys.77.427.

[4] Woods R. D. & Saxon D. S. Diffuse surface optical model for nucleon-nuclei scattering. *Physical Review* **95**, 577 – 578 (1954). URL http://link.aps.org/doi/10.1103/PhysRev.95.577.

[5] Cohen S. & Kurath D. Effective interations for the 1p shell. *Nuclear Physics* **73**, 1 – 24 (1965). URL http://www.sciencedirect.com/science/article/pii/0029558265901483.

[6] Decharge J. & Gogny D. Hartree-Fock-Bogolyubov calculations with the D1 effective interaction on spherical nuclei. *Physical Review C* **21**, 1568 – 1593 (1980). URL http://link.aps.org/doi/10.1103/PhysRevC.21.1568.

[7] Negele J. The mean-filed theory of nuclear structure and dynamics. *Reviews of Modern Physics* **54**, 913 – 1015 (1982). URL http://link.aps.org/doi/10.1103/RevModPhys.54.913.

[8] Dean D., Engeland T., Hjorth-Jensen M. *et al.* Effective interactions and the nuclear shell-model. *Progress in Particle and Nuclear Physics* **53**, 419 – 500 (2004). URL http://www.sciencedirect.com/science/article/pii/S0146641004000912.

[9] Mougey J. The (e,e'p) reaction. *Nuclear Physics A* **335**, 35 – 53 (1980). URL http://www.sciencedirect.com/science/article/pii/0375947480901657.

[10] Dickhoff W. H. Determining and calculating spectroscopic factors from stable nuclei to the drip lines. *Journal of Physics G: Nuclear and Particle Physics* **37**, 064007 (2010). URL http://stacks.iop.org/0954-3899/37/i=6/a=064007.

[11] Barbieri C. Role of long-range correlations in the quenching of spectroscopic factors. *Physical Review Letters* **103**, 202502 (2009). URL http://link.aps.org/doi/10.1103/PhysRevLett.103.202502.

[12] Dickhoff W. & Barbieri C. Self-consistent green's function method for nuclei and nuclear matter. *Progress in Particle and Nuclear Physics* **52**, 377 – 496 (2004). URL http://www.sciencedirect.com/science/article/pii/S0146641004000535.

[13] Kofoed-Hansen O. The birth of on-line isotope separation. In *Proceedings of 3rd International Conference on Nuclei Far from Stability* (Cargse, France, 1976). URL http://cds.cern.ch/record/286626/.

[14] Cornell J. C. Radioactive beam facilities in europe: current status and future development. In *17th International Conference on Cyclotrons and their Applications* (Tokyo, Japan, 2004). URL http://arxiv.org/abs/nucl-ex/0501030v1.

[15] Erler J., Birge N., Kortelainen M. *et al.* The limits of the nuclear landscape. *Nature* 509 – 512 (2012). URL http://www.nature.com/nature/journal/v486/n7404/full/nature11188.html.

[16] Thoennessen M. Current status and future potential of nuclide discoveries. *Reports on Progress in Physics* **76**, 056301 (2013). URL http://stacks.iop.org/0034-4885/76/i=5/a=056301.

[17] Lindroos M. Review of ISOL-type radioactive beam facilities. In *Proceedings of EPAC* (Lucerne, Switzerland, 2004). URL http://accelconf.web.cern.ch/accelconf/e04/PAPERS/TUXCH01.PDF.

[18] Morrissey D. J. & Sherrill B. M. Radioactive nuclear beam facilities based on projectile fragmentation. *Philosophical Transactions of the Royal Society of London A* **356**, 1985–2006 (1998). URL http://rsta.royalsocietypublishing.org/content/356/1744/1985.abstract.

[19] Conceptual Design Report of An International Accelerator Facility for Beams of Ions and Antiprotons. http://www.fair-center.eu/fair-users/publications/fair-publications.html.

[20] Taylor J. T. *Proton Induced Quasi-free Scattering with Inverse Kinematics*. Ph.D. thesis, University of Liverpool, United Kingdom (2011).

[21] EXL collaboration. Technical proposal for the design, construction, commissioning and operation of the EXL project. http://www-linux.gsi.de/~wwwnusta/tech_report/05-exl.pdf (2006).

[22] R^3B collaboration. R^3B , a universal setup for kinematical complete measurements of Reactions with Relativistic Radioactive Beams. http://www-win.gsi.de/r3b/Documents/R3B-TP-Dec05.pdf (2005).

[23] Tanihata I., Hamagaki H., Hashimoto O. *et al.* Measurements of interaction cross sections and nuclear radii in the light *p*-shell region. *Physical Review Letters* **55**, 2676 – 2679 (1985). URL http://link.aps.org/doi/10.1103/PhysRevLett.55.2676.

[24] Fukunishi N., Otsuka T. & Tanihata I. Neutron-skin and proton-skin formations in exotic nuclei far from stability. *Physical Review C* **48**, 1648 – 1655 (1993). URL http://link.aps.org/doi/10.1103/PhysRevC.48.1648.

[25] Yoshida S. & Sagawa H. Neutron skin thickness and equation of state in asymmetric nuclear matter. *Physical Review C* **69**, 024318 (2004). URL http://link.aps.org/doi/10.1103/PhysRevC.69.024318.

[26] Horowitz C. J. & Piekarewicz J. Neutron star structure and the neutron radius of ^{208}Pb. *Physical Review Letters* **86**, 5647 – 5650 (2001). URL http://link.aps.org/doi/10.1103/PhysRevLett.86.5647.

[27] Lattimer J. M. & Prakash M. Neutron star structure and the equation of state. *The Astrophysical Journal* **550**, 426 (2001). URL http://stacks.iop.org/0004-637X/550/i=1/a=426.

[28] Fernandez-Dominguez B., Thomas J. S., Catford W. N. *et al.* Emergence of the $N = 16$ shell gap in ^{21}O. *Physical Review C* **84**, 011301 (2011). URL http://link.aps.org/doi/10.1103/PhysRevC.84.011301.

[29] Otsuka T., Fujimoto R., Utsuno Y. *et al.* Magic numbers in exotic nuclei and spin-isospin properties of the *NN* interaction. *Physical Review Letters* **87**, 082502 (2001). URL http://link.aps.org/doi/10.1103/PhysRevLett.87.082502.

[30] Otsuka T., Suzuki T., Fujimoto R. *et al.* Evolution of nuclear shells due to the tensor force. *Physical Review Letters* **95**, 232502 (2005). URL http://link.aps.org/doi/10.1103/PhysRevLett.95.232502.

[31] Smirnova N., Bally B., Heyde K. *et al.* Shell evolution and nuclear forces. *Physics Letters B* **686**, 109 – 113 (2010). URL http://www.sciencedirect.com/science/article/pii/S0370269310002388.

[32] Wheeler J. A. Molecular viewpoints in nuclear structure. *Physical Reviews* **52**, 1083 – 1106 (1937). URL http://link.aps.org/doi/10.1103/PhysRev.52.1083.

[33] Freer M., Casarejos E., Achouri L. *et al.* α:2n:α molecular band in ^{10}Be. *Physical Review Letters* **96**, 042501 (2006). URL http://link.aps.org/doi/10.1103/PhysRevLett.96.042501.

[34] Hodgson P. & Betak E. Cluster emission, transfer and capture in nuclear reactions. *Physics Reports* **374**, 1 – 89 (2003). URL http://www.sciencedirect.com/science/article/pii/S0370157302002685.

[35] Davidson J. P. *Collective models of the nucleus* (Academic press Inc., 1968).

[36] Heyde K. *Basic Ideas and Concepts in Nuclear Physics an introductory approach* (Institute Of Physics (IOP) Publishing, 1999), 2nd edn.

[37] Harakeh M. N. & van der Woude A. *Giant resonances; Foundamental High-Frequency modes of Nuclear Excitations* (OXFORD science publications, 2001).

[38] Fattoyev F. J., Horowitz C. J., Piekarewicz J. & Shen G. Relativistic effective interaction for nuclei, giant resonances, and neutron stars. *Physical Review C* **82**, 055803 (2010). URL http://link.aps.org/doi/10.1103/PhysRevC.82.055803.

[39] Suzuki T., Sagawa H. & Bortignon P. Shell-model study of electric dipole and spin-dipole strengths in ^{11}Li. *Nuclear Physics A* **662**, 282 – 294 (2000). URL http://www.sciencedirect.com/science/article/pii/S0375947499003644.

[40] Adrich P., Klimkiewicz A., Fallot M. *et al.* Evidence for pygmy and giant dipole resonances in ^{130}Sn and ^{132}Sn. *Physical Review Letters* **95**, 132501 (2005). URL http://link.aps.org/doi/10.1103/PhysRevLett.95.132501.

[41] Goriely S. & Khan E. Large-scale qrpa calculation of e1-strength and its impact on the neutron capture cross section. *Nuclear Physics A* **706**, 217 – 232 (2002). URL http://www.sciencedirect.com/science/article/pii/S0375947402008606.

[42] Paar N., Ring P., Niksic T. & Vretenar D. Quasiparticle random phase approximation based on the relativistic hartree-bogoliubov model. *Physical Review C* **67**, 034312 (2003). URL http://link.aps.org/doi/10.1103/PhysRevC.67.034312.

[43] Baran V., Frecus B., Colonna M. & Di Toro M. Pygmy dipole resonance: Collective features and symmetry energy effects. *Physical Review C* **85**, 051601 (2012). URL http://link.aps.org/doi/10.1103/PhysRevC.85.051601.

[44] Toki H. & Castel B. Ikeda's sum rule and charge-exchange reactions on 54fe. *Physics Letters B* **219**, 181 – 183 (1989). URL http://www.sciencedirect.com/science/article/pii/0370269389903730.

[45] Osterfeld F. Nuclear spin and isospin excitations. *Reviews of Modern Physics* **64**, 491 – 557 (1992). URL http://link.aps.org/doi/10.1103/RevModPhys.64.491.

[46] Marketin T., Martinez-Pinedo G., Paar N. & Vretenar D. Role of momentum transfer in the quenching of gamow-teller strength. *Physical Review C* **85**, 054313 (2012). URL http://link.aps.org/doi/10.1103/PhysRevC.85.054313.

[47] Ichimura M., Sakai H. & Wakasa T. Spin-isospin responses via and reactions. *Progress in Particle and Nuclear Physics* **56**, 446 – 531 (2006). URL http://www.sciencedirect.com/science/article/pii/S0146641005001006.

[48] Kratz K.-L., Harms V., Weohr A. & Meoller P. Gamow-teller decay of ^{80}Zn: Shell structure and astrophysical implications. *Physical Review C* **38**, 278 – 284 (1988). URL http://link.aps.org/doi/10.1103/PhysRevC.38.278.

[49] Botvina A. & Mishustin I. Statistical approach for supernova matter. *Nuclear Physics A* **843**, 98 – 132 (2010). URL http://www.sciencedirect.com/science/article/pii/S0375947410005099.

[50] Borderie B. & Rivet M. Nuclear multifragmentation and phase transition for hot nuclei. *Progress in Particle and Nuclear Physics* **61**, 551 – 601 (2008). URL http://www.sciencedirect.com/science/article/pii/S0146641008000045.

[51] Itkis M. G., Oganessian Y. T. & Zagrebaev V. I. Fission barriers of superheavy nuclei. *Physical Review C* **65**, 044602 (2002). URL http://link.aps.org/doi/10.1103/PhysRevC.65.044602.

[52] Campi X. & Hüfner J. Nuclear spallation-fragmentation reactions induced by high-energy projectiles. *Physical Review C* **24**, 2199 – 2209 (1981). URL http://link.aps.org/doi/10.1103/PhysRevC.24.2199.

[53] Bauer G. Physics and technology of spallation neutron sources. *Nuclear Instruments and Methods in Physics Research Section A* **463**, 505 – 543 (2001). URL http://www.sciencedirect.com/science/article/pii/S016890020100167X.

[54] Mashnik S. G. On solar system and cosmic rays nucleosynthesis and spallation processes (2000). URL arXiv:astro-ph/0008382.

[55] Hansen P. G. & Tostevin J. A. Direct reactions with exotic nuclei. *Annual Review of Nuclear and Particle Science* **53**, 219–261 (2003). URL http://www.annualreviews.org/doi/abs/10.1146/annurev.nucl.53.041002.110406.

[56] Berggren T. & Tyren H. Quasi-free scattering. *Annual Review of Nuclear Science* **16**, 153–182 (1966). URL http://www.annualreviews.org/doi/abs/10.1146/annurev.ns.16.120166.001101.

[57] Sakurai J. J. *Modern quantum mechanics* (Addison-Wesley Publishing company, 1994), revised edn.

[58] Amakawa H. & Austern N. Adiabatic-approximation survey of breakup effects in deuteron-induced reactions. *Phys. Rev. C* **27**, 922 – 929 (1983). URL http://link.aps.org/doi/10.1103/PhysRevC.27.922.

[59] Lee J., Tsang M. B. & Lynch W. G. Neutron spectroscopic factors from transfer reactions. *Physical Review C* **75**, 064320 (2007). URL http://link.aps.org/doi/10.1103/PhysRevC.75.064320.

[60] Brown B. A., Hansen P. G., Sherrill B. M. & Tostevin J. A. Absolute spectroscopic factors from nuclear knockout reactions. *Phys. Rev. C* **65**, 061601 (2002). URL http://link.aps.org/doi/10.1103/PhysRevC.65.061601.

[61] Jensen O., Hagen G., Hjorth-Jensen M. *et al.* Quenching of spectroscopic factors for proton removal in oxygen isotopes. *Physical Review Letters* **107**, 032501 (2011). URL http://link.aps.org/doi/10.1103/PhysRevLett.107.032501.

[62] Dean D. J. & Hjorth-Jensen M. Coupled-cluster approach to nuclear physics. *Physical Review C* **69**, 054320 (2004). URL http://link.aps.org/doi/10.1103/PhysRevC.69.054320.

[63] Shavitt I. & Bartlett R. J. *Many-Body Methods in Chemistry and Physics* (Cambridge University Press, Cambridge, England, 2009).

[64] Tostevin J. Single-nucleon knockout reactions at fragmentation beam energies. *Nuclear Physics A* **682**, 320 – 331 (2001). URL http://www.sciencedirect.com/science/article/pii/S0375947400006564.

[65] Mukhamedzhanov A. & Nunes F. Can spectroscopic informations be extracted from transfer reactions? *Revista mexicana de fisica* **52**, 30 – 34 (2006). URL http://www.scielo.org.mx/scielo.php?script=sci_arttext&pid=S0035-001X2006000700007&nrm=iso.

[66] Palit R., Adrich P., Aumann T. *et al.* Exclusive measurement of breakup reactions with the one-neutron halo nucleus ^{11}Be. *Physical Review C* **68**, 034318 (2003). URL http://link.aps.org/doi/10.1103/PhysRevC.68.034318.

[67] Gade A., Bazin D., Brown B. A. *et al.* Reduced occupancy of the deeply bound $0d_{5/2}$ neutron state in ^{32}Ar. *Physical Review Letters* **93**, 042501 (2004). URL http://link.aps.org/doi/10.1103/PhysRevLett.93.042501.

[68] Gade A., Adrich P., Bazin D. *et al.* Reduction of spectroscopic strength: Weakly-bound and strongly-bound single-particle states studied using one-nucleon knockout reactions. *Physical Review C* **77** (2008). URL http://link.aps.org/doi/10.1103/PhysRevC.77.044306.

[69] Agostinelli S., Allison J., Amako K. *et al.* Geant4 a simulation toolkit. *Nuclear Instruments and Methods in Physics Research Section A* **506**, 250 – 303 (2003). URL http://www.sciencedirect.com/science/article/pii/S0168900203013688.

[70] Borger P. J. *In-beam test of the EXL demonstrator at KVI*. M.Sc. thesis, University of Groningen, The Netherlands (2010).

[71] Najafi M. A., Kalantar-Nayestanaki N. & Rigollet C. In-beam test of the EXL demonstrator at GSI. http://nustar-wiki.gsi.de/pub/EXL/ExlDemonstratorTest/EXLdemoTest_GSI_Sep09.pdf (2010).

[72] Twenhofel C. J. W., Box P. F., Schotanus P. *et al.* The response function of a CsI(Tl) scintillator with photodiode readout to light and heavy ions in the intermediate energy range. *Nuclear Instruments and Methods in Physics Research Section B* **51**, 58 – 62 (1990).

[73] Moeini H. *Feasibility Experiment and Simulations for EXL*. Ph.D. thesis, University of Groningen, The Netherlands (2010).

[74] Geissel H., Armbruster P., Behr K. *et al.* The GSI projectile fragment separator (FRS); a versatile magnetic system for relativistic heavy ions. *Nuclear Instruments and Methods in Physics Research Section B* **70**, 286 – 297 (1992). URL http://www.sciencedirect.com/science/article/pii/0168583X9295944M.

[75] Weick H. FRS website. http://www-wnt.gsi.de/frs/index.asp.

[76] Johansson H. T. *The DAQ always runs, Performing large scale nuclear physics experiments*. Ph.D. thesis, Chalmers University of Technology, Goteborg, Sweden (2006).

[77] Azzarello P. *Tests And Production Of The AMS-02 Silicon Tracker Detectors*. Ph.D. thesis, University of Geneva, Switzerland (2004).

[78] Alcaraz J., Alpat B., Ambrosi G. *et al.* The alpha magnetic spectrometer silicon tracker: Performance results with protons and helium nuclei. *Nuclear Instruments and Methods in Physics Research Section A* **593**, 376 – 398 (2008). URL http://www.sciencedirect.com/science/article/pii/S0168900208007122.

[79] Wamers F. *Quasi-Free-Scattering and One-Proton-Removal Reactions with the Proton-Dripline Nucleus ^{17}Ne at Relativistic Beam Energies*. Ph.D. thesis, Technical University of Darmstadt, Germany (2011).

[80] Langer C. *Coulomb Dissociation of ^{31}Cl and ^{32}Ar - Constraining the rp process*. Ph.D. thesis, Johann-Wolfgang-Goethe University of Frankfurt, Germany (2012).

[81] Metag V. *et al.* The darmstadt-heidelberg crystal-ball. In *Proc. Geiger Memorial Meeting* (1982).

[82] Thies R. *Prototype tests and pilot experiments for the R^{3}B scintillator-based detection systems*. M.Sc. thesis, Chalmers university of technology, Goteborg, Sweden (2011).

[83] Panin V. *Fully Exclusive Measurements of Quasi-Free Single-Nucleon Knockout Reactions in Inverse Kinematics*. Ph.D. thesis, Technical university of Darmstadt, Germany (2012).

[84] Blaich T., Elze T., Emling H. *et al.* A large area detector for high energy neutrons. *Nuclear Instruments and Methods in Physics Research Section A* **314**, 136 – 154 (1992).

[85] Rossi D. M. *Investigation of the Dipole Response of Nickel Isotopes in the Presence of a High-Frequency Electromagnetic Field*. Ph.D. thesis, University of Mainz (2009).

[86] Cub J., Stengel G., Grunschloss A. *et al.* A large-area scintillating fiber detector for relativistic heavy ions. *Nuclear Instruments and Methods in Physics Research Section A* **402(1)**, 67 – 74 (1998).

[87] Mahata K., Johansson H., S.Paschalis *et al.* Position reconstruction in large-area scintillating fibre detectors. *Nuclear Instruments and Methods in Physics Research Section A* **608**, 331 – 335 (2009). URL http://www.sciencedirect.com/science/article/pii/S0168900209014296.

[88] Paschalis S. *Relativistic One-Nucleon Removal Reactions*. Ph.D. thesis, University of Liverpool, United Kingdom (2008).

[89] Veenhof R. GARFIELD, recent developments. *Nuclear Instruments and Methods in Physics Research Section A* **419**, 726 – 730 (1998). URL http://www.sciencedirect.com/science/article/pii/S0168900298008511.

[90] Ershova O. *Coulomb Dissociation Reactions on Molybdenum Isotopes for Astrophysics Applications*. Ph.D. thesis, Johann-Wolfgang-Goethe University of Frankfurt, Germany (2011).

[91] DiJulio D., Avdeichikov V., Cederkall J. *et al.* Proton in-beam tests of the Lund calorimeter prototype. *Nuclear Instruments and Methods in Physics Research Section A* **612**, 127 – 132 (2009). URL http://www.sciencedirect.com/science/article/pii/S0168900209019160.

[92] Gascon M., Alvarez-Pol H., Benlliure J. *et al.* Test of LAAPDs Coupled to CsI(Tl) Crystals for the CALIFA R3B/FAIR Calorimeter. *Nuclear Science, IEEE Transactions on Nuclear Science* **57**, 1465 –1469 (2010). URL http://ieeexplore.ieee.org/xpls/abs_all.jsp?arnumber=5485132&tag=1.

[93] Akkoyun S. *et al.* AGATA - Advanced GAmma Tracking Array. *Nuclear Instruments and Methods in Physics Research Section A* **668**, 26 – 58 (2012). URL http://www.sciencedirect.com/science/article/pii/S0168900211021516.

[94] Bertini D. R3broot, simulation and analysis framework for the r3b experiment at fair. *Journal of Physics: Conference Series* **331**, 032036 (2011). URL http://stacks.iop.org/1742-6596/331/i=3/a=032036.

[95] Al-Turany M., Bertini D., Karabowicz R. *et al.* The FairRoot framework. *Journal of Physics: Conference Series* **396**, 022001 (2012). URL http://stacks.iop.org/1742-6596/396/i=2/a=022001. FairRoot website: http://fairroot.gsi.de/.

[96] Sohler D., Stanoiu M., Dombrádi Z. *et al.* In-beam γ-ray spectroscopy of the neutron-rich nitrogen isotopes $^{19-22}$N. *Physical Review C* **77**, 044303 (2008). URL http://link.aps.org/doi/10.1103/PhysRevC.77.044303.

[97] Elekes Z., Vajta Z., Dombrádi Z. *et al.* Nuclear structure study of ^{19,21}N nuclei by γ spectroscopy. *Physical Review C* **82**, 027305 (2010). URL http://link.aps.org/doi/10.1103/PhysRevC.82.027305.

[98] Wiedeking M., Fallon P., Macchiavelli A. O. *et al.* Nuclear structure of ^{18}N and the neighboring $N = 11$ isotones. *Physical Review C* **77**, 054305 (2008). URL http://link.aps.org/doi/10.1103/PhysRevC.77.054305.